

**Scanned Probe Microscopy of the Electronic Properties
of Low-Dimensional Systems**

by

Michael Thomas Woodside

B.Sc. (University of Toronto) 1995

A dissertation submitted in partial satisfaction of
the requirements for the degree of

Doctor of Philosophy

in

Physics

in the

GRADUATE DIVISION

of the

UNIVERSITY of CALIFORNIA, BERKELEY

Committee in charge:

Professor Paul L. McEuen, Chair

Professor Dung-Hai Lee

Professor Arunava Majumdar

Fall 2001

**Scanned Probe Microscopy of the Electronic Properties
of Low-Dimensional Systems**

Copyright © 2001

by

Michael Thomas Woodside

Abstract

**Scanned Probe Microscopy of the Electronic Properties
of Low-Dimensional Systems**

by

Michael Thomas Woodside

Doctor of Philosophy in Physics

University of California, Berkeley

Professor Paul L. McEuen, chair

The local electronic properties of low-dimensional systems are explored using a low-temperature atomic force microscope (AFM) sensitive to electrostatic forces. Two low-dimensional systems are measured: a two-dimensional electron gas in the quantum Hall regime, and a one-dimensional electron gas in single-walled carbon nanotubes.

The properties of the edge of a quantum Hall conductor are investigated by studying non-equilibrium edge state populations. Electrostatic force microscopy (EFM) is used to measure the local Hall voltage distribution at the edge of a quantum Hall conductor in the presence of a gate-induced non-equilibrium edge state population. Disequilibrium edge state potentials are clearly observed, with a sharp voltage drop seen near the edge of the sample. Equilibration of the edge state potentials by inter edge state scattering is also imaged locally with EFM. Scanned gate microscopy (SGM) is used to probe the inter edge state scattering further, by investigating the scattering mechanisms involved. Scattering is found to be dominated by individual scattering centers, which are imaged with

SGM. Evidence is found for scattering from both weak links between the edge states and microscopic impurities.

The local electronic properties of carbon nanotubes are explored by studying single-electron charging effects in quantum dots that form within the nanotubes. SGM is used to locate individual quantum dots in a nanotube and observe Coulomb oscillations in their conductance. The dependence of the scanned gate images on the AFM tip voltage is found to be influenced strongly by the electrostatic environment of the nanotube, and a phenomenological model is introduced to describe these effects. EFM measurements are used to detect Coulomb oscillations in the electrostatic force exerted by the nanotube on the AFM tip. These Coulomb oscillations in the force are due to the change in the electrostatic potential of the quantum dot associated with single electron charging. Coulomb oscillations in the resonant frequency of the AFM cantilever are also observed, due to the spatial gradient of the force exerted by the dot. In both cases, quantitative agreement with theory is obtained. Finally, degradation of the Q -factor of the cantilever resonance is observed at the same locations as the Coulomb oscillations in the conductance, the force, and the resonance frequency. An explanation in terms of dissipation of the cantilever energy through coupling to single electron motion in the quantum dot is proposed.

To my grandparents, for their unfailing kindness and wisdom
To my parents, for their unstinting love and support

Citius emergit veritas ex errore quam ex confusione
Truth emerges more readily from error than confusion

—Sir Francis Bacon, *Novum Organum* (1620)

As steals the morn upon the night,
And melts the shades away,
So truth does fancy's charm dissolve,
And rising reason puts to flight
The fumes that did the mind involve,
Restoring intellectual day.

—Charles Jennens/Georg Frideric Handel,
L'Allegro, il Penseroso ed il Moderato (1740)

Table of Contents

Acknowledgements **vi**

CHAPTER 1: *Introduction: Electron Transport in Low Dimensions* 1

1.1 Introduction 1

1.2 Electron Transport and Low Dimensions 3

1.2 Conductance Quantisation in a One-Dimensional Channel 5

1.3 Quantum Dots and Single-Electron Transport 9

1.4 Scanned Probe Measurements 14

1.5 Outline 16

CHAPTER 2: *The Low-Temperature Atomic Force Microscope* 17

2.1 Introduction 17

2.2 AFM Cantilever Dynamics 19

2.3 Electrostatic Force on the AFM Tip 23

2.4 Contact Potential and Fixed Charges 26

2.5 AFM Design and Performance 28

2.6 Measurement Techniques: Electrostatic Force Microscopy 33

2.7 Measurement Techniques: Scanned Gate Microscopy 38

2.8 Summary 41

CHAPTER 3: *Non-Equilibrium Edge State Populations in Quantum Hall Conductors* 43

 3.1 Introduction 43

 3.2 Integer Quantum Hall Effect 44

 3.3 Edge of the Quantum Hall Conductor 48

 3.4 2DEG Sample 52

 3.5 Creating Non-Equilibrium Edge State Populations 54

 3.6 EFM of Non-Equilibrium Edge States in a Quantum Hall Conductor 56

 3.7 Summary 61

CHAPTER 4: *Individual Scattering Centers in the Quantum Hall Regime* . . 63

 4.1 Introduction 63

 4.2 Scanned Gate Microscopy of Inter Edge State Scattering 65

 4.3 Interpretation 71

 4.4 Summary 76

CHAPTER 5: *Electron Transport in Nanotubes* 77

 5.1 Introduction 77

 5.2 Band Structure of Carbon Nanotubes 78

 5.3 Transport Measurements of Nanotubes 81

 5.4 Scanned Probe Measurements of Nanotubes 85

CHAPTER 6: *Single-Electron Scanned Gate Microscopy of Carbon Nanotubes* 88

6.1 Introduction 88

6.2 Device Fabrication and Properties 89

6.3 Scanned Gate Images in the Single-Electron Regime 91

6.4 Characterising A Quantum Dot and the Tip-Dot Interaction 95

6.5 Tip Voltage Dependence of Scanned Gate Images 101

6.6 Qualitative Interpretation of Scanned Gate Images 103

6.7 Phenomenological Model of Scanned Gate Measurement 108

6.8 Quantitative Interpretation of Scanned Gate Images 112

6.8 Summary 116

CHAPTER 7: *Single-Electron Force Microscopy in Carbon Nanotubes* . . . 117

7.1 Introduction 117

7.2 Electrostatic Force Measurements 118

7.3 Interpretation of EFM Measurements 122

7.4 Investigating Other Nanotubes 129

7.5 Frequency Shift Measurements 134

7.6 Interpretation of Frequency Shift Measurements 138

7.7 Q Degradation Measurements 141

7.8 Interpretation of Q Degradation Measurements 148

| | |
|---|------------|
| 7.9 Summary | 154 |
| CHAPTER 8: <i>Conclusion</i> | 156 |
| 8.1 Summary | 156 |
| 8.2 Future Directions | 158 |
| 8.3 Concluding Remarks | 160 |
| <i>Appendix</i> | 161 |
| A.1 Scanned Gate Movie: Fig. 6.8 | 161 |
| A.2 Scanned Gate Movie: Fig. 6.10 | 162 |
| <i>References</i> | 165 |

Acknowledgements

Science is a collective and social endeavour, and it is a pleasure to acknowledge here the efforts of the many people who have contributed to the work presented in this dissertation. Foremost among these is of course my advisor, Paul McEuen, who has helped guide this research to a satisfying conclusion. Paul's advice has been invaluable at many stations along the way, and his clarity and focus continue to be an inspiration. It has been both a pleasure and a privilege to work with him on this project.

I am also deeply indebted to my predecessor on this project, Kent McCormick, who originally designed and built the atomic force microscope I used in this research. Without Kent's work, none of this would have been possible. Kent is one of those rare individuals who combine a rigorously analytical outlook with a ruthlessly pragmatic empiricism, and it was a delight to join him on this research.

Several people helped with the task of obtaining the samples I measured. The semiconductor heterostructures used in this work were kindly provided by Christoph Kadow and Kevin Maranowski from Art Gossard's group at UC Santa Barbara. These wafers were shaped into working samples by Chris Vale. Chris also helped fabricate the carbon nanotube devices, along with Jiwoong Park, Philip Kim, and Michael Fuhrer. I thank all these people for helping make it possible to get this research under way.

I would also like to thank my co-workers in the lab, both graduate students and postdocs, with whom it has been a pleasure to work. Chris, who worked with me on this research before leaving for greener pastures elsewhere, was always full of witty quips and

disarmingly insightful questions. Marc was a constant whirlwind of activity and ideas, and an inspiration in how to get things done post-haste. Noah's uncompromising attention to detail was equally impressive, both in the lab and outside, and I thank him for many helpful suggestions in rebuilding the AFM. Thanks also go to Jiwoong, who continues to amaze me with his steady competence, for his help with the work on nanotubes. Finally, I thank Cobbie, Hongkun, Tex, and Philip, for their willingness to provide advice and help when I needed it.

Financial support for this work was provided by the National Science Foundation, the AT&T Foundation, and the Packard Foundation. Special thanks go to the Natural Sciences and Engineering Research Council of Canada for several years of fellowship support.

Outside of the lab, I would like to thank the denizens of Creston Rd., Andrew, Bina, Helene, and Manya, for many years of cooking, talking, singing, and simply living together in such a civilised setting. Heartfelt thanks also go to my choir, *Vox Populi*, for providing a nurturing environment for a fledgling singer. Some of my fondest memories of Berkeley include the ethereal sounds of reverberating counterpoint and the Lucullan feasts at Voxpopluck rehearsals. Singing with Voxpop has left a truly indelible impression on my soul.

Finally, I would like to thank my family, and especially my parents, for their love, understanding, and support, during times both good and bad, in the many years that I have been gone abroad.

CHAPTER 1: *Introduction: Electron Transport in
Low Dimensions*

1.1 Introduction

When electrons in a conductor are physically confined so that they can no longer move in fully three-dimensional space, but only in two-dimensional, one-dimensional, or even point-like zero-dimensional regions of space, a *low-dimensional system* is created. The electronic properties of low-dimensional systems have been the subject of much interest in the last two decades, driven by the twin goals of discovering new physics and developing potential applications. Studies of low-dimensional systems have indeed yielded exciting new discoveries, such as the Quantum Hall Effects, for which two Nobel Prizes have been awarded. They have also permitted beautiful demonstrations of more established physics in elegant model systems, such as energy level structure (Kouwenhoven 1997) and the Kondo Effect (Goldhaber-Gordon 1998) in artificial atoms. The electronic properties of low-dimensional systems remain an important topic of research, with ongoing explorations of novel physical, chemical and biological systems.

To date, much of the work on these systems has involved measurements of electron transport. Transport measurements are a powerful tool that have provided many crucial insights into the properties of low-dimensional electrons. They are not ideal for studying the local properties of these systems, however, since they are typically not capa-

ble of good spatial discrimination. In order to study the local electronic properties of low-dimensional systems in more detail, we turn to novel scanned probe technologies that have been developed in the years since the invention of the scanning tunnelling microscope (Binnig 1981) and the atomic force microscope (Binnig 1986). Scanned probe microscopes use a very small sensor probe that can be scanned with high spatial resolution over the sample. They therefore provide an excellent tool for probing the local properties of a system.

In this dissertation, we report investigations of the electronic properties of low-dimensional systems using scanned probe techniques. We employ an atomic force microscope that is sensitive to electrostatic forces to study the properties of two particular systems: in two dimensions (2D), an electron gas in the quantum Hall regime; and in one dimension (1D), carbon nanotubes. These scanned probe investigations are complementary to the results of electron transport studies. We therefore begin with a review of electron transport in low dimensions. In section 1.2, we give a brief survey of the variety of transport phenomena observed in low dimensional systems. This is followed by a more detailed look at two phenomena that will prove important in later measurements: conductance quantisation in 1D (section 1.3) and single electron transport in quantum dots (section 1.4). In section 1.5, we present a brief outline of some of the scanned probe techniques that have been used to study the electronic properties of low-dimensional systems, before concluding with an outline of the rest of the dissertation.

1.2 Electron Transport and Low Dimensions

The study of electrical conduction, the motion of electric charge inside matter, has a long and distinguished history in the annals of physics. Indeed, physicists' understanding of electricity has led to technology that has fundamentally altered the basis of modern society, from labour-saving devices (robots, elevators, washing machines, ...) to environmental control (lighting, refrigeration, air conditioning, ...) to communications and the information revolution (telephones, radio, television, computers,...). It is now over 100 years since the first successful comprehensive theory of conductivity was proposed by Paul Drude (Drude 1900a, 1990b). Remarkably, electron transport still remains a central area of active research in condensed matter physics, in fields as diverse as superconductivity, magnetic structures, and mesoscopic systems. To a large extent, this continuing relevance is due to the fact that the electrical behaviour of materials is extremely sensitive to their microscopic properties: the conductivity of different materials, for instance, can vary by over 20 orders of magnitude. Electron transport thus provides a very sensitive tool for probing the properties of many physical systems.

Advances in materials science and semiconductor fabrication technology over the last 3 decades have now made it possible to construct conductors with dimensions on the order of microns to nanometers. These conductors are called *mesoscopic* because they are intermediate in size between everyday macroscopic systems and the microscopic atomic scale. Interesting physics arises in mesoscopic systems because the size of the system has been reduced to the same order of magnitude as the typical length scales for scattering and

| | |
|--|---|
| <p>2D</p>  | <p>Quantum wells 2D electron gases Layered structures</p> |
| <p><u>Non-interacting physics:</u></p> <p>2D sub-bands Integer Quantum Hall Effect</p> | <p><u>Interactions and disorder:</u></p> <p>Fractional Quantum Hall Effect Composite fermions, anyons, skyrmions Metal-insulator transition ?</p> |
| <p>1D</p>  | <p>Carbon nanotubes Quantum point contacts nanowires, polymers</p> |
| <p>1D sub-bands Quantised conductance</p> | <p>Luttinger liquid Charge density waves</p> |
| <p>0D</p>  | <p>Quantum dots Nanocrystals</p> |
| <p>Quantised energy levels "Atomic" spectra</p> | <p>Single-electron charging Kondo effect</p> |

Fig. 1.1: Examples of low-dimensional systems and physical phenomena observed in them. The work presented here will investigate 2D electron gases in the integer quantum Hall regime and 1D carbon nanotubes.

quantum mechanical coherence. In addition, it is possible to physically restrict the motion of the electrons in one or more dimension, effectively reducing the dimensionality of the electrons. Since the balance between kinetic and potential energies depends sensitively on the dimensionality, this also has profound consequences for the electronic behaviour. The study of electron transport in low-dimensional mesoscopic systems has led to the discovery of a rich set of qualitatively new physical phenomena.

Some of these phenomena are listed in Fig. 1.1. For example, electrons confined to a two-dimensional (2D) plane, known as a 2D electron gas (2DEG), give rise to the integer and fractional Quantum Hall Effects and related phenomena such as composite fermions, fractionally charged quasiparticles, and skyrmions (for a review see Das Sarma

1997, Prange 1990). There are also interesting questions concerning metal-insulator transitions in 2D systems (Kravchenko 1996). Examples of 2D systems include Si MOSFETs and GaAs/AlGaAs heterostructures. Electrons confined to form a one-dimensional (1D) wire give rise to conductance quantisation and Luttinger liquid behaviour (for a review see Sohn 1997). Such 1D systems include quantum point contacts, semiconductor quantum wires, nanowires, and carbon nanotubes. Finally, when electrons are confined in all directions and form a zero-dimensional (0D) “dot”, Coulomb oscillations and single-electron transport through individual quantum levels are seen (for a review, see Grabert 1992). Examples of 0D systems include nanocrystals and semiconductor quantum dots.

Electron transport in low-dimensional mesoscopic systems thus covers a very broad range of behaviours and systems. The work presented herein will be concentrate on only two specific systems: for 2D electrons, the integer quantum Hall Effect; and for 1D electrons, carbon nanotubes. As we shall see later, electron transport in the integer quantum Hall regime involves 1D conducting channels embedded in a 2D plane of electrons, while transport in nanotubes involves 0D quantum dots embedded in a 1D wire. These two systems thus encapsulate many of the interesting features of low-dimensional systems.

1.2 Conductance Quantisation in a One-Dimensional Channel

The conductance G of a sample is the relationship between the current I that flows across the sample in response to an electrochemical potential difference $\Delta\mu$ across it:

$$I = G \cdot \Delta\mu$$

In the Drude model of conduction, the conductance G , an extrinsic property of the sample, is calculated in terms of the local conductivity σ , an intrinsic property which expresses the local current density \vec{j} in terms of the net electric field \vec{E} in the conductor: $\vec{j} = \sigma \cdot \vec{E}$.

The conductivity σ is found to depend on the density n and mass m of the electrons, and on the average time τ between electron scattering events in the conductor:

$$\sigma = \frac{ne^2\tau}{m}$$

The conductance of the sample is calculated by integrating the local conductivity. In the case of a sample of width w , height h , and length l with uniform conductivity σ , we obtain the well-known result (Kittel 1986):

$$G = \sigma \left(\frac{wh}{l} \right) \tag{1.1}$$

The Drude model works very well for a wide variety of applications within the macroscopic domain. It breaks down in mesoscopic systems, however, because it treats scattering in an average way. The Drude model assumes that the scattering time τ is sufficiently short that scattering events will completely randomise the momentum and phase of the electrons as they pass through the conductor. In mesoscopic systems, however, the sample is of the same size-scale as the mean free path and the phase coherence length, so that this is no longer a good approximation. Instead, conductance in mesoscopic systems is approached in terms of a transmission problem through the conductor. This approach to the conductance is known as the Landauer-Büttiker theory (Landauer 1957, Büttiker 1986; for a review, see Datta 1995).

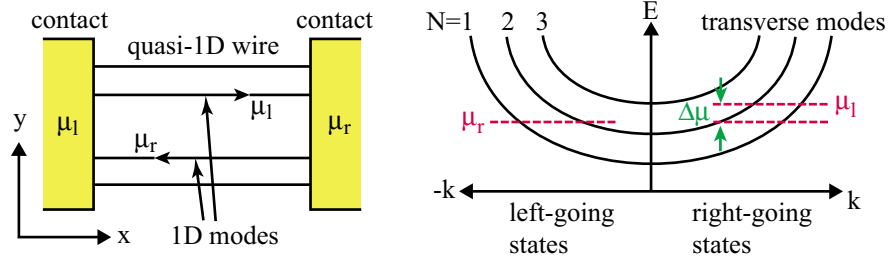


Fig. 1.2: Conduction in a quasi-1D wire. Electrons travel freely in x , with wavevector k , but their motion is quantised in y , producing 1D subbands $N=1,2,3,\dots$. Electrons coming from the right contact (left-moving electrons) have an electrochemical potential μ_r , those coming from the left contact (right-moving electrons) have a potential μ_l . An electrochemical potential difference $\Delta\mu=\mu_l-\mu_r$ gives rise to a net current in the wire. Here two (spinless) subbands are occupied, so the conductance in the absence of scattering is $G = 2e^2/h$.

Consider the conductance of a narrow wire in the absence of scattering. Electrons are free to move along the axis of the wire, but their transverse motion is quantised by the lateral confinement, creating a number of 1D subbands as shown in Fig. 1.2. We label the electronic states in each subband by their momentum k along the wire. The contacts at either end of the wire act as thermodynamic reservoirs that establish the electrochemical potential of the electrons originating from them. If there is an potential difference between the contacts, $\Delta\mu$, then the states travelling in opposite directions are populated to different levels and a net current flows between the contacts.

In each mode, the number of electrons carrying the net current is $\left(\frac{dn}{dE}\right)e\Delta\mu$, where $\frac{dn}{dE}$ is the electronic density of states per unit length of the channel, and the electrons move at the Fermi velocity v_F . The current in each mode (neglecting spin) is therefore given by:

$$I = \left(\frac{dn}{dE} \Big|_{E_F} \cdot e\Delta\mu \right) e v_F$$

In 1D, $\frac{dn}{dE} = \frac{2\pi}{h^2} \left(\frac{m}{k}\right)$ while $v_F = \frac{h}{2\pi} \left(\frac{k_F}{m}\right)$, so that the current in each mode is simply:

$$I = \left(\frac{e^2}{h}\right) \cdot \Delta\mu$$

If there are N 1D modes occupied in the conductor, the sum of the currents yields a total conductance of $G = N \left(\frac{e^2}{h}\right)$.

This describes the conductance when the conduction is ballistic, *i.e.* there is no scattering in the sample. Scattering is included by assuming that each 1D mode i in the conductor has a probability T_i of being transmitted. The current transmitted in each mode is reduced by the factor T_i , resulting in a total conductance of:

$$G = \left(\frac{e^2}{h}\right) \sum_i T_i \tag{1.2}$$

Eq. 1.2 expresses the conductance in a quasi-1D channel in terms of the transmission probabilities of 1D channels. We can see from this equation that when all the transmission probabilities are unity and the conduction is ballistic, the conductance is quantised in terms of the conductance quantum e^2/h . The quantisation of conductance in a quasi-1D channel is an important prediction of the Landauer-Büttiker model that differs markedly from the Drude model. This result has been verified experimentally by measurements of the conductance of a short electrostatically-defined constriction (van Wees 1988, Wharam 1988). As the width of the constriction is increased, its conductance increases not linearly as predicted by the Drude model (Eq. 1.1), but in steps of e^2/h , as predicted by Eq. 1.2.

1.3 Quantum Dots and Single-Electron Transport

If we take a one- or two-dimensional sample and restrict the motion of the electrons further, so that they are effectively confined to a zero-dimensional box, we create what is known as a quantum dot. Quantum dots have been studied extensively in semiconductor heterostructures, particularly dots that are created by electrostatic confinement in 2D electron systems. The rich behaviour of quantum dots is described in detail in reviews of the subject (Grabert 1992, Kastner 1993, Sohn 1997). Here we briefly present the essential properties of quantum dots that will be needed to understand the results discussed later.

For large samples, the fact that electronic charge is quantised is essentially irrelevant, and charge can be treated for most purposes as a continuous variable. As the size of the system being studied becomes smaller, however, the effects of charge quantisation gain in importance, until at the level of 0D quantum dots they can dominate the conductance. This can be seen by considering the effect of adding a single electron to a small conducting island (often called a *quantum dot*) that is coupled through tunnel barriers to source-drain leads¹. Due to the Coulomb repulsion between this electron and the electrons already present on the quantum dot, the electrostatic potential of the dot increases by an amount e/C upon addition of the electron, where C is the capacitance of the dot. The energy $U = e^2/C$ is called the *charging energy*, and it sets the energy scale at which the effects of charge quantisation become important. For $k_B T \ll U$, the thermal energy is

1. Tunnel barriers (rather than Ohmic contacts) are required to see single electron charging, to ensure that the electrons on the island are sufficiently well localised, *i.e.* that the electron occupancy of the island is well defined.

insufficient to allow even a single additional electron onto the quantum dot. The charge on the dot is thus fixed and no current can flow through the dot unless some other means is found to provide the charging energy. This phenomenon is known as *Coulomb blockade*: transport is blocked by the Coulomb repulsion from the electrons already on the dot.

The charge occupancy of a quantum dot can be changed by using a gate to alter the electrostatic potential of the dot and overcome the charging energy. A voltage V_g applied to a gate with capacitance C_g will change the electrostatic potential of the dot continuously as V_g is changed. Expressing this potential in terms of charge, the gate voltage induces an effective continuous charge $q = C_g V_g$. The actual charge on the dot can of course only change by integer multiples of e ; this continuous charge effectively represents the charge that the quantum dot would like to have if charge were not quantised. As we sweep V_g up, the charge on the dot remains quantised while the gate changes the electrostatic potential of the dot and induces a continuous charge q , until the gate voltage has provided enough energy to overcome the charging energy. At this point, an electron can tunnel onto the dot, changing the actual charge on the dot by e , and conductance through the dot is no longer blocked. The competition between the continuous charge q induced by the gate and the quantised charge that can actually transfer onto the dot thus results in periodic peaks in the conductance as a function of V_g , known as *Coulomb oscillations*.

The basic physical picture of Coulomb oscillations is illustrated schematically in Fig. 1.3. Here, we include the fact that the quantum dot, being a very small object, has its own discrete quantum level spacing, ΔE . The dot is connected to two contacts via tunnel

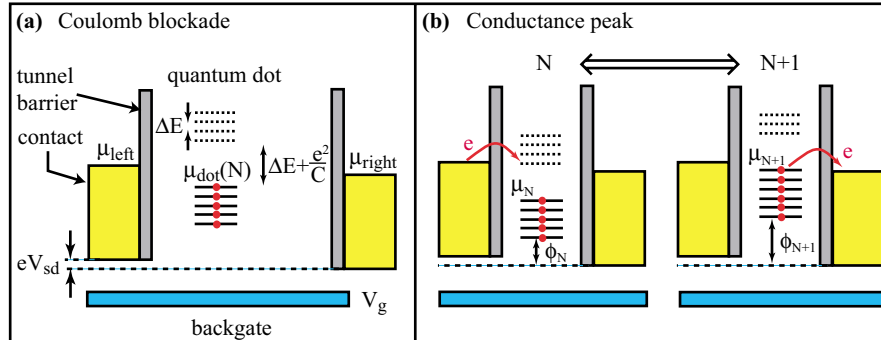


Fig. 1.3: Coulomb oscillations in the conductance of a quantum dot. **(a)** When the electrochemical potential of both leads lies in the energy gap $U+\Delta E$, no electrons can tunnel onto the dot. The occupancy of the dot is fixed and the conductance vanishes due to Coulomb blockade. **(b)** When the gate voltage is tuned so that the electrochemical potential of the dot lies between those of the leads, electrons can tunnel onto and then off of the dot, changing the occupancy of the dot and causing a peak in the conductance.

barriers. A source-drain bias V_{sd} much smaller than the charging energy and level spacing (*i.e.* in the linear regime) is applied across the dot. There is an energy gap $U+\Delta E$ between the highest occupied state and the lowest empty state on the dot; all other states on the dot are separated in energy by only the level spacing ΔE . When the electrochemical potential μ of both leads lies within the energy gap, as shown in Fig. 1.3(a), no electrons can tunnel on or off the dot, the conductance is zero, and the dot is in Coulomb blockade. When the gate voltage has tuned the electrostatic potential of the dot so that the energy of the lowest unoccupied state lies between μ_{left} and μ_{right} , as in Fig. 1.3(b), then an electron can tunnel onto the dot, changing the dot occupancy from N to $N+1$. The electrostatic potential of the dot then jumps up immediately, and the electron in the highest occupied state is able to tunnel off of the dot. The dot occupancy alternates between N and $N+1$ due to successive single-electron tunnelling events, leading to a peak in the conductance.

The simple model described above leads to an expression for the electrostatic potential $\phi(N)$ of a dot with occupancy N :

$$\phi(N) = (N - N_0) \frac{e}{C} - \frac{C_g V_g}{C} \quad (1.3)$$

Here, C is the total capacitance of the dot to its environment (*i.e.* to all gates as well as the leads), and N_0 is the dot occupancy at 0 gate voltage. Similarly, the electrochemical potential $\mu_{dot}(N)$ of a dot with occupancy N is given by:

$$\mu_{dot}(N) = E_N + (N - N_0) \frac{e^2}{C} - e \frac{C_g V_g}{C} \quad (1.4)$$

where E_N is the energy of the single particle state for the N th electron. From this expression we find the addition energy required to add a single electron to the dot:

$$\mu_{dot}(N+1) - \mu_{dot}(N) = \Delta E + \frac{e^2}{C} \quad (1.5)$$

as well as the spacing in gate voltage ΔV_g between conductance peaks:

$$\Delta V_g = \frac{C}{e C_g} \left(\Delta E + \frac{e^2}{C} \right) \quad (1.6)$$

Note that the peak spacing is not strictly periodic, as the level spacing ΔE may change from one state to the next and even the charging energy U is not strictly constant (it is a parametrisation of the Coulomb interactions among the electrons in a given state).

The variation with gate voltage of the conductance, the charge on the dot, the electrostatic potential of the dot, and the electrochemical energy of the dot are all plotted in Fig. 1.4. As the gate voltage moves through a conductance peak, the charge on the dot increases by one, the electrostatic potential increases by e^2/C , and the electrochemical

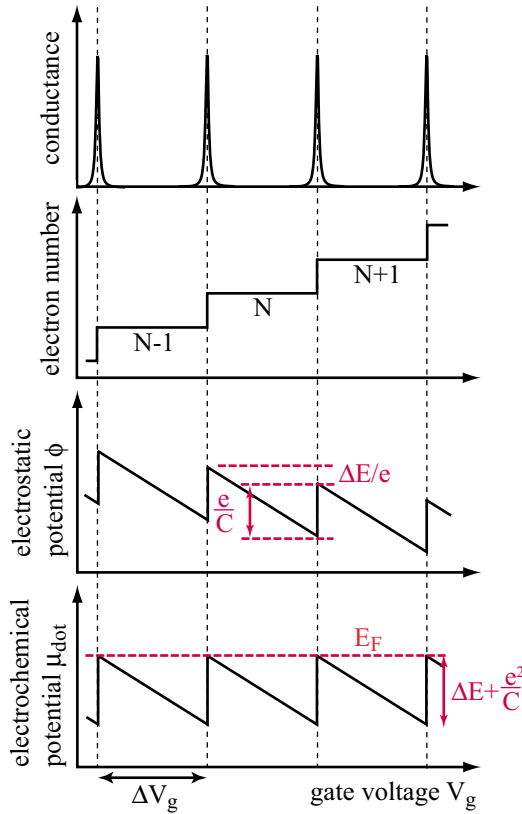


Fig. 1.4: Dependence of the conductance, electron occupancy, electrostatic potential, and electrochemical potential of a quantum dot on the gate voltage. The conductance **(a)** shows sharp peaks when the number of electrons on the dot **(b)** changes by 1. At the same time, the electrostatic potential of the dot **(c)** jumps by e/C and the electro-chemical potential **(d)** jumps by $\Delta E + e^2/C$.

potential increases by $\Delta E + e^2/C$. All of these changes have been shown as abrupt, as expected at $T = 0$ K. At finite temperatures, they are all broadened by the Fermi distribution function.

If the source-drain bias is increased into the non-linear regime, with $eV_{sd} \geq \Delta E$, then electrons can tunnel onto either the lowest or second-lowest unoccupied states. As V_{sd} is increased, ever more excited states are involved in the transport. The excitation energies of the quantum dot can therefore be explored by non-linear single-electron tunnelling. The transport measurements are thus in effect a spectroscopy of the energy levels

of the quantum dot, *single-electron transport spectroscopy*. This provides a very powerful tool for investigating the properties of quantum dots (Sohn 1997).

1.4 Scanned Probe Measurements

Electron transport measurements are very useful for investigating the energetics of mesoscopic systems. They suffer, however, from a lack of spatial discrimination: it is difficult to tell which part of the sample is responsible for which part of the observed behaviour. This is because by their very nature transport measurements probe the entire system at once. Understanding the microscopic mechanisms responsible for the behaviour, however, often requires the ability to probe and manipulate only one small portion of the system at a time. The desire to study the local properties of mesoscopic systems has led to the recent development of a new generation of low-temperature scanned probe techniques that are well suited to investigating electronic properties in low-dimensional systems.

Some of these techniques are designed as non- or minimally-perturbative probes capable of measuring the intrinsic properties of the system. Electrostatic force microscopy has been used to perform electrometry (Schönenberger 1990), to measure local contact potentials (Nonnenmacher 1991), and to measure local electrostatic potentials (Martin 1988, McCormick 1998a, Bachtold 2000). Scanned capacitance measurements have also been used to measure the local electrostatic potential, as well as the local compressibility of the electrons (Tessmer 1998, Finkelstein 2000). A scanned single-electron transistor has been used as yet another way to perform electrometry and measure both the local elec-

trostatic potential and the electronic compressibility (Yacoby 1999, Zhitenev 2000). And of course scanning tunnelling microscopy remains a very useful technique for local spectroscopic and structural measurements (Odom 1998, Wildöer 1998, LeMay 2001).

Other techniques have been developed to explore the response of the system to deliberate perturbations. Scanned gate microscopy has been used to electrostatically perturb the system and image electron orbits under various conditions (Eriksson 1996, Crook 2000, Topinka 2000 and 2001). It has also been used to study scattering from potential perturbations and impurities (Bachtold 2000, Tans 2000, Bockrath 2001, Woodside 2001). In another approach, atomic force microscopes have been used to mechanically perturb and manipulate conductors, for instance by compressing or stretching them, changing their shape, or cutting them (Tomblor 2000a, Bozovic 2001, Postma 2001).

All of these approaches have provided valuable insights into the microscopic properties of the systems studied. In the work presented here, we use two particular techniques. To measure the local electrostatic potential, we apply electrostatic force microscopy, while to study scattering centers and single-electron charging, we apply scanned gate microscopy. These measurements are made with a low-temperature atomic force microscope specially designed to study the electronic properties of low-dimensional systems.

1.5 Outline

The rest of this dissertation will present research into the local electronic properties of two specific low-dimensional systems, 2D electron gases in the quantum Hall regime and 1D carbon nanotubes, using scanned probe microscopy. Chapter 2 will provide a description of the low-temperature atomic force microscope used in this research and how it can be used to measure the electronic properties of these systems. The specific experimental techniques employed, electrostatic force microscopy and scanned gate microscopy, will be discussed in detail in this chapter. Chapter 3 will introduce the integer Quantum Hall Effect in 2D electron gases. Electrostatic force microscopy will be used to investigate the local electrostatic potential distribution associated with non-equilibrium currents in a quantum Hall conductor. A measurement of local equilibration rates in this chapter will lead in Chapter 4 to an investigation of the individual scattering centers responsible for equilibration in the quantum Hall regime. Chapter 5 will turn from 2D electron gases to 1D carbon nanotubes, reviewing transport in carbon nanotubes as well as previous scanned probe studies. In Chapter 6, scanned gate measurements of nanotubes at the single-electron level will be discussed, while in Chapter 7, scanned force measurements of nanotubes at the single-electron level will be presented. Finally, Chapter 8 will briefly outline questions that remain to be answered and directions for future work.

CHAPTER 2: *The Low-Temperature Atomic Force
Microscope*

2.1 Introduction

Since its invention in 1986 (Binnig 1986), the atomic force microscope (AFM) has developed into a powerful and versatile tool with applications in many fields of science. The strength of the AFM lies in its combination of high spatial resolution and excellent force sensitivity coupled with a very robust force sensing mechanism that can operate in many different environments (Sarid 1994, Wiesendanger 1994). It is easily adapted to sense a variety of forces (*e.g.* van der Waals, frictional, electric, magnetic, chemical, ...) or to probe other properties of the sample altogether (*e.g.* electronic, thermal, ...). The AFM can also be used not just to sense forces but to apply them, providing a microscopic probe with which to manipulate samples as desired. Because of these features, atomic force microscopy is proving to be an invaluable tool for fields as diverse as biology, chemistry, materials science, engineering, and physics.

The basic concept of the AFM is very simple: a sharp tip is mounted on the end of a soft cantilever and placed above the sample to be studied. The cantilever behaves like a spring, so that any forces acting on the AFM tip cause the cantilever to deflect (Fig. 2.1). By monitoring the motion of the cantilever through one of a variety of techniques (Sarid 1994), we can then measure the force being applied to the tip. For example, if the tip is brought into contact with the sample surface, then inter-atomic repulsion between tip and

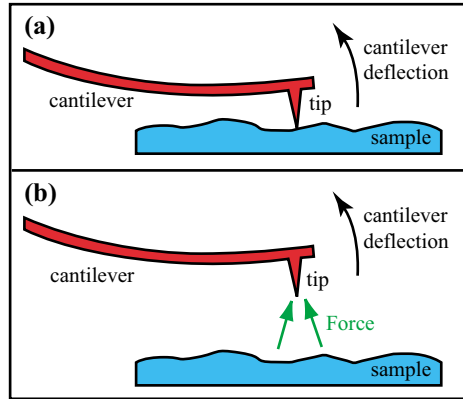


Fig. 2.1: Principle of operation of the atomic force microscope (AFM): a sharp tip senses the force from the sample, which is measured by detecting the deflection of the cantilever. **(a)** In contact mode AFM, the tip is in contact with the sample surface. **(b)** In non-contact AFM, the tip is held just above the sample surface.

sample deflects the cantilever, and the sample topography can be imaged. Measurement with the tip in contact with the surface is known as *contact mode AFM*. If the tip is held above the surface, then longer-range forces such as the electrostatic force can be measured. This is known as *non-contact AFM*. The tip can also be used to perturb the sample, for instance by applying electric fields or mechanical stresses to the sample. Many different feedback and control systems are employed to implement the various incarnations of atomic force microscopy. In essence, however, the AFM is simply a force transducer, translating forces on the tip into mechanical motion of the cantilever.

The dynamics of AFM cantilever motion are reviewed in section 2.2. This is followed in sections 2.3 and 2.4 by a discussion of the forces acting on the AFM tip (primarily electrostatic) that will be relevant for the experiments described later. The design of the low-temperature AFM used in the experiments is reviewed in section 2.5. The chapter concludes with a discussion in sections 2.6 and 2.7 of the principal measurement tech-

niques used in this work: electrostatic force microscopy (EFM) and scanned gate microscopy (SGM).

2.2 AFM Cantilever Dynamics

In order to use the AFM to measure forces, we need to understand the dynamics of the response of the tip and cantilever to an applied force. This is most easily done by modelling the cantilever and tip assembly as a damped simple harmonic oscillator (see, for example, Sarid 1994). For small displacements z , the cantilever acts as a linear spring, obeying Hooke's law $F = kz$, where k is the spring constant. The equation of motion of the tip in response to an applied force $F(t)$ is then:

$$m \left(\frac{d^2 z}{dt^2} \right) + \gamma \left(\frac{dz}{dt} \right) + kz = F \quad (2.1)$$

Here m is the effective mass of the tip-cantilever system, and γ is a damping term (*e.g.* due to air resistance or defects in the lever).

For a periodic driving force $F(t) = F \cos(\omega t)$, the response $z(t)$ is also periodic, $z(t) = A \cos(\omega t - \theta)$, with:

$$A(\omega) = \frac{F}{k} \cdot \frac{Q}{\sqrt{Q^2 (1 - (\omega/\omega_0)^2)^2 + (\omega/\omega_0)^2}} \quad (2.2)$$

$$\tan \theta = \frac{\omega_0 \omega}{Q(\omega_0^2 - \omega^2)} \approx \frac{1}{\omega_0 - \omega} \left(\frac{\omega_0}{2Q} \right) \quad (2.3)$$

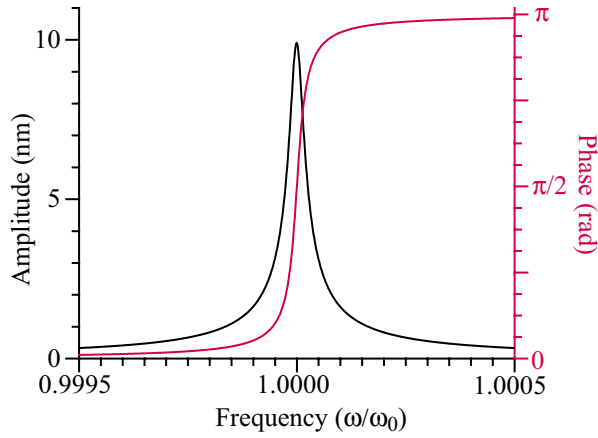


Fig. 2.2: Amplitude and phase response of a cantilever to a 1 pN driving force calculated from Eqs. 1.2 and 1.3, for a hypothetical cantilever with $k = 3$ N/m (similar to k of actual AFM cantilevers). The resonance Q is 30 000, typical for an AFM cantilever in vacuum at low temperature. A 1 pN driving force produces a 10 nm response on resonance, which is easily detectable. Note that the bandwidth of the resonance is extremely narrow, only 1 Hz for a cantilever with a typical resonance frequency of 30 kHz.

This is the classic resonance response, where we have defined the resonance frequency ω_0 of the cantilever as $\omega_0 = \sqrt{k/m}$, and the quality factor Q of the resonance as $Q = (m\omega_0)/\gamma$. The smaller the damping, the larger the Q factor, and the larger the amplitude response to a given force. Q also sets the width of the resonance, as it is the ratio of the resonant frequency to the full width at half power.

Eqs. 2.2 and 2.3 describe the response of a freely-oscillating cantilever, which is the situation in non-contact AFM. To illustrate what this response looks like, in Fig. 2.2 we plot the response of a hypothetical cantilever to a 1 pN driving force calculated from Eq. 2.2 and 2.3. The cantilever in this calculation has a spring constant of $k = 3$ N/m and a resonance quality factor of $Q = 30\,000$, typical values for the actual AFM cantilevers used in the measurements we discuss later. We see that a small driving force (1 pN) produces on resonance a large displacement of the cantilever that can easily be detected. The high Q factors of AFM cantilevers allow them to sense very small forces on resonance.

Note that the high Q also results in a very narrow resonance linewidth: for example, a typical cantilever with a resonant frequency of 30 kHz and $Q = 30\,000$ has a resonance width of only 1 Hz.

The previous equations assume that the driving force is uniform. It is usually the case in non-contact AFM, however, that the force driving the tip is not simply uniform but varies slowly in space. In this case, we approximate the force by Taylor expanding it around the equilibrium position of the tip z_0 in terms of derivatives of the force:

$F(t) \sim [F(z_0) + F'(z_0)(z - z_0)] \cos(\omega t)$. The solution to the equations of motion becomes:

$$A(\omega) = \left(\frac{F(z_0)}{k'} \right) \left(\frac{\omega_0}{\omega_0'} \right)^2 \cdot \frac{Q}{\sqrt{Q^2 (1 - (\omega/\omega_0')^2)^2 + ((\omega\omega_0)/\omega_0'^2)^2}} \quad (2.4)$$

$$\tan \theta = \frac{\omega_0 \omega}{Q(\omega_0'^2 - \omega^2)} \quad (2.5)$$

The force derivative acts to change the effective spring constant, creating a new spring constant $k' = k - F'(z_0)$ and shifting the resonance frequency to:

$$\omega_0' = \sqrt{\frac{k'}{m}} \sim \sqrt{\frac{k}{m}} \left(1 - \frac{F'(z_0)}{2k} \right) \quad (2.6)$$

An attractive force, having a positive F' , thus effectively softens the cantilever and reduces the resonance frequency. Typical force gradients in the work that will be presented in later chapters involve frequency shifts of a few Hertz, or on the order of a few parts in 10^4 . Note that this frequency shift is larger than the typical width of the reso-

nance, and so has important effects. The changes in the response amplitude at resonance, however, are sufficiently small that they can be essentially ignored (Eq. 2.4). The principal effect of the force gradient is thus to shift the resonant frequency of the cantilever. (For further details on cantilever dynamics, see Sarid 1994 or Wiesendanger 1994).

Finally, we consider the force sensitivity of an AFM. The ultimate limit on the force sensitivity is set by the thermal vibrations of the cantilever: forces causing deflections smaller than the thermal vibration are clearly not easily measured. From the equipartition theorem, the thermal fluctuations at temperature T have an energy $E_{therm} = \frac{1}{2}k_B T$, where k_B is Boltzmann's constant. Equating this to the energy of the cantilever oscillation, we have $k\langle\delta z_N^2\rangle = k_B T$, where δz_N is the thermal displacement of the cantilever. Most of the response of the cantilever to thermal oscillations will be concentrated near the resonance frequency, however, as is clear from Fig. 2.2. Taking this into account, we can write the effective noise amplitude on resonance, $\delta z_{N,eff}$, as (Albrecht 1990):

$$\delta z_{N,eff} = \sqrt{\frac{4QBk_B T}{\omega_0 k}} \quad (2.7)$$

Here, B is the bandwidth of the measurement, which is assumed to be less than the resonance linewidth. The minimum force that can be measured on resonance, and hence the ultimate force sensitivity of the AFM, is therefore:

$$F_{min} = (k/Q) \cdot \delta z_{N,eff} = \sqrt{\frac{4Bkk_B T}{Q\omega_0}} \quad (2.8)$$

We will use these equations in section 2.5 to calculate the force sensitivity of the low temperature AFM used in the experiments reported in subsequent chapters.

2.3 Electrostatic Force on the AFM Tip

A large part of the versatility of the AFM as an experimental tool comes from its ability to sense many different types of forces. In this work, we will use the AFM to probe electrostatic forces. Since the tip and the sample are two conducting surfaces that together form a capacitor, we can calculate the electrostatic force F_{es} on the AFM tip in terms of the tip-sample capacitance C . The energy U stored in a capacitor with capacitance C is well known: $U = \frac{1}{2}C(\Delta V)^2$, where ΔV is the electrostatic potential difference between the plates of the capacitor. The force in the z direction normal to the tip is then:

$$F_{es} = \frac{1}{2}C'(\Delta V)^2 \quad (2.9)$$

where $C' = \frac{dC}{dz}$ is the derivative of the capacitance. This expression includes the work done to maintain the potential difference at a constant value (Jackson 1975).

For small amplitude oscillations around the equilibrium height of the tip above the sample, z_0 , the force may be Taylor expanded in terms of the capacitance derivatives:

$$F_{es}(z) \sim \frac{1}{2}C'(z_0)(\Delta V)^2 + \frac{1}{2}C''(z_0)(\Delta V)^2 \cdot (z - z_0) \quad (2.10)$$

This implicitly assumes that $\Delta V \neq \Delta V(z)$, an assumption that we will see later breaks down in some situations. Comparing this result to Eqs. 2.4 and 2.6, we see that the first term sets the amplitude of the cantilever response, while the second term changes the spring constant of the cantilever and sets the frequency shift of the oscillation. Thus the amplitude of the response varies as C' while the frequency shift varies as C'' . Both terms are quadratic in the electrostatic potential difference between the tip and the sample.

The force on the tip depends on the derivatives of the tip-sample capacitance. These can be calculated easily for simple approximations to the tip-sample geometry. For example, approximating the tip and sample as parallel disks with radius R equal to the radius of curvature of the tip, the capacitance is $C \sim (4\pi\epsilon_0 R^2)/z$, and the first derivative is $C' = -(4\pi\epsilon_0 R^2)/z^2$. As expected for an electrostatic interaction, the force on the tip is long range, dying off slowly as the tip moves away from the sample. In fact, this approximation underestimates the capacitance by ignoring the sides of the conical AFM tip. A full numerical calculation of the capacitance for a realistically-shaped AFM tip sitting above a planar sample shows that the capacitance derivative is even more long range, with $C' \propto z^{-1/2}$ at tip heights of $z \sim 100$ nm, due to the effects of the conical sidewalls (Belaidi 1997). This is indeed the distance dependence measured for a tip sitting above a 2D electron gas (McCormick 1998a).

To give an idea of the order of magnitude of the electrostatic force on the AFM tip, we calculate F_{es} under typical experimental conditions. Previous measurements of the capacitance derivative C' over a 2D electron gas (McCormick 1998b) found that $C' \sim 5 \times 10^{-11}$ F/m at a tip height of $z \sim 50$ nm. With a typical dc electrostatic potential difference of $\Delta V \sim 0.5$ V between the tip and the sample, we find from Eq. 2.9 that the dc electrostatic force on the tip is $F_{es} \sim 5$ pN.

In actual experiments, the cantilever is deflected not just by the force on the AFM tip, but also by the force on the cantilever itself. For short range forces this is negligible,

since the cantilever is far away from the sample (typically 3 μm or more, compared to a tip-sample separation on the order of 50-100 nm). For long range forces such as the electrostatic force, however, the force on the cantilever produces a significant deflection. Empirically, the force on the cantilever has been observed to be of the same order of magnitude as the force on the tip, typically accounting for about 1/2 of the total cantilever deflection (McCormick 1998b). Fortunately, the force on the cantilever shows much slower spatial variation than the force on the tip, because of the large area of the cantilever ($\sim 500 \mu\text{m}^2$) and its height above the sample. It can thus usually be ignored as a constant, non-local signal on top of the local signal from the tip in which we are interested.

Finally, we note that the tip will also be affected by van der Waals forces, in addition to the electrostatic forces in which we are interested. In contrast with the electrostatic force, the van der Waals force, which is due to the interaction between instantaneously induced dipoles in the tip and sample, is a short range interaction. It can be calculated by approximating the tip as a sphere of radius R at a height z above an infinite plane. For $z \ll R$, the force is:

$$F_{vdW} \sim \frac{AR}{6z^2} \quad (2.11)$$

where A is the Hamaker constant, $A \sim 10^{-19}$ J (Israelachvili 1992). For $z \gg R$, the distance dependence falls from z^{-2} to z^{-3} . At a typical tip radius of 50 nm and height above the sample of 50 nm, the van der Waals force is ~ 0.3 pN. As this is an order of magnitude smaller than the electrostatic force, the van der Waals force can be safely ignored in the work that follows.

2.4 Contact Potential and Fixed Charges

In Eqs. 2.9 and 2.10, the electrostatic force on the sample is expressed in terms of the electrostatic potential between the tip and the sample. Experimentally, however, voltage sources set the electrochemical potential rather than the electrostatic potential. This has some important practical ramifications. In particular, if the tip and sample are made of different materials, then they will have different workfunctions. When the tip and sample are connected electrically as done here, the electrochemical potential is the same in both, but the workfunction (chemical potential) difference leads to an additional electrostatic potential difference between tip and sample, called the contact potential (Fig. 2.3). This is analogous to the electrostatic potential induced in a semiconductor *pn* junction by the chemical potential difference between the differently-doped sections (Ashcroft 1976). The value of the contact potential is just equal to the difference between the two workfunctions.

If the voltages on the tip and sample are V_{tip} and V_{sample} , respectively, then the actual electrostatic potential between the tip and the sample ΔV is given by:

$$\Delta V = V_{tip} - V_{sample} - \Phi \quad (2.12)$$

where Φ is the contact potential difference between the tip and the sample. The value of the contact potential depends on the materials of the tip and sample, but is typically on the order of a few hundred mV. In fact, the exact value of the contact potential depends on the details of any charged dipole or monopole layers at the surfaces of the sample and tip

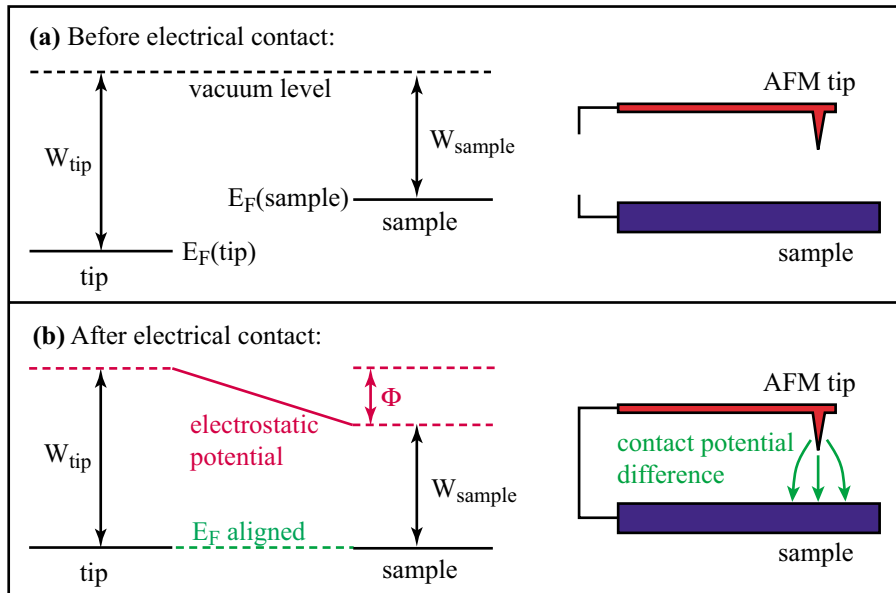


Fig. 2.3: Contact potential between tip and sample. **(a)** The tip and sample are made of different materials and so have different workfunctions, W_{tip} and W_{sample} . **(b)** Electrical contact between tip and sample aligns the electrochemical potential E_F , giving rise to an electrostatic potential between the tip and sample known as the contact potential, $\Phi = W_{tip} - W_{sample}$.

(Ashcroft 1976). It is thus not a constant for any pair of materials but must be measured experimentally. The easiest way to measure the contact potential is to vary $V_{tip} - V_{sample}$ until the electrostatic force on the tip vanishes (Eq. 2.9), a variation on the Kelvin probe method (Nonnenmacher 1991). The contact potential is then just equal to the value $V_{tip} - V_{sample}$.

This picture is complicated by the effect of fixed charges on the surface of the sample or the tip. Such charges establish yet another electric field between the tip and the sample which contributes to the electrostatic potential difference between them. A fixed charge on the sample will induce an image charge on the AFM tip of the opposite sign. This image charge on the tip then interacts electrostatically with the sample, effectively

altering the tip voltage experienced by the sample. For example, a negative charge on the sample surface will induce a positive image charge on the AFM tip, effectively increasing the potential difference ΔV between the sample and the tip. Because there are usually many fixed charges on or near the sample surface (charges in oxide layers, nearby dopants, charged dirt, ...), the value of the effective contact potential can vary significantly as the tip is moved around over the surface. For example, Yoo *et al.* (1997) reported spatial variations of 50 mV for 2D electron gas systems, while McCormick *et al.* (1998a, 1999) found even larger variations, on the order of 100 mV or more. In addition, since the charges on the surface and tip can change with time, there can be similarly large temporal variations in the contact potential (examples will be shown in subsequent chapters). These variations in the contact potential can cause significant variations in the electrostatic force, and must therefore be properly taken into account in the measurements.

2.5 AFM Design and Performance

We next turn to the design of the AFM used to make the measurements reported in later chapters. As mentioned above, this AFM is designed specifically to make electrostatic measurements of mesoscopic samples at low temperatures. A detailed description of the construction of this home-built machine is given elsewhere (McCormick 1998b). Here, we provide only a brief overview of the design.

The layout of the AFM is shown in Fig. 2.3. A commercial AFM tip made of Si is coated with a 25 nm thick layer of Ti and mounted on a scan head. The scan head contains

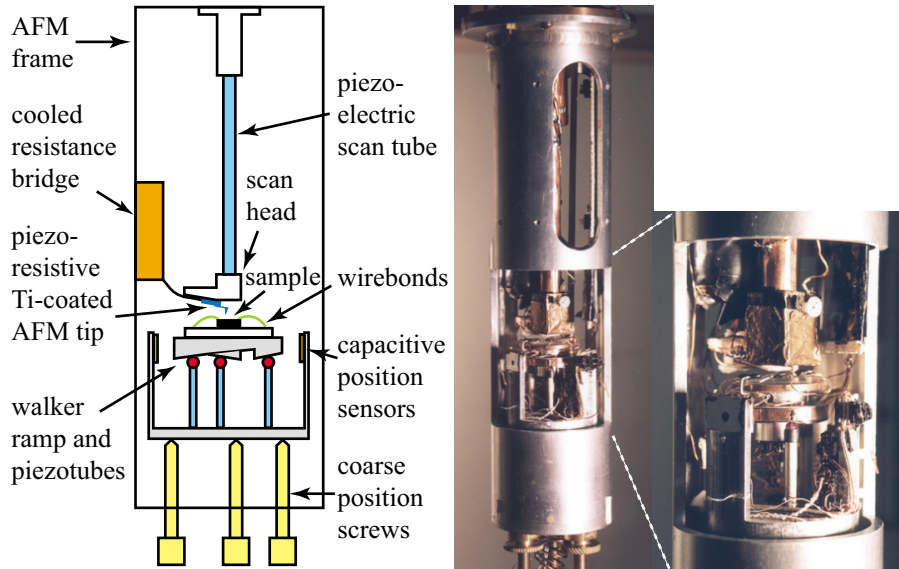


Fig. 2.4: Design of low-temperature AFM: schematic and photographs of the instrument.

a piezoelectric driver used to oscillate the cantilever mechanically. This scan head is attached to a 4-inch long 4-quadrant piezoelectric scan tube providing fine position control of the tip in all three axes. The sample sits on a Besocke-style walker (Besocke 1986) providing coarse positioning in all three axes, with a range of almost 1 mm in z (vertical axis) and over 3 mm in x and y (horizontal axes). Coarse lateral position sensing is provided by three parallel plate capacitors around the sample. Up to 20 electrical leads on the walker allow transport measurements to be performed while scanning the AFM tip. This whole assembly is attached to a ^3He cryostat, placed in a 7 T superconducting magnet, and cooled to 600 mK.

The force on the tip is sensed with a piezoresistive cantilever (Tortonese 1993).

This is a cantilever made of Si that has doped conducting channels running down the

length of the cantilever. Deflection of the cantilever deforms the band structure of the Si, changing the resistance of the conducting channels (Seeger 1991). We incorporate this piezoresistive cantilever into a Wheatstone bridge cooled to the base temperature of the cryostat, so that the cantilever deflection is monitored simply by measuring the resistance of the cantilever. The deflection signal from the resistance bridge is then amplified by a home-built low-noise amplifier before being passed to the computer controlling the AFM. The electronics and software used to control the AFM were all built in-house also, and are discussed in greater detail elsewhere (McCormick 1998b).

Since force measurements with an AFM depend on measuring small motions of the cantilever, the AFM has to be isolated vibrationally from the environment in order to achieve high force sensitivity and high spatial resolution. This is particularly important for the instrument used here because the long scan tube and AFM frame have low-frequency resonances. A three-stage vibration isolation system is used. First, the AFM is suspended from the ^3He cryostat by long weighted springs, in order to cut off vibrations from He boil-off in the bath and acoustic coupling through the dewar. The dewar is then hung from a heavy air table, and finally the air table is supported by massive pillars sitting on alternating steel and rubber plates.

The vertical spatial resolution of the AFM can be determined by measuring the noise in the height z of the AFM tip above the sample. To do this we park the tip at a point over the sample and bring it into contact with the sample. Any noise in z then deflects the

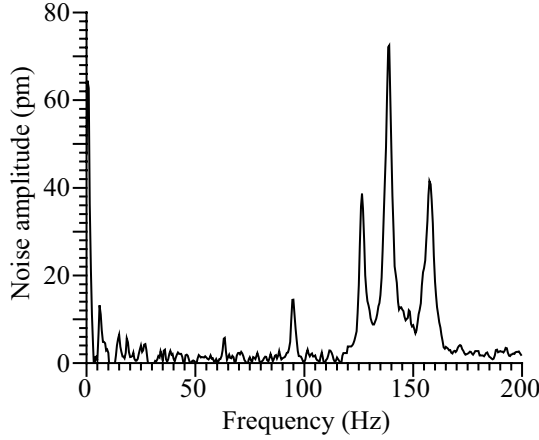


Fig. 2.5: Power spectrum of the AFM cantilever deflection due to noise in z , measured at 600 mK with the tip in contact with the sample. Several strong resonances are visible near 150 Hz. There are no major resonances above 200 Hz. The integrated noise in z is 0.25 nm.

cantilever, so that the power spectrum of the cantilever deflection provides a direct measure of the noise spectrum in z . Such a measurement of the power spectrum of the cantilever in contact with the sample is shown in Fig. 2.5, at $T = 600$ mK. Several strong resonances are visible near 150 Hz, accounting for the largest part of the noise power. There are no significant resonances above 200 Hz (not shown). Calculating the vibrational noise amplitude δz_N from the measured power spectrum $P(\omega)$, using the definition:

$$\langle \delta z_N^2 \rangle = \frac{1}{2\pi} \int_{-\infty}^{\infty} P(\omega)^2 d\omega \quad , \quad (2.13)$$

we find that the noise in z is $\delta z_N \sim 0.25$ nm. The vertical spatial resolution is thus 0.25 nm. The lateral spatial resolution, determined crudely from contact scans, is on the order of 10 nm or better. Note that since we measure only electrostatic forces, which are long range, we do not have a requirement for very high lateral resolution.

Finally, we determine the force sensitivity of the AFM at resonance. The noise in the detection system and electronics is sufficiently low that the sensitivity is limited by

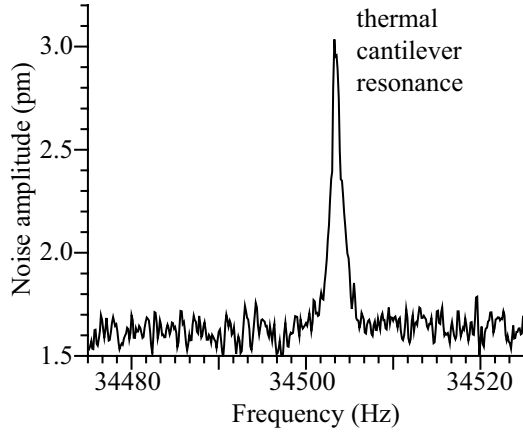


Fig. 2.6: Power spectrum of the AFM cantilever deflection near resonance, measured at $T \sim 5$ K. Here the tip is not in contact with the sample, and the cantilever oscillates freely due to thermal noise. The thermal cantilever oscillation on resonance at 34 502 Hz is clearly seen above the background noise, indicating that the force sensitivity on resonance is thermally limited. The force sensitivity measured here is $300 \text{ aN/Hz}^{1/2}$.

thermal oscillations (McCormick 1998b). We measure the thermal oscillation of the cantilever from a power spectrum near resonance of the cantilever deflection. Here the tip is not in contact with the sample; rather, the cantilever is free to oscillate due to thermal noise. A power spectrum of the cantilever deflection near resonance measured at $T \sim 5$ K for one of the AFM tips used in subsequent chapters is plotted in Fig. 2.6. The thermal oscillation of the cantilever clearly rises out of the background noise at the resonant frequency of the cantilever, 34 502 Hz. When we average several such measurements, we observe an effective noise on resonance of $\delta z_{N,eff} \sim 3.5 \text{ pm/Hz}^{1/2}$ at $T \sim 5$ K. Using Eq. 2.8 with the measured values for this cantilever $Q \sim 31\,000$ and $k \sim 3 \text{ N/m}^1$, we calculate that we achieve a force sensitivity of $F_{min} \sim 300 \text{ aN/Hz}^{1/2}$.

The AFM thus has exquisite sensitivity when measuring forces on resonance, due to the high Q of the cantilever. For purposes of comparison, the best force sensitivity that

1. The spring constant k of these cantilevers is quoted by the manufacturer as 1 N/m . This is only a nominal value, however, and k can vary significantly from one cantilever to the next. We determine $k = 3 \pm 0.5 \text{ N/m}$ for this cantilever from the magnitude of the thermal deflection on resonance using Eq. 2.7.

has been reported using an AFM on resonance is $3 \text{ aN/Hz}^{1/2}$ (Stipe 2001), 100 times smaller than the sensitivity of our instrument. This improvement in the sensitivity is achieved by using extremely soft cantilevers with a spring constant $k \sim 10^{-5} \text{ N/m}$, which are not suitable for the measurements we perform.

The parameters describing the performance of the AFM for a typical tip and cantilever are summarised in Table 2.1 below:

TABLE 2.1

| Parameter | Typical value |
|--|---------------------------|
| Resonant frequency ω_0 | 34 500 Hz |
| Resonance width $\Delta\omega$ | 1.1 Hz |
| Resonance Q factor | 31 000 |
| Cantilever spring constant k | 3 N/m |
| Force sensitivity on resonance F_{min} | $300 \text{ aN/Hz}^{1/2}$ |
| Vibrational noise amplitude δz_N | 0.2 nm |

2.6 Measurement Techniques: Electrostatic Force Microscopy

We use the AFM to make two broad classes of electrostatic measurements: electrostatic force microscopy (EFM) and scanned gate microscopy (SGM). In this section we will present the principles of EFM, discussing SGM in the following section. EFM senses the electrostatic force on the tip from the sample, and can be used for such experiments as measuring the force from localised charges (Stern 1988, Schönenberger 1990) or measuring the local electrostatic potential in a sample (Martin 1988, McCormick 1998a). In this work we use EFM to measure the potential distribution in quantum Hall conductors as well as the force from single-electron motion in carbon nanotubes.

There are two common classes of EFM measurements, shown schematically in Fig. 2.7 below. The first is dc-EFM, illustrated in Fig 2.7(a). In dc-EFM, a voltage V_{tip} biases the AFM tip with respect to the sample. A dc bias V_{dc} is applied across the sample, establishing in the sample a electrostatic potential distribution $V_{dc}(x,y)$ which we would like to measure. The cantilever is then driven mechanically at a frequency near the resonance. The local potential difference between tip and sample changes as the tip moves in the (x,y) plane, leading to spatial variations in the force derivative (Eq. 2.10):

$$F'(x, y) = \left(\frac{1}{2}\right) C''(x, y) \cdot (V_{tip} - V_{dc}(x, y) - \Phi(x, y))^2$$

This causes a spatially-varying shift in the resonance frequency, which is monitored by measuring the phase of the cantilever vibration. Since this is a dc technique, however, there is no way to discriminate between the effects of a spatially varying sample voltage

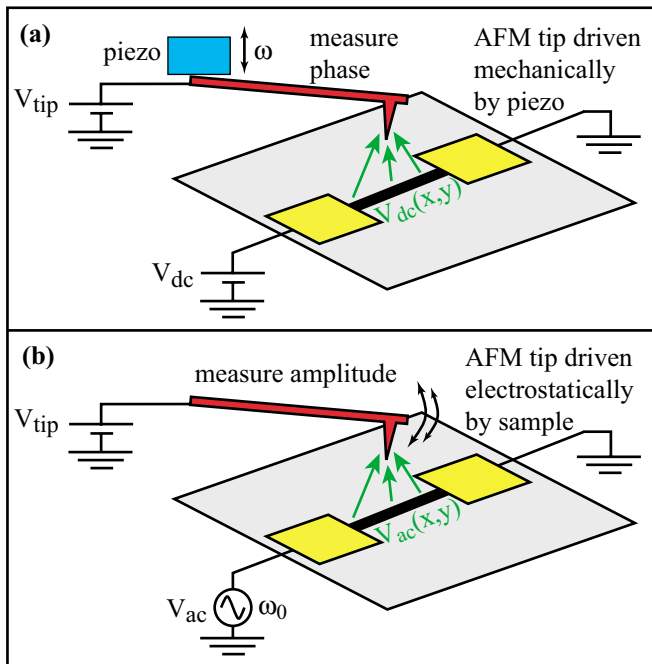


Fig. 2.7: Electrostatic Force Microscopy (EFM). **(a)** dc-EFM. A voltage V_{tip} is applied to the AFM tip and the cantilever is driven mechanically near resonance. A dc source-drain bias V_{dc} is applied across the sample, giving rise to a potential distribution $V_{dc}(x,y)$ in the sample. The local potential difference between tip and sample exerts a force on the tip, whose gradient changes the resonant frequency. This is monitored via the phase response of the cantilever. **(b)** ac-EFM. A voltage V_{tip} is applied to the tip. An ac source-drain bias at the resonant frequency of the cantilever is applied to the sample. The local potential in the sample, $V_{ac}(x,y)$, exerts an ac force on the tip that causes the cantilever to resonate. Here the amplitude rather than the phase of the response is measured.

and a spatially varying contact potential. As a result, dc-EFM is only useful for measuring sample voltage changes that are much larger than the typical contact potential variations. For the samples studied here, local contact potential variations are on the order of 100 mV, as previously mentioned, while the sample voltages being measured are on the order of 1 mV or less. Thus, dc-EFM is of little use.

Instead, the ac-EFM technique shown schematically in Fig. 2.7(b) is used. Here, a dc potential V_{tip} is still applied to the AFM tip, but an ac voltage at the resonant frequency of the cantilever, $V_{ac}\cos(\omega_0 t)$, is applied to the sample. This ac voltage sets up a potential distribution in the sample, $V_{ac}(x,y)$, which exerts an ac force on the tip that causes the cantilever to resonate. The force on the tip, neglecting the component at $2\omega_0$, is now:

$$F \approx F_{dc} + F_{\omega_0} \cos(\omega_0 t)$$

$$F_{dc}(x, y) = \left(\frac{1}{2}\right) C'(x, y) \cdot \left[(V_{tip} - \Phi(x, y))^2 + \frac{1}{2} V_{ac}(x, y)^2 \right]$$

$$F_{\omega_0}(x, y) = C'(x, y) \cdot [V_{tip} - \Phi(x, y)] V_{ac}(x, y) \quad (2.14)$$

By measuring the component of the force at ω_0 using a lock-in amplifier, we can measure the potential distribution in the sample, $V_{ac}(x,y)$. In contrast to the dc-EFM technique, we here monitor the amplitude response of the cantilever rather than the phase response. Note that we must still remove the spatial variations due to the contact potential (and also the capacitance derivative). Because these contributions are multiplicative rather than additive as in dc-EFM, however, they can be removed without difficulty by a normalisation procedure described later.

This ac-EFM technique works quite well and has been successfully applied to measure the local electrostatic potential in 2D electron gases and in carbon nanotubes, as will be discussed in subsequent chapters. There are two important subtleties, however, regarding how the tip is driven into resonance by the electrostatic force. First, it is essential to ensure that the driving frequency remain on resonance at all times, in order to avoid spurious signals in the amplitude response due to frequency changes (Eq. 2.4). In particular, as the tip moves, the resonant frequency changes due to spatial variations in the contact potential or the capacitance derivative (Eq. 2.14). In vacuum at low temperatures, these frequency shifts can be significant compared to the width of the cantilever resonance, which is typically only 1 Hz. They can thus introduce large amplitude modulations that have nothing to do with the local electrostatic potential distribution we want to measure.

To avoid problems from the response of the cantilever to frequency shifts, we drive the cantilever with the self-resonant positive-feedback loop drawn in Fig. 2.8. The cantilever deflection is sent through a phase shift compensator and thence to a limiter, whose output amplitude is independent of its input amplitude. The limiter output is then applied to the sample electrodes to drive the cantilever electrostatically into resonance. The amplitude of the oscillation is measured

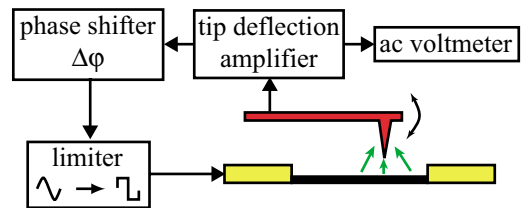


Fig. 2.8: Self-resonant feedback loop for ac-EFM. The tip deflection is fed back as a constant-amplitude driving signal to the sample electrodes. A phase shifter is used to compensate for phase changes in the feedback loop. The cantilever oscillation amplitude is measured using an ac voltmeter.

directly from the tip deflection amplifier using an ac voltmeter. This feedback loop ensures that the cantilever always remains on resonance as the tip moves over the sample (Albrecht 1990, McCormick 1998a). Note that this method does have some disadvantages. The feedback can be non-linear, especially at low amplitudes, so that care must be taken to remain always in the linear regime. A lock-in amplifier can not be used to measure the oscillation amplitude directly, since the frequency changes too rapidly. And finally, the bandwidth of the amplitude response is only ~ 1 Hz, due to the narrow cantilever resonance, so that these measurements are very slow.

A second subtlety involved in the ac-EFM measurement is that spatial variations in Φ and C' also give spurious amplitude responses, as can be seen from Eq. 2.14. We can remove these by measuring the amplitude of the cantilever response at resonance when a uniform ac voltage is applied to the sample, so that $V_{ac}(x, y) = V_{ac}$. Any variations in the amplitude response to this uniform driving signal are then due to the prefactor in Eq. 2.14, $C'(x, y)(V_{tip} - \Phi(x, y))$. This reference signal can therefore be used to normalise the response to the non-uniform potential distribution we desire to measure. When this is done, the only spatial dependence that remains is due to the potential distribution in which we are interested. For practical reasons, the reference signal is measured at the same time as the desired signal by locking in to an amplitude modulation of the tip response at a different frequency (McCormick 1998b). This technique is used for the EFM measurements of a 2DEG presented in Chapter 3.

A final consideration with EFM involves the issue of the perturbation of the sample induced by the measurement. In principle, EFM should be made as a non-perturbative measurement, since we do not want to modify the electrostatic potential in the sample. In practice, however, a voltage must be applied between tip and sample (Eq. 2.14), and hence the sample is perturbed. In order to minimise the perturbation, ΔV is kept as low as possible, consistent with a measurable EFM signal (typically around 500 mV or less). This issue will be discussed in more detail in later chapters.

2.7 Measurement Techniques: Scanned Gate Microscopy

The second technique we use for probing the electrostatic properties of our samples is scanned gate microscopy (SGM). With EFM, as has been described, we use the AFM tip to measure the electrostatic potential of the sample. With scanned gate microscopy (SGM), on the other hand, we use the AFM tip to perturb the electrostatic potential of the sample. The basic idea of SGM is that the tip is not a force sensor but rather a movable local gate. We can therefore make transport measurements just as with samples that use a fixed gate (such as a planar backgate) to change the electrostatic potential, except that now we can choose which part of the sample to perturb, since the gate (the AFM tip) will change the electrostatic potential only in that part of the sample beneath the tip.

The measurement configuration for SGM is illustrated in Fig. 2.9. A dc potential V_{tip} is applied to the tip, while a current is passed through the sample. The conductance of the sample is then measured as the tip is scanned over it. The tip bias locally changes the

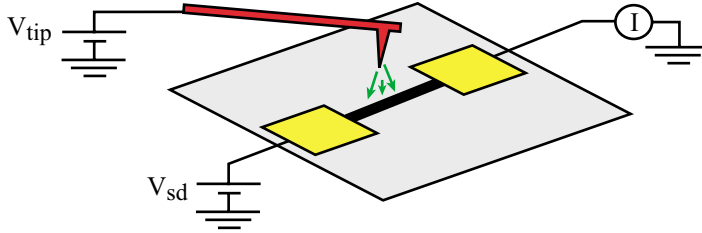


Fig. 2.9: Scanned gate microscopy (SGM). A source drain voltage V_{sd} is applied across the sample and the sample conductance is measured. A voltage V_{tip} is applied to the AFM tip. Changing the tip voltage or position changes the electrostatic potential of the sample, altering the conductance.

electrostatic potential of the sample, altering the conductance. By scanning the tip over the sample with a fixed tip voltage, SGM can thus be used to make images revealing the locations that are particularly sensitive to changes in the electrostatic potential. By parking the tip over one of these locations and varying the tip voltage, such sensitive areas can also be studied individually. SGM has been used to study conduction orbits (Eriksson 1996, Crook 2000, Topinka 2000 and 2001), scattering centers (Bachtold 2000, Tans 2000, Bockrath 2001, Woodside 2001), and charging effects in quantum dots (as we shall see in Chapter 6).

We can approximate the electrostatic potential perturbation from the AFM tip by crudely modelling the tip as a charged sphere sitting at a height z above the sample. The potential from this charge is what perturbs the sample. For a tip-sample bias $\Delta V = V_{tip} - \Phi$ and capacitance C , the charge on the tip is $q_{tip} = C \cdot (V_{tip} - \Phi)$. The potential perturbation $\delta\phi$ at the point (x_0, y_0) when the tip is located at the point (x, y) is therefore:

$$\delta\phi(x_0, y_0) = \left(\frac{1}{4\pi\epsilon} \right) \frac{C \cdot (V_{tip} - \Phi)}{\sqrt{(x - x_0)^2 + (y - y_0)^2 + z^2}} \quad (2.15)$$

This toy model captures several of the important features of SGM. For instance, it is clear that the perturbation is not truly local, because of the long-range nature of electrostatic forces. We also see that variations in tip distance and tip voltage are in a sense equiv-

alent in scanned gate measurements: the perturbation $\delta\phi$ can be changed equally well by increasing V_{tip} at a constant tip position as by moving the tip closer with a constant V_{tip} . Finally, when scanned gate images are made at fixed V_{tip} , a given perturbation $\delta\phi$ at (x_0, y_0) will occur not just for a single tip location (x, y) , but for the entire circle of points the same distance from (x_0, y_0) . This circle describes the equipotential surfaces of the perturbation for the given tip voltage. We thus expect that features in the scanned gate measurements may show up as equipotential rings.

Because the AFM tip is employed only as a source of electrostatic potential, the measurement is much simpler than with EFM. There is no need in SGM for complicated feedback systems to monitor and maintain resonant cantilever oscillations, as there is in EFM. Because the amplitude response of the cantilever is not being monitored (the cantilever is not oscillating), the measurement bandwidth is not limited by the resonance Q and the measurement is therefore much faster, too.

In practice, of course, the perturbation is much more complicated than the toy model in Eq. 2.15 suggests, and this gives rise to some subtleties that must be considered in actual measurements. For instance, this model neglects the effects of screening from nearby conductors and dielectrics. The presence of dielectrics and conductors can alter the shape and position of scanned gate features, in particular distorting the circular equipotentials predicted by Eq. 2.15, as will be seen in Chapters 4 and 6. Fixed charges on or near the sample surface also affect the measurements. For one thing, they produce their

own electrostatic perturbation of the sample, which can be screened by the conducting tip. The amount of screening changes as the tip moves, so that fixed charges can give rise to features in the scanned gate images, as will be seen in Chapter 6. Another effect of fixed charges is to induce image charges on the tip which effectively change the local contact potential and hence the electrostatic perturbation of the sample, as mentioned in section 2.4. In addition, large tip voltages can cause these charges to move around over time, changing the properties of the sample. Care must therefore be taken to ensure that the perturbation from the tip is not so large that charges are constantly being moved around. In practice, this typically restricts the tip voltage to the range $|\Delta V| \leq 1$ V (Woodside 2001).

2.8 Summary

In this chapter, we have seen how an atomic force microscope can be used to measure the force on the sensing tip by monitoring the motion of the AFM cantilever. We have also described the AFM that was built to measure the local electrostatic properties of mesoscopic systems at low temperatures, and we have discussed the two principal techniques that will be used to measure these properties: electrostatic force microscopy, and scanned gate microscopy. In the following chapters, we apply these techniques to two systems with different dimensionalities. In 2D, we study a 2D electron gas in the quantum Hall regime, investigating non-equilibrium populations in the quasi-1D edge states and inter edge state scattering (Chapters 3 and 4). Then in 1D, we study single-walled carbon

nanotubes, exploring single-electron charging effects in the 0D quantum dots that form in carbon nanotubes at low temperatures (Chapters 6 and 7).

CHAPTER 3: *Non-Equilibrium Edge State
Populations in Quantum Hall
Conductors*

3.1 Introduction

The first system we study is a two-dimensional electron gas (2DEG) in the quantum Hall regime. The quantum Hall effect was one of the first experimental surprises to be discovered in the study of transport in low dimensions (von Klitzing 1980). It has been explored intensively over the two decades since its discovery, leading to many new insights into the behaviour of electrons in low dimensions (for reviews, see Prange 1990, Das Sarma 1997) and ultimately two Nobel Prizes. Nevertheless, the quantum Hall effect continues to provide important challenges to both experimentalists and theorists.

Some of the most interesting questions concern the non-uniform spatial structures that can occur within the 2DEG in the quantum Hall regime. These structures arise from competition between the effects of Landau level (LL) quantization, Coulomb interactions, and external potentials and include striped phases (Lilly 1999) and insulating phases in the bulk (for a review, see Sondhi 1997) as well as conducting states localized at the edges of the sample, known as *edge states* (Halperin 1982, Büttiker 1988). Scanned probe techniques offer a new approach to investigate these structures directly. They have recently been used to probe the Hall voltage profile and the properties of the insulating state within a quantum Hall plateau (Tessmer 1998, McCormick 1999, Yacoby 1999, Finkelstein 2000,

Zhitenev 2000). In the work presented in the next two chapters we use a scanned probe to study the microscopic effects of the spatial structure in a 2DEG on electron transport by investigating non-equilibrium edge state populations. We first measure the potential distribution associated with them, and then investigate the scattering centers that are responsible for re-equilibration.

The basic physics of the integer quantum Hall effect will be reviewed in section 3.2, followed in section 3.3 by a more detailed discussion of the edge state structure in a quantum Hall conductor. Section 3.4 describes the GaAs/AlGaAs heterostructure used in the measurements. In section 3.5 we discuss how to create non-equilibrium edge state populations. Measurements of the local voltage distribution due to non-equilibrium edge state populations are then presented in section 3.6. This prepares the way for an investigation of equilibration and individual scattering centers in Chapter 4.

3.2 Integer Quantum Hall Effect

When a thin conducting strip is placed in a magnetic field B and a current I is passed through it, a transverse voltage V_H develops across the conductor. This is the well-known classical Hall Effect (Hall 1880), arising from the Lorentz force on charges moving in a magnetic field. The transverse (“Hall”) voltage V_H is directly proportional to the magnetic field. Expressed in terms of the transverse (“Hall”) resistance $R_{xy} = V_H/I$, we find

$R_{xy} = \frac{B}{nq}$, where n is the density of charge carriers and q is their charge (Kittel 1986). At

low temperatures and high magnetic field, however, this linear relationship breaks down.

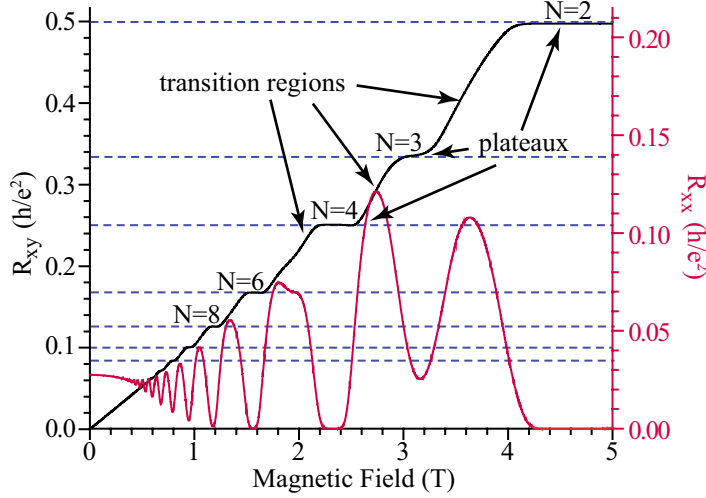


Fig. 3.1: Integer Quantum Hall Effect. At high magnetic fields B , the linear rise in the transverse resistance R_{xy} with B (classical Hall Effect) is modified by the appearance of plateaux in R_{xy} . On these plateaux, which are periodic in B^{-1} , R_{xy} is quantised in terms of the resistance quantum h/e^2 . In the same places that R_{xy} develops quantised plateaux, the longitudinal resistance R_{xx} dips to zero. These measurements shown here are made on the sample studied later in the chapter.

Instead, R_{xy} develops plateaux where its value is quantised in terms the resistance quantum h/e^2 : $R_{xy} = (1/N)(h/e^2)$, for integer N . These plateaux occur periodically in B^{-1} , whenever $N = \frac{nh}{eB}$. At the same time, the longitudinal resistance R_{xx} develops pronounced dips, becoming vanishingly small at the Hall resistance plateaux (Prange 1990). A measurement displaying the typical behaviour of R_{xx} and R_{xy} is shown in Fig. 3.1. Because of the quantised Hall resistance at integer values N , this is known as the integer quantum Hall effect (IQHE).

To understand the origin of the IQHE, we must consider the effect of strong magnetic fields on the electron motion. Classically, electrons in a magnetic field B move in cyclotron orbits with angular velocity $\omega_c = eB/m^*$, where m^* is the effective mass of the electron. At high magnetic fields, these classical cyclotron orbits become quantised, with energies $E_j = (j - 1/2)\hbar\omega_c$ for integer j . These are the well-known orbital Landau levels (LLs) separated by the cyclotron energy $\hbar\omega_c$. The spacing and degeneracy of the LLs

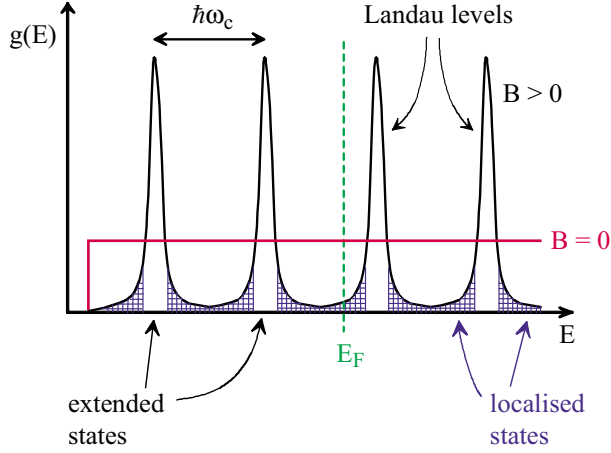


Fig. 3.2: Electronic density of states $g(E)$ of a 2DEG. At $B=0$, $g(E)$ is flat. In a magnetic field, the density of states splits into discrete Landau levels (LLs) separated by the cyclotron energy $\hbar\omega_c$. The LLs are broadened by the presence of disorder, so that there is a low density of localised states between the LLs. The only extended states lie at the core of the LLs. When the Fermi level E_F lies between LL energies, which occurs on the quantum Hall plateaux, the states at E_F are localised.

varies with B , and hence so does the number of occupied LLs, which is given by the filling factor $\nu = \frac{nh}{eB}$. Plotting the electronic density of states $g(E)$ in Fig. 3.2, we see that the flat $g(E)$ observed for 2D electrons at $B=0$ splits up into discrete LLs. In a perfectly ordered 2DEG, these LLs would be δ -functions at the energies E_j . The presence of disorder, however, broadens the LLs and introduces a low density of localised states between the LLs, as illustrated in Fig. 3.2. Note that the only extended states are at the LL energies; all other states are localised. As the filling factor changes with B , then, the Fermi level E_F lies alternately in regions of extended states (near half-integral ν) and localised states (elsewhere). The sample should thus be conducting near half-integral ν and insulating elsewhere.

This picture is not yet sufficient to explain the IQHE, because it neglects the finite size of the sample, and it turns out that the sample edges play a very important role in the IQHE (Halperin 1982, Büttiker 1988). At the edges, there is a rapidly rising confinement potential that keeps electrons inside the sample. This confinement potential raises the LL

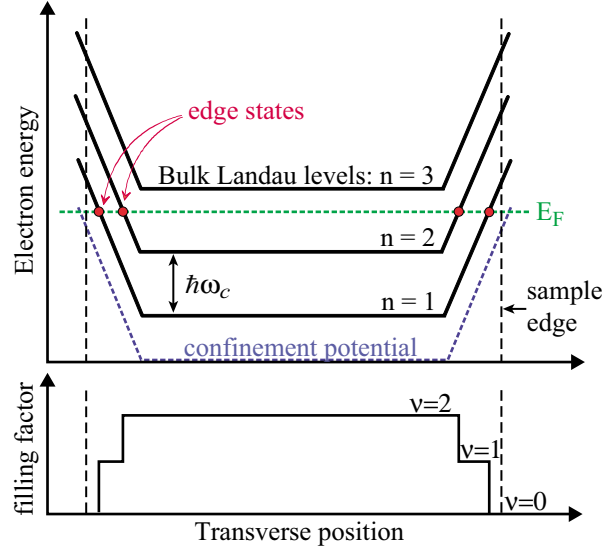


Fig. 3.3: Confinement potential and edge states in a finite sample. At the edge of the sample, the confinement potential that keeps electrons in the 2DEG raises the energy of the bulk LLs, until at some point near the edge the LLs cross E_F . These crossing points create extended states at E_F called edge states. Each edge state is a quasi-1D channel with conductance e^2/h . In this non-interacting model, the filling factor ν (number of filled LLs) changes abruptly by 1 at each edge state.

energies as the edges are approached, until at some point close to the edge the LLs cross E_F . Each occupied bulk LL thus gives rise to an extended state at E_F along the edge of the sample, called an *edge state* (Fig. 3.3). These edge states are effectively 1D channels that contribute to the conductivity at all filling factors. Due to the magnetic field, the edge states circulate around the sample, travelling in opposite directions on opposite sides of the sample. Note that as each LL crosses E_F , the filling factor is reduced by 1.

We can now understand the central features of the IQHE. Near integral $\nu \sim N$, as shown in Fig. 3.4(a), E_F lies between LLs, and the states at E_F in the bulk are all localised. The only extended states at E_F are the edge states, of which there are N . Since the edge states travelling in opposite directions are on opposite sides of the sample, *i.e.* they are separated by macroscopic distances, backscattering is suppressed and R_{xx} vanishes. The N 1D edge channels, however, result in a Hall conductance of $N(e^2/h)$ and hence a Hall resistance of $R_{xy} = (1/N)(h/e^2)$. Since the number of occupied extended states is unchanged as

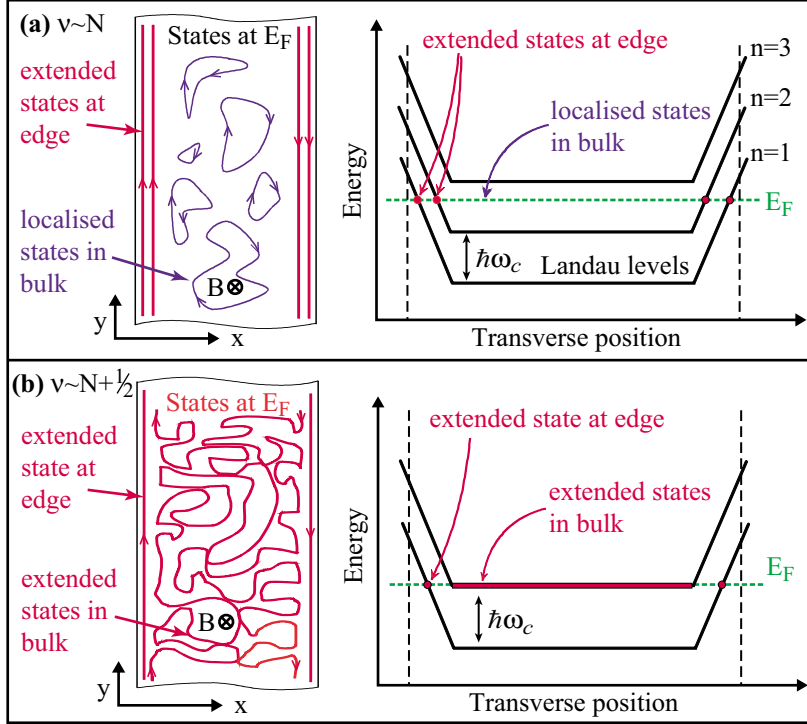


Fig. 3.4: Model of the integer Quantum Hall Effect. **(a)** On the plateaux near integer ν , E_F lies between bulk LLs and the only extended states at E_F are the edge states. Each edge state contributes a conductance of e^2/h , accounting for the quantised R_{xy} . Currents flowing in opposite directions are physically separated by the width of the sample, suppressing backscattering and causing R_{xx} to vanish. **(b)** In the transition regions between plateaux, near half-integer ν , E_F lies on a bulk LL. Extended states exist in the bulk as well as the edges, so R_{xy} is no longer quantised. Current can also backscatter, giving a finite R_{xx} .

ν varies near N , we observe a plateau in R_{xy} as in Fig. 3.1. The situation for the transition regions between plateaux, where $\nu \sim N+1/2$, is pictured in Fig. 3.4(b). Here, E_F lies on a LL, and there are extended states at E_F in the bulk. Backscattering between edges now occurs, making R_{xx} non-zero. The extended states at E_F in the bulk also contribute to the Hall conductivity, but the number of these states decreases as B increases, so that R_{xy} increases with B in the transition regions as seen in Fig. 3.1.

3.3 Edge of the Quantum Hall Conductor

From this discussion it is clear that the edge of the sample plays a central role in electron transport in the quantum Hall regime. For simplicity, we have assumed that the

electrons are non-interacting. A better understanding of the structure of the edge states and their influence on the transport, however, requires that Coulomb interactions be taken into account. Screening effects in the 2DEG turn out to be particularly important, because the screening ability of the 2DEG depends strongly on the filling factor. From Fig. 3.2, we deduce that the 2DEG can effectively screen electric fields only near half-integer ν : near integer ν , there are no extended states at E_F and hence electric fields are unscreened. The spatial variation in ν at the edge (Fig. 3.3) thus leads to spatial variation in the electrostatic screening which must be taken into account self-consistently.

In the absence of interactions, the electron density (and hence filling factor) changes with abrupt steps at the sample edge as shown in Fig. 3.3. These changes in the density occur only at the locations where the bulk LLs cross E_F . When electrostatic repulsion of the electrons is included, however, a smoother change in density is preferred energetically. Screening of the confinement potential by the extended states at the edge broadens the regions where the density changes, resulting in the situation illustrated in Fig. 3.5. The electron density is constant in regions with near-integer ν , where the electrostatic potential is unscreened. Because the density is constant, these regions are known as *incompressible strips*. The incompressible strips have only localised states at E_F and are thus insulating in nature. Between the incompressible strips are regions with changing electron density, where the electrostatic potential is screened and hence constant. These are known as *compressible strips*, and are metallic in character. The compressible strips are the quasi 1D

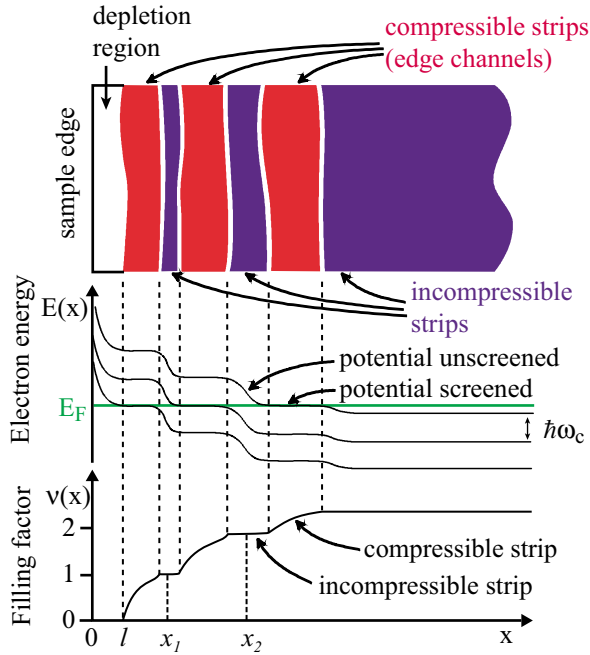


Fig. 3.5: Electrostatic screening by the 2DEG modifies the structure at the sample edge. The edge states broaden into compressible strips where the electrostatic potential is flat (screened) but the electron density changes smoothly. The compressible edge channels have extended states at E_F and are metallic in character. They are separated by incompressible strips where the electron density is fixed at integer ν but the electrostatic potential changes. The incompressible strips have only localised states at E_F and are insulating in character. l is the depletion length at the edge; x_1 and x_2 are the positions the first and second edge states would have if unscreened.

conducting channels responsible for the quantised conductance on the quantum Hall plateaux.

This picture of alternating strips of compressible and incompressible electron fluid (Beenaker 1990, Chang 1990) has been quantitatively elaborated to calculate the positions and widths of the strips under various conditions (Chklovskii 1992, Gelfand 1994, Larkin 1995). The widths of the strips are found to depend on the steepness of the confinement potential gradient at the edge: the steeper the gradient, the narrower the strips. The strips nearer the bulk of the sample are thus wider than those near the edge, and the innermost strips are the widest of all (Chklovskii 1992). The widths of the incompressible and compressible strips predicted by this model are on the order of 100 nm, with the compressible strips always somewhat wider than the incompressible strips.

Experimental results have largely confirmed this model of the edge of a quantum Hall conductor. These measurements have used a variety of techniques, including transport (Kane 1987, Komiyama 1989, van Wees 1989a and 1989b, Alphenaar 1990, McEuen 1990), magnetocapacitance (Takaoka 1994), edge magnetoplasmon excitations (Zhitenev 1994), inductive coupling (Yahel 1996), photovoltage imaging (van Haren 1995, Shashkin 1997), and in situ single-electron transistor (SET) electrometry (Wei 1998). More recently, novel scanned probe methods have been applied to the study of compressible and incompressible strips in the 2DEG, including scanned charge accumulation (Tessmer 1998, Finkelstein 2000) and scanned SET (Yacoby 1999).

One of the experimental consequences of the insulating incompressible strips that separate the conducting edge states (compressible strips) is the existence of non-equilibrium edge state (NES) populations. Using electrostatic gates to manipulate the local electron density, adjacent compressible states can be filled to different levels, creating a non-equilibrium population. Such a non-equilibrium population will persist until equilibrium is re-established by scattering between the edge states. These disequilibrated edge states are especially robust when it is the innermost state that is out of equilibrium with the rest, because the innermost incompressible strip is the widest and can effectively decouple the innermost edge state from the others (Alphenaar 1990, McEuen 1990). The outer edge states often equilibrate rapidly by inter edge state scattering, but non-equilibrium populations in the innermost edge state have been observed to persist over extremely long dis-

tances, up to hundreds of microns, before eventual re-equilibration (van Wees 1989b, Alphenaar 1990).

Previous studies of NES populations and the scattering processes responsible for re-equilibration have all involved transport measurements. These provide much useful information about the sample as a whole, but are not well suited to investigating what is happening at the local scale. Here, we use scanned probe microscopy to study the properties of the edge of the quantum Hall conductor. We create a NES population and measure the local Hall voltage distribution at the sample edge associated with the disequilibrated edge states. We observe sharp voltage drops at the sample edges which are suppressed by removing the NES population. We also observe re-equilibration of the edge state potentials due to inter edge state scattering. Most of these results have been previously published in *Physica E* (Woodside 2000).

3.4 2DEG Sample

The sample used for measurements in the quantum Hall regime is made from a GaAs/AlGaAs heterostructure grown by molecular beam epitaxy. The physical layout of the heterostructure is shown in Fig. 3.6. The 2DEG forms at the interface between the GaAs and undoped AlGaAs layers, due to a band gap mismatch between the two materials (Bastard 1991). The electrons in the 2DEG come from Si dopants in the doped AlGaAs layer, which is physically removed from the GaAs/AlGaAs interface to reduce scattering from the dopants. The heterostructure is capped with a layer of GaAs, so that the 2DEG is

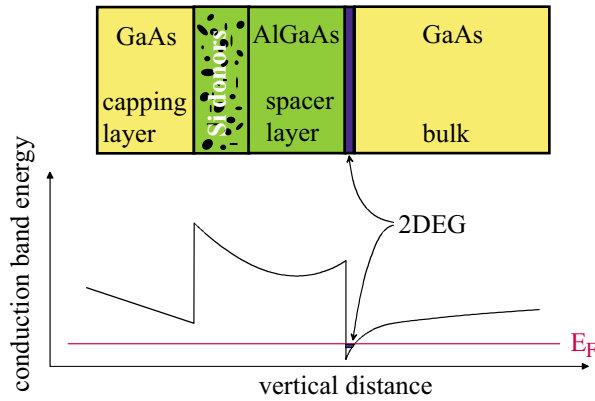


Fig. 3.6: 2DEG in a GaAs/AlGaAs heterostructure. The band gap mismatch between GaAs and AlGaAs creates a quantum well at the interface in which a 2DEG forms. Electrons come from Si donors in a donor layer that is physically removed from the interface to reduce impurity scattering. In the sample used here, the 2DEG lies 90 nm below the surface of the heterostructure.

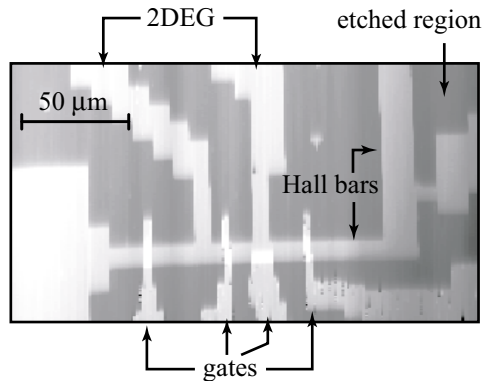


Fig. 3.7: AFM image of a sample used for measurements in chapters 3 and 4. The dark regions show where the 2DEG has been etched away. Transport measurements are made on Hall bars that are 10 and 20 μm wide. Three metallic top gates are used to control the edge state populations (the wide side gate is not used here). The 2DEG density is $2.4 \times 10^{15} \text{ m}^{-2}$ and the mobility at 4K is $19 \text{ m}^2/\text{Vs}$.

90 nm below the surface of the sample. Further details on the heterostructure from which samples are made are described elsewhere (Maranowski 1996).

The heterostructure is patterned using standard photolithographic techniques (Williams 1984) into Hall bars 10 μm and 20 μm wide. The heterostructure is everywhere else etched by a wet chemical process to a depth of 100 nm, completely removing the 2DEG except on the Hall bar. In addition, three 2 μm wide gold gates are deposited on top of the narrow Hall bar by e-beam evaporation. These are used to deplete locally the 2DEG and manipulate the edge state populations. An AFM image of the finished sample is shown in Fig. 3.7. The density of the 2DEG in this sample is $2.4 \times 10^{15} \text{ m}^{-2}$, and the mobility at 4 K

is $19 \text{ m}^2/\text{Vs}$. Note that the mobility is chosen to be high enough to permit non-equilibrium edge states to persist over distances that are long enough to measure, but low enough to permit sufficient scattering in the sample to be able to study equilibration.

3.5 Creating Non-Equilibrium Edge State Populations

The population of the edge states in the sample is manipulated by using the metallic gates on top of the Hall bar (Fig. 3.7) to change the electron density beneath the gates. This allows us to selectively backscatter some of the edge states and establish a non-equilibrium population downstream of the gates, as illustrated in Fig. 3.8 (van Wees 1989a). Note that to maximise the equilibration length, all measurements are taken at a bulk filling factor of $\nu=3$, which is known to support disequilibrated states over long distances (van Wees 1989b, Alphenaar 1990). As shown in Fig. 3.8, all three edge states coming out of the injector contact are at potential V_0 . The injector gate deflects the innermost edge state, so that downstream of the injector gate only the two outer edge states are at potential V_0 ; the inner edge state is at ground, creating a NES population.

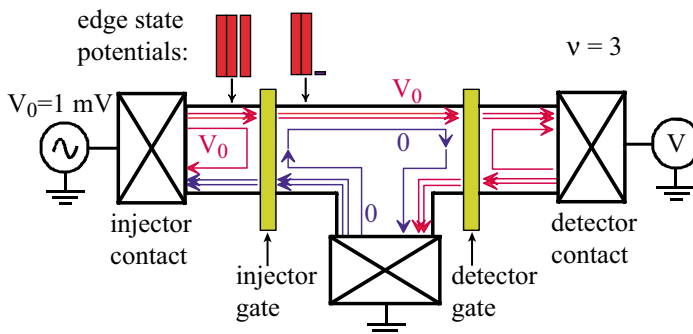


Fig. 3.8: Creating nonequilibrium edge state (NES) populations with gates. The injector gate transmits only the outermost edge states, creating a NES population downstream of the gate: the innermost edge state is at 0 V, while the outer ones are at V_0 .

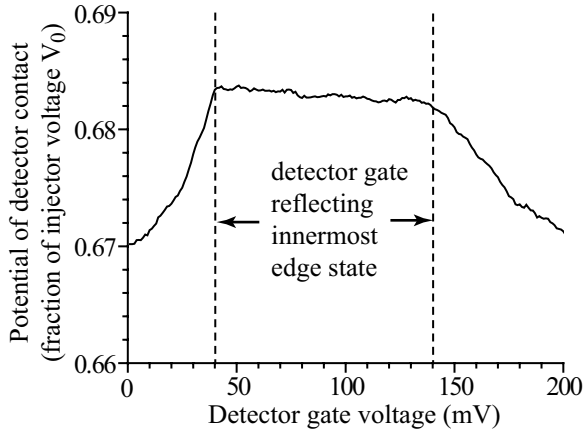


Fig. 3.9: Detecting the NES population. The presence of disequilibrated edge states created as in Fig. 3.8 can be verified by measuring the potential of the detector contact as the detector gate is turned from transmitting the innermost edge state to reflecting it. When there is a NES population, the potential of the outer edge states is higher than that of the inner edge state, causing the detector contact to measure a higher potential when the detector gate only transmits the outer edge states. The small increase in the detector potential seen here indicates that there is significant inter edge state equilibration over the $40\ \mu\text{m}$ distance between injector and detector gates.

We can confirm the presence of a non-equilibrium population by measuring the potential of the detector contact as a function of the detector gate voltage. The detector gate is used to selectively transmit or reflect the inner edge state on its way to the detector contact as shown in Fig. 3.8. If the edge states are disequilibrated, then the potential of the outer two edge states will be higher than that of the innermost state. Since the detector contact measures the average of the potential of the edge states transmitted by the detector gate, the potential of the detector contact will rise if the inner edge state is out of equilibrium with the outer edge states.

When we perform this measurement, shown in Fig. 3.9, we see that the detector contact does indeed measure a higher potential when the detector gate deflects rather than transmits the innermost edge state, confirming the presence of a NES population. In the absence of any mechanisms that re-equilibrate the edge state potentials, the detector potential should change from $(2/3)V_0$ when transmitting the innermost edge state, to V_0 when reflecting it. The fact that the change observed in Fig. 3.9 is significantly smaller indicates

that the edge states are being re-equilibrated during their passage across the 40 μm distance between the injector and detector gates.

The process by which re-equilibration takes place, scattering between edge states, will be investigated in more detail in the next chapter, where we will examine individual scattering sites at the sample edge. Here, we simply parametrise the edge state equilibration by an average equilibration length l_{eq} . If the difference between the edge state potentials changes from $\Delta\mu$ to $\Delta\mu'$ when the edge states travel a distance d , then the equilibration length l_{eq} is defined by:

$$\frac{\Delta\mu}{\Delta\mu'} = \exp\left(-\frac{d}{l_{eq}}\right) \quad (3.1)$$

From Fig. 3.9, we find that the edge states are 95% equilibrated after travelling 40 μm , yielding an equilibration length of $\sim 13 \mu\text{m}$. This is quite short, due to the choice of a low mobility sample, but it permits us to study the equilibration on length scales accessible to scanned probe measurements.

3.6 EFM of Non-Equilibrium Edge States in a Quantum Hall Conductor

We now investigate the properties of non-equilibrium edge state populations by studying the Hall voltage distribution to which they give rise. From previous measurements of the local Hall voltage distribution in a quantum Hall conductor, we know that the edge states have an important influence on the Hall voltage profile (McCormick 1999, Weitz 2000). Sharp voltage gradients at the sample edges are observed when transport measurements indicate the presence of edge states out of equilibrium with the bulk. Here,

we focus more closely on the behaviour at the sample edges by directly controlling the edge state population using electrostatic gates on the sample.

We measure the Hall voltage profile using the ac-EFM technique described in Chapter 2. An ac voltage $V_0 = 1$ mV is applied to one contact of the Hall bar, driving the AFM tip oscillation into resonance via a self-resonant loop. The force on the tip is directly proportional to the local ac voltage in the sample, so that by measuring the amplitude of the tip oscillation we can measure the voltage distribution in the sample. Note that there are significant variations in space of the contact potential of the 2DEG, on the order of 100 mV. Such contact potential variations have been observed previously (Yoo 1997, McCormick 1999), and are most likely due to charges in the surface or dopant layers. To eliminate the effect of these variations, we simultaneously measure a reference signal by applying an uniform voltage at a different frequency to all contacts, as discussed in Chapter 2. Normalising the primary signal by the reference signal, we remove any spatial dependence resulting from contact potential variations and end up with the desired local potential in the sample.

Having confirmed the presence of a non-equilibrium edge state population in the previous section, we measure the local potential profile across the Hall bar by scanning the AFM across the Hall bar, 50 nm above the sample surface and about 5-10 μm downstream of the injector gate. The results are shown in Fig. 3.10 for three different injector gate voltages. When the gate is open, all of the Hall voltage drops in the bulk of the sample with a slightly non-uniform distribution (Fig. 3.10(a)). When the gate backscatters the $\nu=3$ edge state, the potential in the bulk flattens out somewhat and a sharp voltage gradient develops

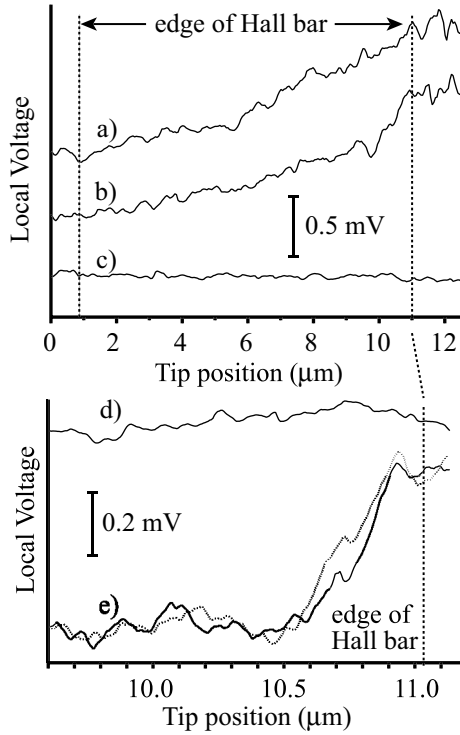


Fig. 3.10: Hall voltage profiles across 10 μm wide Hall bar at $\nu = 3$, taken 5-10 μm downstream of the injector gate. All traces are offset for clarity. **(a)** With the injector gate open, the Hall voltage V_H drops in the bulk of the 2DEG. Voltage gradients in the bulk are due to the non-uniform local conductivity of the states at E_F . **(b)** With the gate at $\nu=2$, reflecting the inner edge state, a sharp voltage gradient develops at one edge of the Hall bar. This is the edge where the NES populations exist. Only half of V_H drops at the edge, due to re-equilibration between the edge states. **(c)** When the gate is pinched off entirely so that no edge states are transmitted, V_H disappears. **(d),(e)** Close up view of the Hall voltage profile at the sample edge. **(d)** When the gate is open, there is no gradient at the edge because there is no NES population. **(e)** With the gate at $\nu=2$, the Hall voltage drops over a distance of ~ 300 nm, 200 nm from the sample edge. Two traces are plotted to show the reproducibility of the signal (small-scale features are noise).

at one edge of the Hall bar, the edge where the backscattered state flows (Fig. 3.10(b)). Approximately half of the Hall voltage drop occurs at this edge; the rest occurs in the bulk. Finally, when the gate is entirely closed off, the Hall voltage profile is flat (Fig. 3.10(c)). The effect of the gate voltage on the Hall voltage profile at the edge of the 2DES can be seen more clearly in an expanded view of the edge (Fig. 3.10(e),(f)). The voltage gradient arising from the back-scattering of the $\nu=3$ edge channel drops over a distance of 0.3 μm , about 0.2 μm from the edge.

These observations can be readily understood in terms of the standard theory of the edge of a quantum Hall conductor presented earlier in this chapter. When the gate is open and all edge states pass through, the edge states are all at the same potential, and there is no

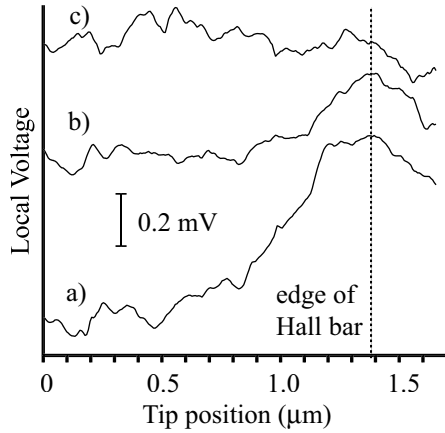


Fig. 3.11: Re-equilibrating NES populations at $\nu=3$ with a dc Hall voltage. All traces are offset for clarity. **(a)** At 0 dc bias, the Hall voltage drop due to the NES population is seen clearly. **(b)** At 5.5 mV dc bias, close to $\hbar\omega_c = 5.5$ meV, the voltage gradient at the edge is greatly diminished, as the edge states are mostly re-equilibrated. **(c)** At 8 mV, there is no gradient left at the edge, and the edge states are fully re-equilibrated.

voltage drop at the edges (Fig. 3.10(d)). Instead, the Hall voltage drops in the bulk of the sample (Fig. 3.10(a)), where the Hall voltage distribution is determined by the local conductivity of the states at E_F (McCormick 1999). When the gate is fully pinched off, all of the edge states are reflected and hence no Hall voltage is observed (Fig 3.10(c)). When the gate reflects only the $\nu=3$ edge state, however, the outer edge states downstream of the gate are at potential V_0 while the innermost state is at potential 0, as in Fig. 3.8. This gives rise to a sharp voltage drop across the incompressible strip separating the $\nu=2$ and $\nu=3$ edge states (Fig. 3.10(e)). The length over which the voltage drops suggests that the incompressible strip is at most ~ 300 nm wide. This result agrees well with other measurements (Wei 1998), but it is close to the resolution limit of the measurement and hence should be viewed as an upper bound on the width of the incompressible strip.

It is known that non-equilibrium edge state populations can be re-equilibrated by applying a dc Hall voltage of the order of the LL energy splitting, $\hbar\omega_c$ (Komiyama 1992). We next show that we can observe this in the local potential profile at the edge of the sam-

ple. The voltage near the sample edge in the presence of a dc Hall voltage is shown in Fig. 3.11. The gate reflects the $\nu = 3$ edge state for all the linetraces here. As the dc bias is increased from 0 (Fig. 3.11(a)) to 5 mV (Fig. 3.11(b)), just below $\hbar\omega_c = 5.5$ meV, the voltage drop due to the disequilibrated edge states is reduced substantially, indicating significant re-equilibration. At 8 mV dc bias, well above $\hbar\omega_c$, there is no voltage drop at the sample edge (Fig. 3.11(c)), and the edge states are completely equilibrated.

Note that in Fig. 3.10(b) only about half of the Hall voltage drops across the incompressible strip. This is because of edge state re-equilibration that occurs between the injector gate where the NES population is created and the location where the Hall voltage profile is measured. As found in section 3.5, the equilibration length l_{eq} is only about 13 μm , due to the low sample mobility. The measurements of Fig. 3.10 are taken 5-10 μm downstream of the injector gate, *i.e.* at a distance of between 0.5-1 l_{eq} from the gate. The fact that only half of the original potential difference between the outer and inner edge states remains after this distance is therefore expected.

We can observe this re-equilibration of the edge state populations more clearly by imaging the Hall voltage profile as the AFM tip moves away from the injector gate. In Fig. 3.12, we measure the Hall voltage profile at distances from about 3 μm downstream of the injector gate to 12 μm downstream. We can clearly see that the potential difference between the disequilibrated edge states falls off as the tip moves further away from the gate. Fitting the change in the Hall voltage drop at the edge of the sample to an exponential decrease according to Eq. 3.1, we find an equilibration length of $l_{eq} \sim 6$ μm .

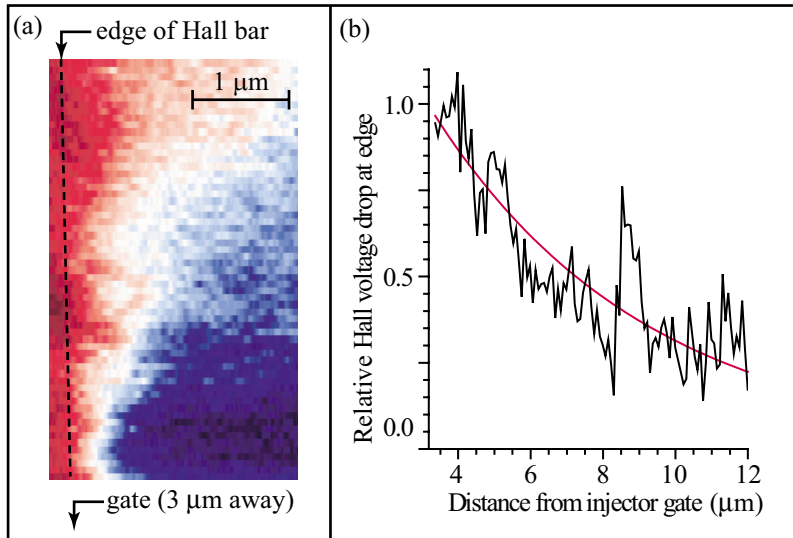


Fig. 3.12: EFM image of edge state re-equilibration at $\nu=3$. **(a)** The Hall voltage profile at the edge of the sample at a distance of 3-12 μm from the injector gate, in the presence of NES populations. A sharp gradient is seen at the edge when the tip is close to the gate. This gradient diminishes as the tip moves away from the gate. **(b)** The relative size of the drop in V_H within 1 μm of the edge as a function of distance from the injector gate. The exponential fit to the decrease in V_H results in an equilibration length of 6 μm .

This is only half as long as the l_{eq} measured by transport (see section 3.5). The reason for the discrepancy is not clear. One possibility is that the model of equilibration in Eq. 3.1 breaks down at these length scales. Eq. 3.1 assumes that the inter edge state scattering that equilibrates the edge state potentials occurs uniformly along the edge. As we shall see in the next chapter, however, the scattering is in fact dominated by discrete scattering centers that are distributed non-uniformly along the edge of the sample (Woodside 2001). The amount of equilibration occurring at each scattering center may vary, so that the equilibration rate is far from uniform along the edge. The average equilibration length l_{eq} expected from Eq. 3.1 thus may not correspond to the local equilibration rate measured with EFM.

3.7 Summary

In conclusion, we have measured the local Hall voltage across a quantum Hall conductor in the presence of gate-induced non-equilibrium edge state populations at $\nu = 3$. We

observe a sharp voltage drop at the edge of the sample along which the disequilibrated edge states flow. This voltage gradient can be suppressed by equilibrating the edge states, either with the gate or with a dc Hall voltage of order $\hbar\omega_c$. Due to the low mobility of the sample, there is significant equilibration of the edge state potentials. We image the local change in the non-equilibrium edge state population with electrostatic force microscopy, finding the local equilibration length. In the next chapter, we will investigate the source of this equilibration by studying individual scattering centers at the edge of the sample.

CHAPTER 4: *Individual Scattering Centers in the Quantum Hall Regime*

4.1 Introduction

The incompressible strips separating the conducting edge states in a quantum Hall conductor can support non-equilibrium edge state populations that persist over extremely long distances before re-equilibrating, sometimes up to hundreds of microns or more (van Wees 1989b, Alphenaar 1990). Measurements of the local Hall voltage distribution at the edge of a quantum Hall conductor in the previous chapter (Woodside 2000) showed that we can observe these non-equilibrium populations locally and watch them as they equilibrate. In the present chapter, we study in more detail the process by which re-equilibration takes place: inter edge state scattering.

Recall that the high magnetic field in the quantum Hall regime physically separates counter-propagating edge states, suppressing backscattering between them. It has a similar effect on the scattering between co-propagating edge states on the same side of the sample that is responsible for edge state equilibration. As discussed previously, edge states belonging to different LLs are separated by incompressible strips. These incompressible strips have a width $a \gg l_B$, where $l_B = \sqrt{\frac{\hbar}{eB}}$ is the magnetic length (Chklovskii 1992). The extent of the edge state wavefunction, however, is only l_B . The tunnelling rate τ between edge states, $\tau \propto \exp\left(-\frac{a^2}{2l_B^2}\right) \ll 1$, is hence very small and tunnelling directly between adjacent edge states is strongly suppressed (Martin 1990). Inter edge state scat-

tering thus occurs principally through scattering from impurity potentials and phonons. Possible sources of these impurity potentials include impurities in any of the heterostructure layers near the 2DEG, especially the donor layer; impurities at the face of the etched sample edge; and impurities in the GaAs/AlGaAs interface. In an effort to quantify the contribution for various sources, several calculations of scattering rates have been performed (Ohtsuki 1989, Badalian 1991, Palacios 1991, Komiyama 1992). One of the important conclusions of this work is that scattering from long range potentials is suppressed due to the large momentum transfer needed to scatter from one LL to the next (Ohtsuki 1989).

Inter edge state scattering has been explored with various transport measurements using electrostatic gates to manipulate the edge state populations. In particular, Komiyama *et al.* (1992) determine from a comparison to their theoretical model that the contribution from acoustic phonon scattering is insignificant at temperatures of about 1 K and below, concluding that equilibration is due only to impurity scattering. Müller *et al.* (1992), Haug *et al.* (1993b), and van Haren *et al.* (1993) show that the equilibration rate can be changed significantly by changing the confinement potential at the edge of the sample using gates. They find that when the confinement potential is made shallower, the equilibration rate decreases because the edge states are pushed further apart and moved further from impurities at the edge of the sample. A few measurements also observe sharp fluctuations in the equilibration as a function of gate voltage and/or magnetic field

(Alphenaar 1991, Acremann 1999). These are interpreted as indirect evidence of scattering from individual scattering centers .

All of these measurements study the aggregate equilibration over distances of 10's of microns, and therefore have difficulty investigating the properties of individual scattering sites. Basic questions remain about the nature of the scattering centers, their frequency, and the amount of scattering at individual sites. Using an atomic force microscope (AFM) tip as a gate to influence inter edge state scattering, we address these issues by imaging and characterising individual scattering centers, to our knowledge for the first time. We find that scattering involves both tunnelling through weak links and scattering from microscopic impurities. These measurements yield a clearer picture of the nature of edge state scattering and also provide lessons about how a scanned probe tip influences a sample. These results were previously published in *Physical Review B Rapid Communications* (Woodside 2001).

4.2 Scanned Gate Microscopy of Inter Edge State Scattering

The sample we study is the same GaAs/AlGaAs heterostructure as in the previous chapter. It has a 2DEG lying 90 nm below the surface, with a density of $2.4 \times 10^{15} \text{ m}^{-2}$ and a mobility of $19 \text{ m}^2/\text{Vs}$. The low mobility ensures that there is enough scattering to allow the study of intrinsic scattering centers. All measurements are made at temperatures between 0.7 and 1 K and at filling factors between $\nu=3$ and $\nu= 2.5$. At these filling factors there are 2 spin resolved outer edge states and a single inner edge/bulk state, as shown in

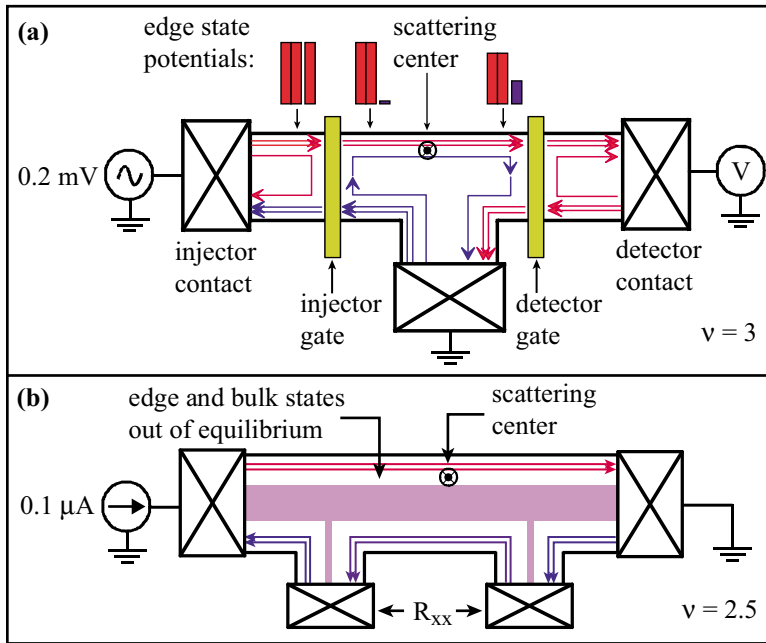


Fig. 4.1: Creating and detecting non-equilibrium edge state (NES) populations. **(a)** At $\nu=3$ the injector gate reflects the innermost edge state, creating a NES population downstream of the gate. Scattering centers near the edge re-equilibrate the edge state potentials, reducing the potential of the outer states. The detector gate reflects the innermost edge state, allowing the detector contact to measure the potential of the outer edge states. **(b)** Bulk and edge states are decoupled near $\nu \sim 2.5$, giving rise naturally to NES populations. The outer edge states carry excess current, depressing R_{xx} in a 4-terminal measurement. Scattering centers between the resistance probes increase the equilibration between bulk and edge, increasing R_{xx} .

Fig. 4.1. As shown in the last chapter, these filling factors allow significant non-equilibrium edge state (NES) populations.

We use two different methods to establish and detect NES populations. The first method (Fig. 4.1(a)) is the same as the one described in section 3.6: a metal gate on top of the 2DEG (the injector gate) is used to selectively inject a non-equilibrium current distribution into the outer edge states. A second gate (the detector gate) is then used to detect the existence of the NES population by selectively transmitting the outer edge states to a voltage probe (van Wees 1989a). The second technique (Fig. 4.1(b)) uses the fact that NES populations arise naturally in the transition regions between quantum Hall plateaux when the edge and bulk states are decoupled (van Wees 1989b, Alphenaar 1990). The non-equilibrium edge states carry excess current that depresses the longitudinal resistance

R_{xx} . Additional equilibration between the bulk and the edges leads to an increase in R_{xx} . Changes in the NES population can thus be detected by measuring R_{xx} .

Having established a NES population by one of these methods, we use scanned gate microscopy (SGM) to study the local scattering in the sample. The AFM tip is metalised with Ti and has a diameter of approximately 100 nm. When the tip is biased with a voltage V_{tip} as described in Chapter 2, it acts as a local gate and perturbs the states at the edge of the 2DEG. This alters the scattering between edge channels, changing the equilibration rate. We scan the tip 50-75 nm above the sample and measure the change in equilibration induced by the tip with one of the methods described above. Note that a large V_{tip} (outside the range ± 1 V) causes abrupt hysteretic changes in the scattering, and sometimes irreversibly increases the scattering rate. This is likely due to a rearrangement of the charges in the donor or surface layers induced by V_{tip} (Tessmer 1998). For this reason, large tip voltages are not used in these measurements.

Fig. 4.2(a) displays the results for a 10 μm long section of the edge of the Hall bar where the NES population is established and detected using top gates. The tip voltage here is $V_{tip} = 0.9$ V¹. Regions where the scattering is enhanced by the presence of the tip are light, whereas regions where it is reduced are dark. Several bright features representing areas of increased scattering are visible along the edge of the sample. They are not correlated with any topographic features, and they are not observed when the edge and

1. The contact potential, the potential at which the tip voltage does not perturb the sample, varies from 0-0.3 V at different locations due to the effects of charges in the surface and donor layers.

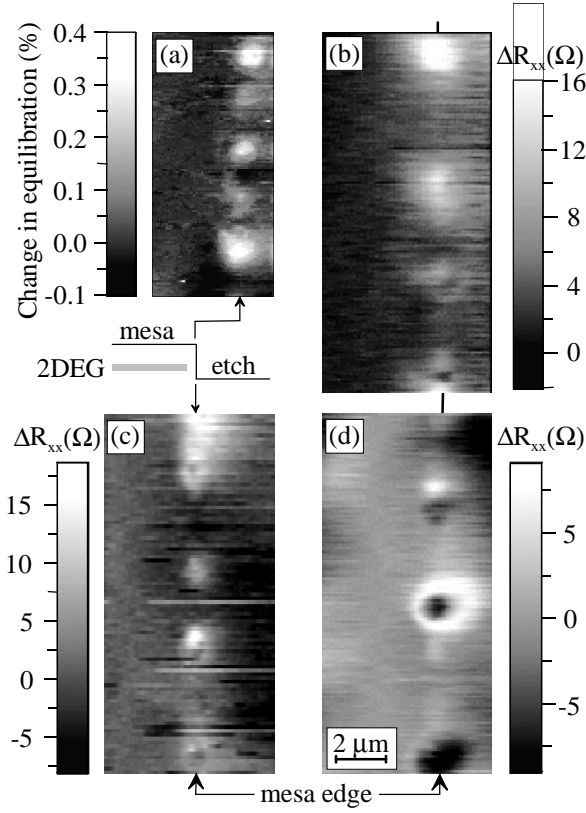


Fig. 4.2: Scanned gate images of scattering centers at the edge of the Hall bar. **(a)** An image of the equilibration along a 10 μm section of the Hall bar at $\nu=3$ using the method of Fig. 4.1(a). The bright regions show where the AFM tip increases inter edge state scattering. This image is taken with $V_{tip}=0.9$ V and an injector bias of 0.2 mV rms. **(b)-(d)** Images of the equilibration-induced change in longitudinal resistance R_{xx} along three different 15 μm sections of the Hall bar at $\nu=2.6-2.7$, using the method of Fig. 4.1(b). Several different types of features are observed: bright spots of increased scattering, dark spots of decreased scattering, and bright rings of increased scattering surrounding regions of decreased scattering. These images are taken with $V_{tip}=0.8$ V and a current bias of 100 nA rms

bulk are in equilibrium. They are clearly associated with individual scattering centers, separated on average by ~ 2 μm .

Similar results are seen when the NES population is established by selective back-scattering of the bulk state, as in Fig. 4.1(b). Since these measurements do not have to be made between the gates, larger areas can be explored. Figs. 4.2(b)-(d) show the scattering-induced change in R_{xx} over three different 15 μm long segments of the sample edge at filling factor $\nu \sim 2.6-2.7$. In addition to bright spots of increased scattering, there are dark spots of decreased scattering, and bright rings of increased scattering surrounding regions of decreased scattering. Again, these are observed only along the edge of the sample and

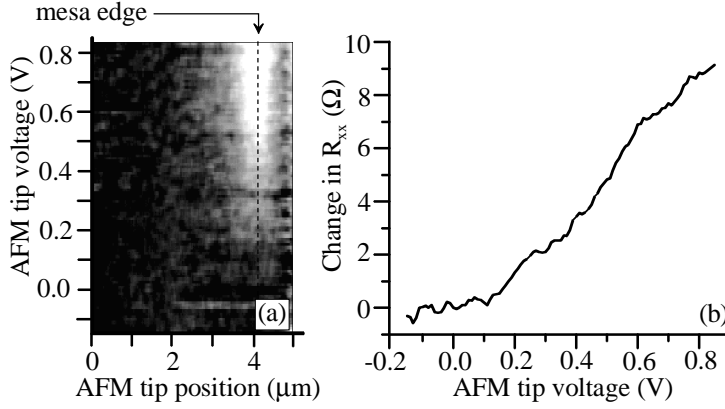


Fig. 4.3: Tip voltage dependence of the scattering at one of the bright spots of increased scattering in Fig. 4.2. **(a)** Cross section through the center of the bright spot as a function of V_{tip} . The center of the scattering feature is located at the edge of the Hall bar mesa. The scattering increases monotonically with V_{tip} , but the width at half maximum remains constant. **(b)** Linetrace at the center of the spot showing the increase in R_{xx} due to the scattering.

are separated on average by a distance of $\sim 2 \mu\text{m}$. We find that the bright spots occur most frequently, while the dark spots and the bright rings each occur only about one third as frequently. On average, then, a positive AFM tip bias increases inter edge state scattering, but at any particular site it can either enhance or reduce the scattering.

The nature of these scattering centers can be probed further by examining the tip voltage dependence of the scattering. A cross-section through the center of one of the bright spots as a function of V_{tip} is shown in Fig. 4.3(a). As V_{tip} is reduced from positive values, the amount of scattering at the center of the spot decreases monotonically until the spot disappears (Fig. 4.3(b)). The width at half-maximum of the spot remains roughly constant as V_{tip} is changed. In some cases, a dark spot appears at negative V_{tip} , indicating reduced scattering.

Figs. 4 and 5 show the tip voltage dependence of one of the rings of scattering. A cross-section through the ring as a function of V_{tip} (Fig. 4.4(a)) reveals strikingly different behaviour from that seen in Fig. 4.3. There is a strong peak in the amount of scattering at

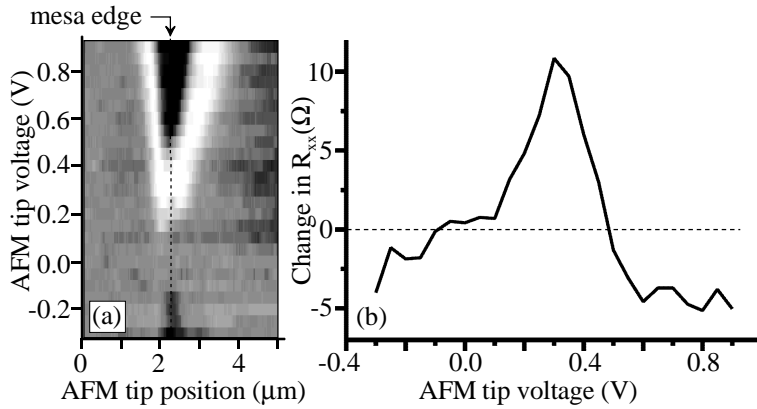


Fig. 4.4: (a) Cross section through the center of a ring of increased equilibration as a function of V_{tip} . The equilibration is increased around the rim of the ring but decreased in the center. As V_{tip} is reduced from large positive values, the radius of the ring shrinks until the ring disappears near 0 V. A spot of reduced scattering appears in its place at negative V_{tip} . (b) A linetrace at the center of the ring shows a peak in the equilibration.

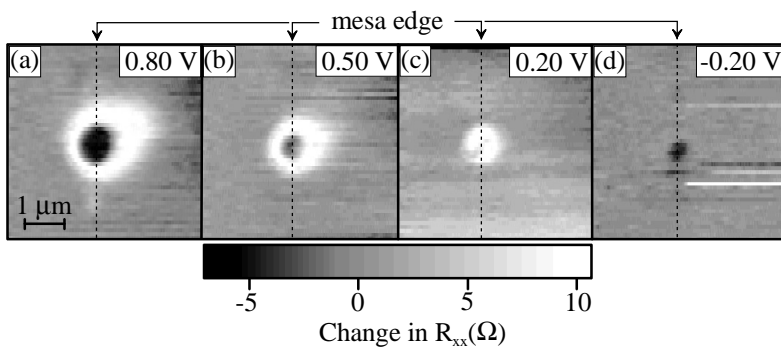


Fig. 4.5: Images of the scanned gate feature in Fig. 4.4 at different tip voltages. As V_{tip} decreases from positive values, the ring of increased scattering (a) first shrinks (b), then collapses to a spot of increased scattering (c). At negative V_{tip} , it turns into a spot of decreased scattering (d).

the center of the ring as V_{tip} is changed, as seen in Fig. 4.4(b). The evolution of the scattering with V_{tip} revealed by Fig. 4.4(a) is more clearly illustrated in Fig. 4.5 by a series of images of the same scattering feature at different tip voltages. As V_{tip} is reduced from positive values, the radius of the ring shrinks linearly with V_{tip} until the ring collapses into a spot. The magnitude of the scattering peak remains constant during this process. As V_{tip} is reduced further, the spot of increased scattering first vanishes and then is replaced by a spot of decreased scattering at negative V_{tip} .

4.3 Interpretation

To understand these results, we consider how an electrostatic perturbation at the sample edge influences edge state scattering. Equilibration involves tunnelling across the $\nu=2$ incompressible strip between edge and bulk states. As described earlier, the tunnelling rate is proportional to $\exp(-a^2/l_B^2)$, where a is the width of the strip and l_B is the magnetic length. Because $a \ll l_B$, tunnelling is normally strongly suppressed (Martin 1990). Previous work has shown that the scattering rate can be changed by using a gate alongside the 2DEG to change the confining potential and alter the width of the incompressible strip, as discussed in section 4.1. Positive side gate bias decreases the width of the strip, increasing the equilibration rate, while negative bias has the opposite effect. In these measurements, the AFM tip plays a role analogous to the side gate by changing the confining potential at the sample edge. This both moves the edge states and alters the width of the incompressible strip.

We interpret the bright spots of increased scattering seen in Fig. 4.3 as weak links in the incompressible strip. It is known that potential variations at the edge of the 2DEG cause the width of the strip to fluctuate along the length of the sample (Chklovskii 1992, van Haren 1993, Haug 1993a). Locations where the strip is especially narrow give rise to weak links across which tunnelling occurs preferentially, as illustrated in Fig. 4.6(a). Positive V_{tip} hardens the confining potential and further decreases the width of the strip, increasing the tunnelling through the weak link (Fig. 4.6(b)). These results are thus consistent with previous work showing an increase in equilibration rates with more positive

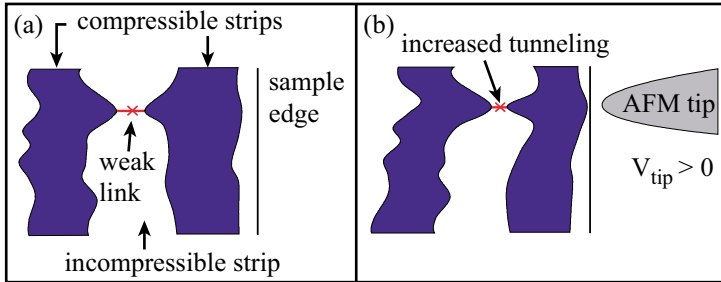


Fig. 4.6: Scattering through weak links (bright spots in Fig. 4.3). **(a)** Variations in the width of the incompressible strip create narrow regions (weak links) through which tunnelling occurs preferentially. **(b)** Positive V_{tip} increases the confinement potential gradient, decreasing the width of the weak link and increasing the tunnelling between edge states. V_{tip} also moves the edge states closer to the edge.

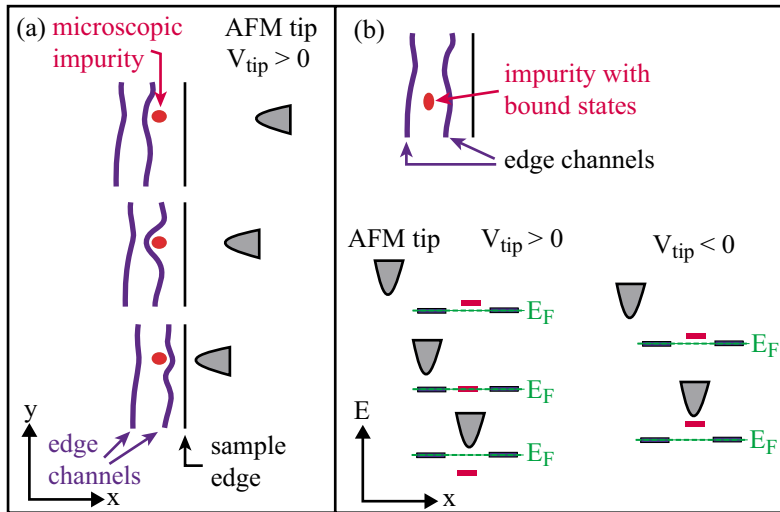


Fig. 4.7: Scattering from microscopic impurity (bright rings in Figs. 4.4 and 4.5). **(a)** The AFM tip voltage causes the edge states to move. Peaks in the scattering occur when the AFM tip pushes the edge states over the potential gradients associated with a microscopic impurity. **(b)** If an impurity lying between the edge channels supports bound states, then peaks in the scattering will occur when V_{tip} brings the energy level of the impurity state into resonance with E_F .

side gate bias. The high spatial resolution of the AFM tip, however, reveals that the increased scattering occurs only at specific sites along the edge.

The different behaviour seen in Fig. 4.4 indicates a different type of scattering center. We interpret the bright rings as scattering from potential fluctuations with a size scale smaller than the edge state structure. Such microscopic impurities may arise from an individual defect or dopant atom near the heterostructure interface. The tip can change the scattering from these impurities in two ways, as shown in Fig. 4.7. First (Fig. 4.7(a)), the tip moves the edge states around the impurity. When the tip pushes the edge states across

an impurity, the large potential gradients associated with the impurity narrow the incompressible strip and increase the tunnelling between edge states, causing a peak in the scattering. Second (Fig. 4.7(b)), if the impurity supports bound states, then the tip will also change the energy of the impurity states. Scattering peaks can then occur when V_{tip} brings the impurity states into resonance with the Fermi level (Jain 1988, Main 1994, Cobden 1999), as long as the impurity remains between the edge states. If more than one electron can occupy the site, single-electron charging may produce multiple concentric rings around the scattering site.

We have studied 7 annular scattering features, and most have a single ring as in Figs. 4.2 and 4.5. This is consistent with both of the mechanisms described above. Only one showed evidence of multiple rings, a faint double ring shown in Fig. 4.8. The fact that more multiple rings are not seen may be due to the limited range of V_{tip} that

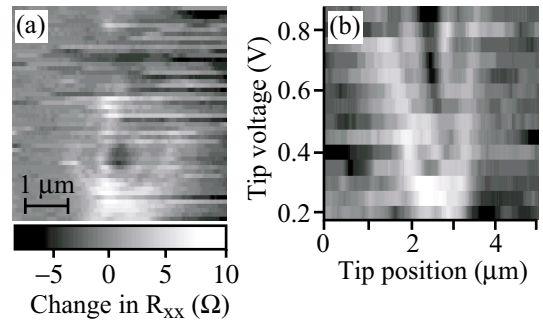


Fig. 4.8: Double ring feature in the scattering. **(a)** A faint double ring of increased scattering is seen next to a bright spot of increased scattering. **(b)** A cross section through the middle of this feature as a function of V_{tip} shows that both rings contract at the same rate as V_{tip} is reduced.

can be used without rearranging charges in the donor layer or on the surface. Further study of the dependence of the scattering on temperature, bias, and magnetic field will be required to clarify the relative importance of these mechanisms².

2. Impurities located on opposite sides of the incompressible strip should cause scattering similar to Fig. 4.5 but at opposite V_{tip} polarity (this is also true for bound states having energies on opposite sides of the Fermi level). We believe this is the origin of the dark spots of reduced scattering at positive V_{tip} in Fig. 4.2. It also explains why such dark spots occur with the same frequency as the rings of increased scattering.

We now turn to the question of how much equilibration occurs at each site. This can be determined from the results of Fig. 4.2(a), where top gates are used to measure the non-equilibrium potential difference $\Delta\mu$ between the $\nu=1, 2$ and $\nu=3$ edge states. In the absence of the tip, the total equilibration rate over the $30\ \mu\text{m}$ distance between top gates is $\sim 90\%$. Since scattering sites are located every $\sim 2\ \mu\text{m}$, the average scattering probability p needed to account for the measured equilibration rate (Acremann 1999) is $p \sim 0.15$. The NES population is therefore reduced by $\sim 15\%$ at each microscopic scattering site.

We can also determine from Fig. 4.2(a) the amount of extra scattering caused at each scattering site by the AFM tip perturbation. The change in the scattering probability Δp induced at a particular site is given by the fractional change in $\Delta\mu$ caused by the tip at that site. For the scattering sites observed in Fig. 4.2(a) with $V_{tip} = 0.9\ \text{V}$, we find that $\Delta p = 0.1-0.3$, with an average value of $\Delta p = 0.2$. The amount of scattering induced by the tip at this tip bias is thus of the same order as the scattering already present in the sample.

These experiments are, to our knowledge, the first direct measurement of the amount of edge state coupling at individual scattering sites. They show that the equilibration is dominated by strong scattering centers separated by a few μm . This contrasts with the results of a previous study, which inferred the existence of scattering sites with $p \sim 0.006-0.02$ separated by $\sim 90-600\ \text{nm}$ based on a statistical analysis of scattering between the $\nu=2$ and $\nu=1$ (spin-polarized) edge states (Acremann 1999). The origin of the differences between these two experiments is not clear. However, the momentum and spin conservation issues for scattering between edge states of different orbital LLs are very

different from those for scattering between different spin states within the same LL (Haug 1993a).

The measurements presented here clearly probe individual scattering centers. We emphasize, however, that the relation between the observed features and the underlying scattering centers is not straightforward, due to the complex tip-sample electrostatics. As discussed above, the rings seen in Fig. 4.5 correspond not to annular scattering centers, but rather to equipotential contours around a single scattering center. The ring of scattering in Fig. 4.5 is also not circular, as might naively be expected, but flattened on the side over the mesa. This is due to the spatial variation in the dielectric properties of the sample near the mesa edge. The high-dielectric GaAs ($\epsilon \sim 13$) and the 2DEG screen the AFM tip more effectively when the tip is over the mesa than when it is over the etched region, flattening the side of the ring over the mesa. We note as well that the scanned gate features in Figs. 4.2-4.5 are very near the physical edge of the sample. Previous theoretical (Chklovskii 1992, Larkin 1995) and experimental work (Wei 1998), however, indicates that the edge states reside several hundred nm inside the mesa due to depletion of the 2DEG near the sample edge. We again attribute this to the non-uniform screening properties near the sample edge: the tip has its greatest effect near the edge of the mesa where the 2DEG and the GaAs are less effective in screening it. This further illustrates the complexities in relating features observed in scanned probe images to the underlying spatial structures in the 2DEG.

4.4 Summary

In this chapter, we have investigated the scattering between edge states in a quantum Hall conductor, studying the mechanisms responsible for re-equilibrating non-equilibrium edge state populations. We have seen that the scattering occurs at discrete sites along the edge, and we have for the first time imaged and characterised these individual inter edge state scattering centers. By studying the dependence of the scattering on tip voltage, we have found that the scattering involves tunnelling across weak links and scattering from microscopic impurities.

This concludes our study of the electronic properties of 2DEGs in the quantum Hall regime. In the coming chapters, we turn from looking at electrons in 2D to looking at electrons in 1D, exploring the properties of carbon nanotubes in the single-electron regime.

5.1 Introduction

In the previous chapters, we used a low-temperature AFM to investigate the local electronic properties of 2D electron gases in the quantum Hall regime. We found that we could study in detail microscopic aspects of the transport such as the Hall voltage distribution, non-equilibrium edge state populations, and individual scattering centers at the sample edges. We now move from systems where electron motion is confined to two dimensions systems to a system where electrons are confined to only one dimension: specifically, carbon nanotubes.

Carbon nanotubes are cylinders of covalently bonded carbon atoms that were first discovered in 1991 (Iijima 1991). They have since been the subject of very intense scrutiny (for a review, see Dresselhaus 1996 and Ebbesen 1997). Partly this is due to the beautiful model system nanotubes provide for 1D physics. Mainly, however, the interest in nanotubes has been inspired by the many promising applications that have been identified in areas as diverse as materials design (Dresselhaus 1996), electronics (Dekker 1999), nano-electromechanical systems (Kim 1999) and sensor technologies (Collins 2000, Kong 2000). Here we will concentrate on the electrical properties of carbon nanotubes, studying in particular electron transport through individual single-walled carbon nanotubes.

Note that carbon nanotubes actually exist in two principal forms: *single-walled* nanotubes and *multi-walled* nanotubes. Single-walled nanotubes consist of a single isolated cylinder of carbon, while multi-walled nanotubes consist of sets of multiple, nested cylinders (Dresselhaus 1996). Each form is interesting in its own right and has been the subject of much study. For simplicity, however, we ignore multi-walled nanotubes in this work and confine our investigations to individual single-walled nanotubes.

This chapter will present a brief overview of the electronic properties of carbon nanotubes. In section 5.2, we describe the band structure of carbon nanotubes and how it affects their basic electronic properties. Previous electron transport measurements will be discussed in section 5.3. Finally, section 5.4 will review what has been learned from previous scanned probe measurements of the electronic properties of nanotubes. This will set the stage for an account of new work on scanned gate microscopy in the single-electron regime in Ch. 6 and single electron force microscopy in Ch. 7.

5.2 Band Structure of Carbon Nanotubes

Carbon nanotubes, the most recently discovered form of elemental carbon, are cylindrical macromolecules of carbon that form under special conditions. They typically have a diameter on the order of a few nanometers, and a length of up to many microns. Their structure is very similar to graphene (a single sheet of graphite). In fact, we can image a nanotube as just a piece of a graphene sheet that has been rolled up along its axis

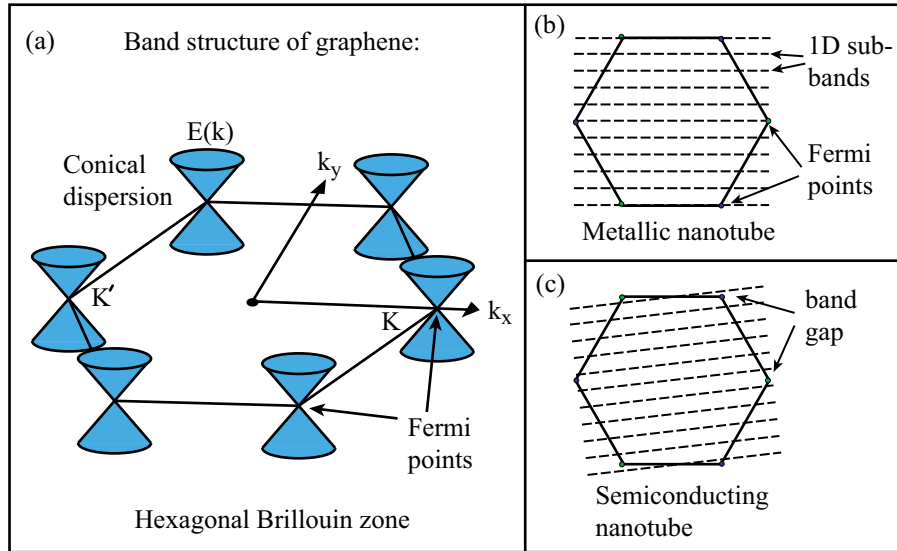


Fig. 5.1: Band structure of carbon nanotubes. **(a)** Band structure of graphene, the parent material of carbon nanotubes. The first Brillouin zone is hexagonal, and the Fermi surface consists of the K, K' points at the zone boundary. The dispersion at each point is conical. **(b)** Periodic boundary conditions create 1D subbands in the transverse axis. When the subbands cross the Fermi points, the nanotube is metallic. **(c)** When the chirality of the nanotube is such that the subbands do not cross the Fermi points, the nanotube is semiconducting.

and then stitched together along the seam. The C atoms in the nanotubes are bonded by sp^2 -hybridised orbitals just as in graphene, and the band structure is hence essentially the same as that of graphene (Saito 1992).

Graphene is a semimetal whose band structure is illustrated in Fig. 5.1(a). The Fermi surface of undoped graphene consists of only 2 inequivalent points at the Brillouin zone boundary (the K and K' points), with conical band dispersion dispersion around each of these points as shown. In carbon nanotubes, this picture is modified principally by the imposition of periodic boundary conditions due to the cylindrical symmetry of the nanotubes. These periodic boundary conditions give rise to 1D subbands perpendicular to the longitudinal axis of the nanotube (Hamada 1992). The orientation of the axis of the nano-

tube relative to the graphene lattice structure (known as the chirality of the nanotube) determines how these 1D subbands intersect the 2D conical band surfaces at the Brillouin zone boundary. This in turn determines the electrical properties of the nanotube. If the subbands cross the Fermi points at the zone boundary, then the nanotube is a 1D metallic conductor with linear subband dispersion, as shown in Fig. 5.1(b). Because there are only two inequivalent Fermi points, the nanotube has only two 1D conducting channels. If the subbands do not cross the Fermi points, then there is a bandgap at the Fermi energy and the nanotube is a 1D semiconductor as shown in Fig. 5.1(c).

The electronic properties predicted from the band structure have been confirmed directly by experiment. For example, scanning tunnelling microscopy (STM) has been used to image the lattice of individual nanotubes with atomic resolution and measure density of states spectra (Odom 1998, Wildöer 1998). Fig. 5.2 shows STM images of two nanotubes, one semiconducting (Fig. 5.2(a)) and one metallic (Fig. 5.2(b)). The atomic lattice can be clearly seen, allowing the chirality of the nanotubes to be determined. The density of states spectra from the nanotube expected to be semiconducting because of its chirality do indeed show a bandgap at the Fermi energy (Fig. 5.2(c)). The spectra from the nanotube that is expected to be metallic, on the other hand, show that there is no gap (Fig. 5.2(d)). These measurements also provide clear evidence of the 1D nature of conduction: the edges of the subbands reveal the van Hove singularities that are expected for 1D conductors (Kittel 1986). In other experiments, STM has been used to image directly the spa-

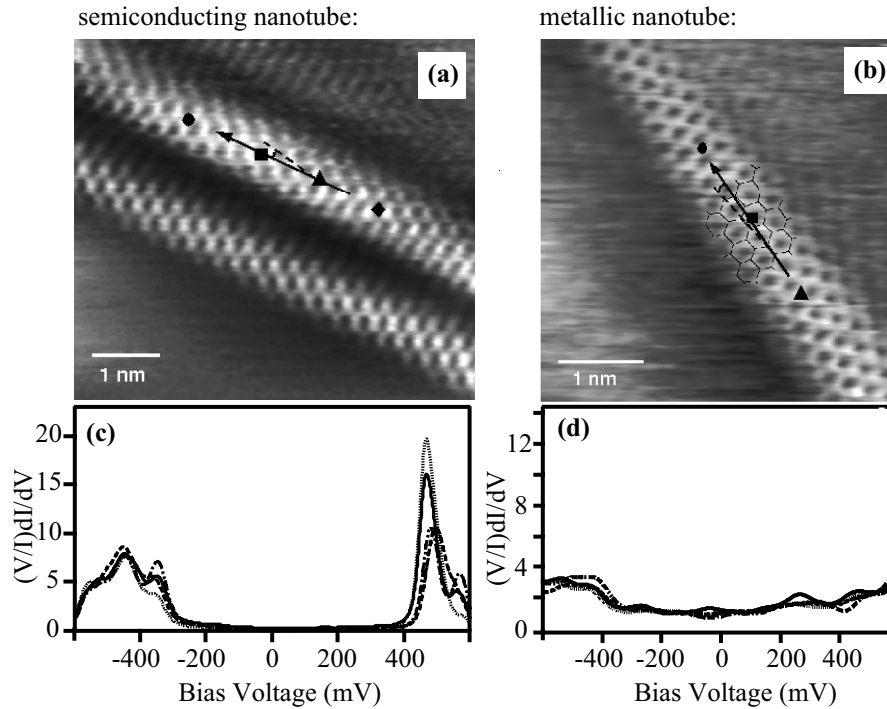


Fig. 5.2: STM images of single-walled nanotubes. **(a)** Semiconducting nanotube. The atomic lattice is clearly visible. **(b)** Metallic nanotube. **(c)** Electronic density of states (DOS) spectra at several points on the nanotube in (a). There is a energy gap at the Fermi level. **(d)** Electronic DOS spectra from the nanotube in (b). There is no gap at the Fermi level. Images and spectra from Odom *et al.* (1998), courtesy of P. Kim.

tial structure of electronic wavefunctions in a carbon nanotube, again confirming the picture of Fig. 5.1 (LeMay 2001).

5.3 Transport Measurements of Nanotubes

Simple electron transport measurements through gated nanotubes at room temperature are consistent with the picture described above. The two types of transport behaviour that are expected for metallic and semiconducting nanotubes are indeed observed. In semiconducting nanotubes, there is a gap in the density of states. A voltage applied to the

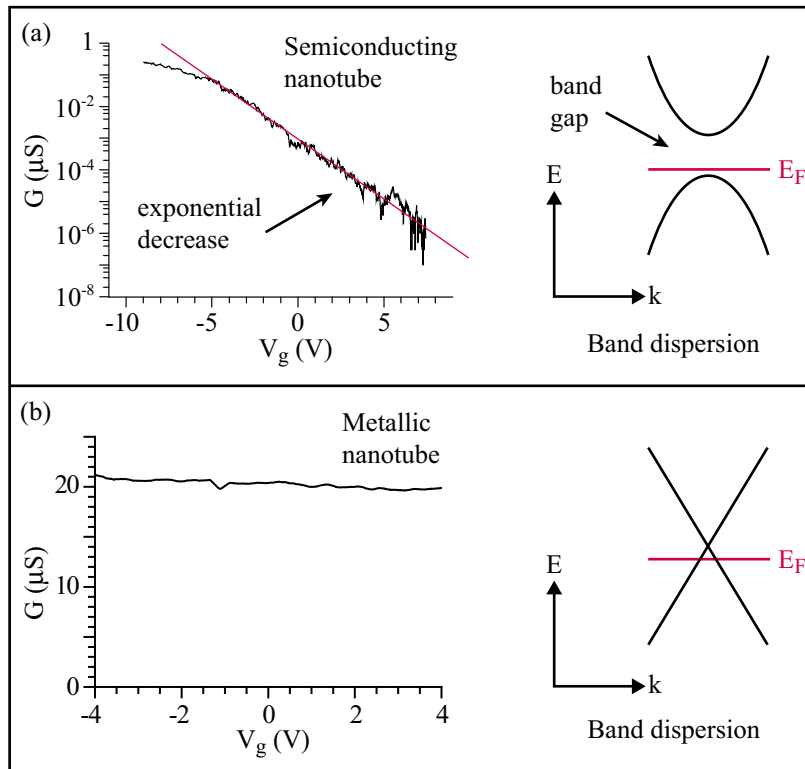


Fig. 5.3: Room-temperature transport measurements of nanotubes. **(a)** Semiconducting nanotube. The conductance decreases by many orders of magnitude as increasingly positive gate voltage moves the Fermi level into the bandgap. The nanotube is p-doped by the contacts and/or substrate. **(b)** Metallic nanotube. The conductance varies little with gate voltage, since there is no energy gap at the Fermi level. Figures courtesy of M. Bockrath.

gate can be used to move the Fermi level E_F of the nanotube, depleting the carrier concentration as E_F moves into the gap and causing an exponential decrease in the conductance (just as in semiconductor field-effect transistors). This behaviour is shown in Fig. 5.3(a). In metallic nanotubes, on the other hand, there is no energy gap, and hence the conductance is not very sensitive to the gate voltage. This behaviour is shown in Fig. 5.3(b). The gate voltage dependence of the conductance can thus be used as a simple test to determine whether a nanotube is metallic or semiconducting. Note from Fig. 5.3(a) that the nanotube is p-doped by the gold contacts and/or the substrate due to differences between the work-function of these materials. This is generally observed to be the case in nanotube devices¹.

1. Similar p-doping of nanotubes by gold is observed in STM measurements of nanotubes (*e.g.* Wildöer 1998).

When the two-terminal conductance of carbon nanotubes is measured, it is found to vary significantly from one device to the next, by many orders of magnitude (McEuen 1999). This is attributed to two reasons. First, as mentioned, the conductance depends strongly on whether the nanotube is metallic or semiconducting. Second, there are often difficulties in making proper Ohmic contact to the nanotube, so that electrical contact frequently occurs through tunnel barriers between the electrodes and the nanotube. When good contact is made to a nanotube, the conductance can approach the value $G = 4e^2/h$ ($R \sim 6 \text{ k}\Omega$). This is true for both metallic nanotubes (Bockrath 1997) and semiconducting nanotubes that are heavily doped (Park 2001). Note that this conductance is the value expected for ballistic conduction in a 1D wire with 2 spin-degenerate channels (see Eq. 1.2), which is precisely the situation expected from the discussion in the last section.

New behaviour is observed in the gate voltage dependence of the conductance when nanotubes are cooled down to low temperatures. Quasi-periodic peaks appear in the conductance, between which the conductance becomes vanishingly small, as shown in Fig. 5.4 (Bockrath 1997, Tans 1997). This is the classic signature of single-electron charging in a quantum dot, as described in Chapter 1, indicating that 0D quantum dots form within the 1D nanotube due to the presence of tunnel barriers. In some nanotubes a single quantum dot is found to span the entire length of the nanotube, up to several microns, showing that the only tunnel barriers are at the contacts (Fig.5.4(a)). This occurs in both metallic (Bockrath 1997, Tans 1997) and semiconducting (Park 2001) nanotubes. In other nanotubes, multiple quantum dots in series are seen, indicating the presence of multiple

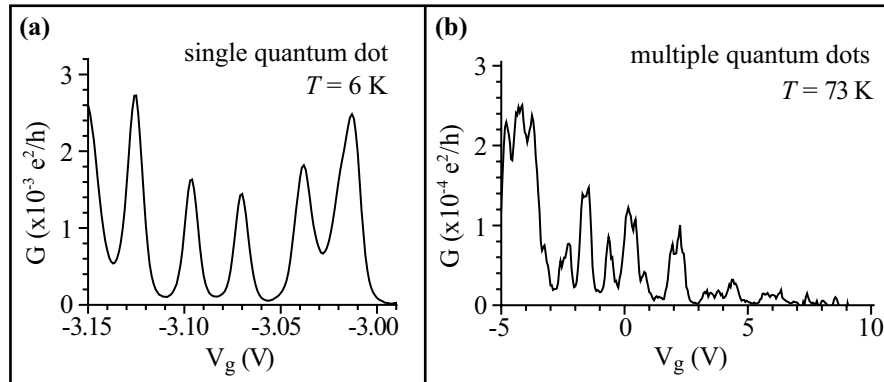


Fig. 5.4: Low-temperature transport measurements of nanotubes. (a) A single ~ 1 μm long quantum dot forms in the nanotube over its entire length, due to tunnel barriers at the contacts. (b) Multiple quantum dots form in the nanotube, producing Coulomb oscillations with many periods. Figures courtesy of J. Park and M. Bockrath.

tunnel barriers within the nanotube (Fig. 5.4(b)). Again, this occurs in both metallic (Bockrath 2001) and semiconducting (McEuen 1999) nanotubes, but it is especially common in semiconducting nanotubes near turn-on.

The transport measurements described above reveal important information about scattering in nanotubes. The microns-long quantum dots and the conductance on the order of the conductance quantum indicate that the mean free path in nanotubes can be many microns in length, with conduction essentially ballistic over the length of the nanotube. This is attributed to several causes. Structural defects are thought to be rare, and scattering from short range disorder is suppressed by the non-zero diameter of the nanotube, which results in the effective short range disorder being averaged over the circumference of the nanotube (White 1998). In metallic nanotubes, scattering from long range disorder is also suppressed by conservation of momentum (McEuen 1999). Semiconducting nanotubes are more sensitive to long range disorder due to less stringent constraints from conserva-

tion of momentum, accounting for the fact that near turn-on they have much shorter mean free paths and more numerous tunnel barriers.

5.4 Scanned Probe Measurements of Nanotubes

As we have seen in the brief review above, transport measurements have revealed many important details about conduction in nanotubes. Nevertheless, traditional transport measurements suffer from the same disadvantage found when studying 2DEGs in the quantum Hall regime: they have very little spatial discrimination, and are thus not ideal for exploring the microscopic properties underlying the behaviour that is observed. This is particularly true when studying defects and scattering centers. Just as with the Quantum Hall Effect, various scanned probe techniques have been applied to study the electronic properties of nanotubes on a local scale. These scanned probe measurements have confirmed and extended the picture of conduction in nanotubes presented above.

For instance, electrostatic force microscopy (EFM) has been used to measure the voltage distribution along individual nanotubes (Bachtold 2000). This allows us to determine where the voltage drops in the nanotube. Such measurements show that there is very little voltage drop across metallic single-walled nanotubes, as expected for a ballistic conductor; instead, the voltage drops at the contacts (Fig. 5.5(a)). The two-terminal resistance is thus dominated by the contact resistance, which can be measured for each contact. Tunnel barriers within the nanotube that give rise to scattering centers causing large voltage

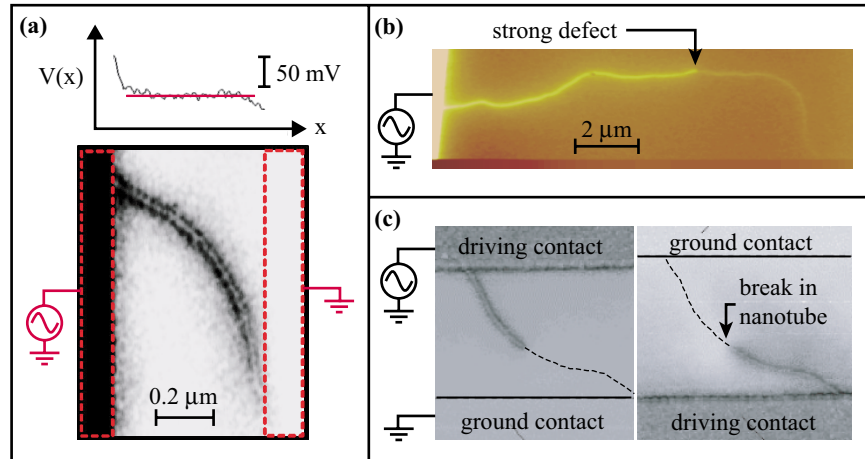


Fig. 5.5: EFM measurements of nanotubes at room temperature. (a) The local voltage distribution in a metallic nanotube shows that conduction is ballistic. Most of the voltage drops at the contacts, whose resistance can be measured. (b) EFM image of a semiconducting nanotube showing a sharp voltage drop across a defect in the middle of the nanotube. (c) EFM images of a broken nanotube. The nanotube can be clearly seen in the EFM images, even though there is no conductance through it. The location of the break can easily be identified. Images courtesy of A. Bachtold and M. Fuhrer (adapted from Bachtold *et al.* (2000) and unpublished).

drops can also be identified. An example is shown in Fig 5.5(b), where a strong defect in the middle of a semiconducting nanotube can clearly be seen. Finally, in contrast to traditional transport measurements, with EFM even broken nanotubes through which there is no conduction can be inspected. This allows, for example, the location of the break to be determined (Fig. 5.5(c)) (Bachtold 2000).

Scanned gate microscopy (SGM) is also useful for probing transport in nanotubes. It has been used to locate the potential modulations that give rise to tunnel barriers in semiconducting nanotubes and hence identify individual scattering centers (Bachtold 2000, Tans 2000, Tomblor 2000b). An example of a scanned gate image of a semiconducting tube is shown in Fig. 5.6. The tunnel barriers are visible here as bright spots

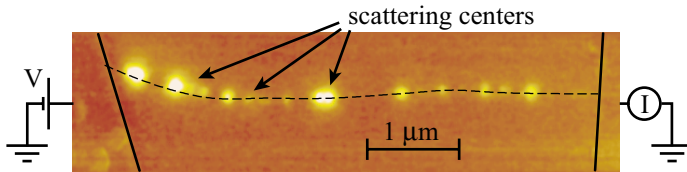


Fig. 5.6: Scanned gate image of a semi-conducting nanotube at room temperature. Many locations where the conductance is very sensitive to the AFM tip voltage can be seen along the length of the nanotube. Adapted from McEuen (2000).

demarking regions of the nanotube that are easily depleted. Individual scattering centers have also been observed with SGM in metallic nanotubes. Here, resonant scattering from microscopic defects was discovered, and the transmission coefficients of the defects were measured (Bockrath 2001).

These scanned probe studies have allowed us to look at what is happening inside nanotubes with high spatial resolution, providing valuable insight into their microscopic properties. Most of these measurements, however, have been carried out on samples at room temperature. This makes them easier to perform, but the high thermal energy (~ 25 meV) limits the energy resolution of the measurements. In particular, the thermal energy is much too high to detect single-electron charging. In the following chapters, we present scanned probe measurements of nanotubes that overcome this limitation by using our low-temperature AFM. This provides us with both high spatial resolution and high energy sensitivity, allowing us to investigate the local properties of nanotubes in the single-electron regime.

CHAPTER 6: *Single-Electron Scanned Gate
Microscopy of Carbon Nanotubes*

6.1 Introduction

We begin our scanned probe studies of the electronic properties of carbon nanotubes with scanned gate measurements in the single-electron regime. In Chapter 4, we used scanned gate microscopy (SGM) to study the scattering between 1D conducting channels at the edge of a quantum Hall conductor. The principal effect of the AFM tip in that case was to change the scattering by altering the tunnel barriers coupling the channels. Now, we use SGM to investigate transport within a single metallic nanotube. Similar measurements have been made before (Bachtold 2000, Bockrath 2001), as mentioned in the previous chapter. The novel element we add here is to perform the measurement at temperatures in the single-electron regime, where the techniques and results of single-electron transport spectroscopy can be brought to bear. As we shall see, the effect of the AFM tip is here not so much to change the tunnel barriers as it is to change the charge states of the 0D quantum dots that form within the nanotube. These are, to our knowledge, the first scanned gate images of quantum dots in the single-electron regime.

The nanotube device used in these measurements is described in section 6.2. Section 6.3 presents scanned gate measurements revealing the presence of two quantum dots in the nanotube. The properties of one of these dots and the characteristics of the interaction between the dot and the AFM tip are studied quantitatively in section 6.4. The tip volt-

age dependence of the scanned gate images is explored in section 6.5, leading to an interpretation in terms of the electrostatic environment of the nanotube in section 6.6. The chapter concludes in sections 6.7 and 6.8 with a phenomenological model accounting for the major features of the scanned gate images.

6.2 Device Fabrication and Properties

The samples we study in this chapter and the next consist of individual single-walled carbon nanotubes grown by chemical vapour deposition (CVD) and electrically contacted by gold leads. These nanotube devices are fabricated by standard procedures on a degenerately-doped Si wafer with a 700 nm thick surface oxide. First, Fe-alumina catalyst islands are deposited on the oxide using a lift-off resist technique. The wafer is then placed in a CVD growth furnace at 900°C through which flows methane gas. This causes nanotubes to grow from the catalyst islands (Kong 1998, Hafner 1998). The nanotubes are subsequently located by AFM, and 50 nm Cr/Au leads are deposited on the sample by electron-beam lithography. These leads contact the nanotubes electrically at each end of the nanotube. Finally, the sample is glued to the sample holder with silver epoxy and connected electrically with wire-bonds. Note that an additional layer of gold 125 nm thick is added to the bonding pads to prevent the oxide from breaking during the wire-bonding process.

Nanotubes can also be grown by other techniques, such as laser ablation (Thess 1996) and arc discharge (Ebbesen 1997). The CVD growth method is used here because

of the high proportion of single-walled nanotubes that it tends to produce (Kong 1998). An equally important advantage of CVD growth is the ability to direct the growth of the nanotubes *in situ* through the placement of the catalyst islands. This avoids additional processing steps to deposit and position the nanotubes that may damage them by introducing defects. One disadvantage of CVD-grown nanotubes is the presence of large catalyst islands. Nanotubes are known to grow straight up from the catalyst particles, and can catch on an AFM tip (Hafner 2001). This was found to be a major problem on preliminary samples: nanotubes protruding from the catalyst can impede the oscillation of the AFM cantilever. This difficulty is mitigated in the sample studied here, however, by subjecting the catalyst islands to sonication during lift-off. Many small (<10 nm) particles break off from the island and are redeposited elsewhere on the oxide surface. Typically only one or two nanotubes grow from these small particles, and they tend to lie flat on the substrate, creating ideal conditions for AFM measurements.

A total of six nanotubes prepared as described above are measured in the next two chapters, but only one of these is measured using scanned gate microscopy in this chapter¹. AFM images of this nanotube are shown in Fig. 6.1. In Fig. 6.1(a) we see an image of the nanotube just after CVD growth, before contacts are put on the sample, while in Fig. 6.1(b) we see an image of the nanotube after 6 months of scanned probe measurements. The surface is very dirty in the latter image because of resist residue left over from fabrication and

1. Of the other five nanotubes, 3 are electrically contacted on only one side (the other contact is floating), and 2 are contacted on both sides but broken due to damage suffered during a cooldown attempt.

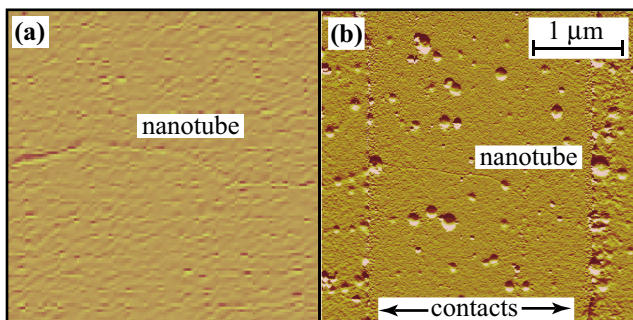


Fig. 6.1: AFM images of the nanotube sample used for scanned gate measurements. **(a)** Image taken at room temperature just after CVD growth. The nanotube is 1.3 nm tall. **(b)** Image after completion of all measurements. The gold contacts are visible on the left and right sides of the image. The nanotube is 2.5 μm long and horizontal between the contacts. The many spots in the images are resist residue and particles deposited during several months of scanning.

because of dirt deposited by the AFM tip during many months of scanning over the same area. From these images, we find that the nanotube is about 2.5 μm long, and has a height of 1.3 nm, confirming that it is almost certainly single-walled. Transport measurements show that there is very little gate voltage dependence of the conductance, so that the nanotube is metallic.

6.3 Scanned Gate Images in the Single-Electron Regime

The scanned gate measurements are performed as described in Chapter 2 (see Fig. 2.9). The nanotube is biased with a source-drain voltage V_{sd} , and its conductance is measured as a function of the position and voltage of the AFM tip at a temperature $T = 600$ mK. We begin by fixing the AFM tip in place 120 nm above the nanotube and measuring the conductance as a function of the tip voltage. The result is shown in Fig. 6.2: a series of sharp quasi-periodic peaks in the conductance that are separated by regions of vanishing conductivity. These look just like the Coulomb oscillations seen in the measurements of samples with extended backgates described in the previous chapter, where the nanotube forms one or more quantum dots at low temperatures. The only difference is that here it is

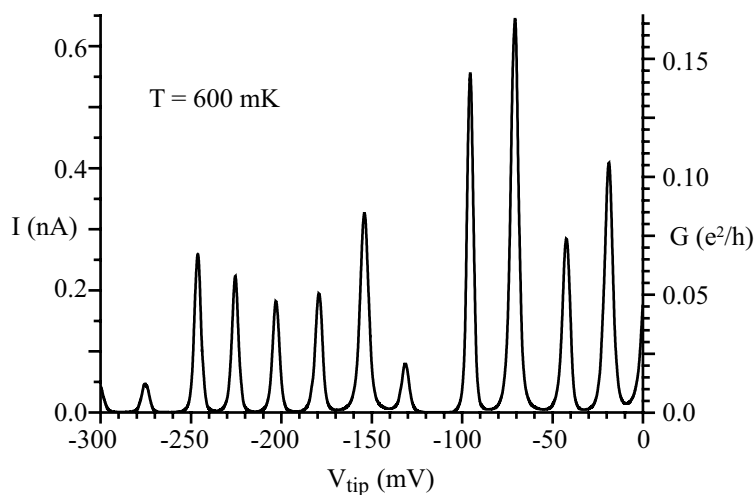


Fig. 6.2: Coulomb oscillations in the conductance of the nanotube as the AFM tip bias is changed. The tip is at a fixed position over the nanotube. Measurement taken at $T = 600$ mK, with a source-drain bias on the nanotube of 0.1 mV and a tip height above the nanotube of 120 nm.

the AFM tip rather than the backgate that gates the quantum dot, changing the electrostatic potential of the dot and modulating its conductance. We thus see that at least one quantum dot forms in this nanotube.

Knowing that the nanotube has formed at least one quantum dot, we next use the AFM tip to take a scanned gate image and determine the position of the dot(s). Fixing the tip voltage and then scanning the tip over the sample at a height of about 120 nm, we observe two distinct sets of concentric rings of maxima in the conductance, shown in Fig. 6.3. These rings are centered directly over the nanotube, as determined from topographic images of the nanotube. We relate the rings of conductance peaks seen in Fig. 6.3 to the Coulomb oscillations seen in Fig. 6.2 by noting that in Fig. 6.3 the change in the potential of the quantum dot is no longer due to changes in the voltage on the tip, but rather to changes in the position of the tip. Recall that the expression presented in Chapter 2 for the scanned gate potential perturbation $\delta\phi$ that occurs at the point (x_0, y_0) when the AFM tip is located at the point (x, y) is (Eq. 2.15):

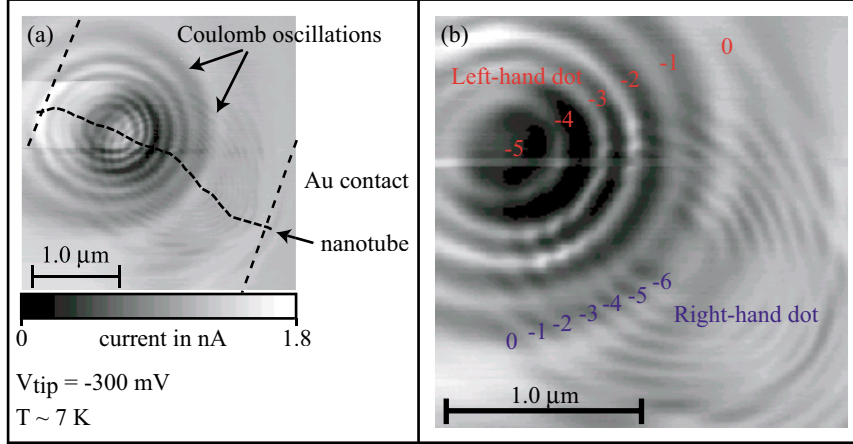


Fig. 6.3: Scanned gate images of the nanotube at $T \sim 6$ K. $V_{sd} = 0.1$ mV, $V_{tip} = -300$ mV, and $z = 120$ nm. **(a)** Two sets of concentric Coulomb oscillations reveal the presence of two quantum dots. The gold contacts and the nanotube are overlaid on top of the scanned gate image. **(b)** Charge states of the two dots as a function of the AFM tip position.

$$\delta\phi(x_0, y_0) = \left(\frac{1}{4\pi\epsilon}\right) \frac{C_{tip}(V_{tip} - \Phi)}{\sqrt{(x-x_0)^2 + (y-y_0)^2 + z^2}} \quad (6.1)$$

As discussed in Chapter 2, features in the scanned gate image follow equipotential contours surrounding the quantum dot. The quasi-periodic Coulomb oscillations of Fig. 6.2 thus become, in Fig. 6.3, concentric rings around the quantum dot with quasi-periodic spacings. These images represent to our knowledge the first scanned gate measurements of Coulomb oscillations in a quantum dot.

The fact that there are two separate sets of rings, each clearly centered around a different part of the nanotube, indicates the presence of two quantum dots. As mentioned in the previous chapter, quantum dots often form in nanotubes due to tunnel barriers between

the contacts and the nanotube. In order to form two quantum dots as seen here, yet another tunnel barrier must exist in the nanotube, this time in the middle of the nanotube between the two sets of circles in the scanned gate image (Fig. 6.3). This tunnel barrier does not appear to be associated with any of the bent sections of the nanotube that are visible in the topographic image overlaid on the scanned gate image in Fig. 6.3. It may instead be due to a defect in the nanotube or a potential fluctuation due to interaction with the substrate.

By comparing the spacing between the Coulomb oscillations around the two dots, as described in Chapter 1, we can compare the tip-dot capacitances and hence the sizes of the quantum dots. We find that the left-hand dot is about 2 times smaller than the right-hand dot. We can also see that while the left-hand dot is sufficiently small for the equipotential contours to be closely circular, the equipotential contours around the right-hand dot are obviously elliptical. This again betrays the latter's larger size. As a final observation, we note that we can label the occupancy of each dot, since each Coulomb oscillation corresponds to changing the occupancy by a single electron. This is shown for a magnified view of the Coulomb rings in Fig. 6.3(b).

These images were taken at $T \sim 6$ K, where the Coulomb oscillations are just starting to become visible. At this temperature, the conductance minima are not very strong, and the rings of conductance peaks can be very clearly seen around both dots. When the sample is cooled down further, the conductance minima become much closer to true zeroes and the peaks become much better defined. Because finite conduction is only measured

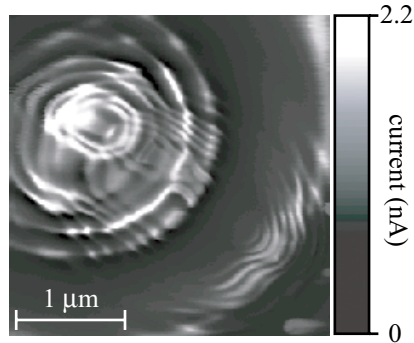


Fig. 6.4: Scanned gate image of the nanotube at $T = 600$ mK and $z = 120$ nm with $V_{tip} = -300$ mV. A log scale is used for clarity. The minima of the Coulomb oscillations are much stronger at lower temperature. Significant current flows only near the intersection of the Coulomb rings.

when neither quantum dot is blockaded, the scanned gate signal is significant only at the intersection of the Coulomb rings around the two dots. A scanned gate image using the same V_{tip} but taken at $T = 600$ mK is shown in Fig. 6.4 (a log scale is used for clarity). Here we can see that the concentric rings around the dots are broken up by strong conductance minima. Note that the left-hand dot, which is smaller and thus has a higher charging energy, has much stronger conductance minima than the right-hand dot.

6.4 Characterising A Quantum Dot and the Tip-Dot Interaction

The previous section showed that we can image Coulomb oscillations around quantum dots in a nanotube with scanned gate microscopy. In the nanotube studied here, we find two dots (Figs. 6.3 and 6.4). We now explore the properties of this nanotube further by quantitatively characterising one of the quantum dots in the nanotube (the dot on the right side of the nanotube in Fig 6.3) and its interaction with the AFM tip. This will prove helpful in understanding not only the scanned gate images in this chapter, but also the scanned force measurements in the following one.

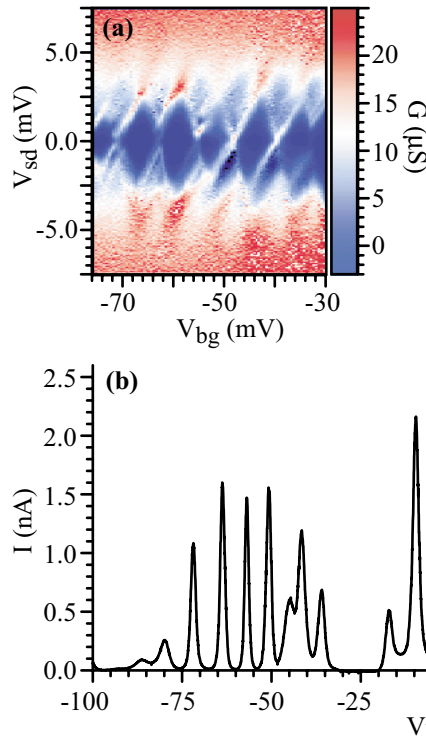


Fig. 6.5: (a) Conductance plot as a function of source-drain and gate voltages. Coulomb oscillations and excited states can be clearly seen. (b) High-resolution conductance trace as a function of back-gate voltage. The Coulomb oscillations are modulated by the larger period of the second quantum dot. All measurements made at 600 mK. The device parameters are summarised in Table 6.1.

We first obtain the parameters describing the quantum dot. The current through the device is measured while sweeping both V_{sd} and the voltage on the backgate, V_{bg} . The result is then numerically differentiated to produce the conductance plot shown in Fig. 6.5(a). A higher-resolution plot of the zero-bias conductance is also shown, in Fig. 6.5(b). From these plots, we determine the charging energy, as well as the level spacing, the peak widths, and the ratio α of the gate capacitance to the total capacitance, in the standard manner described in Chapter 1 and elsewhere (Sohn 1997). These parameters are summarised in Table 6.1. For comparison, some of the same parameters have been determined from Fig.

6.2, where the AFM tip is used to gate the dot instead of the backgate, and also listed in the table².

TABLE 6.1

| Parameter | Dot gated by backgate | Dot gated by AFM tip |
|--|-----------------------|----------------------|
| Coulomb peak height (maximum) | $0.25 e^2/h$ | $0.25 e^2/h$ |
| Coulomb peak spacing ΔV_g | 7.8 mV | 26 mV |
| Coulomb peak width ΔV_{peak} | 1.5 mV | 4.6 mV |
| Addition energy $E_{add}=\Delta E+U$ | ~3 meV | - |
| Excitation energy ΔE | ~1meV | - |
| Charging energy $U=e^2/C_{tot}$ | ~2 meV | - |
| Total capacitance of dot C_{tot} | 80 aF | - |
| Capacitance to gate C_g | 30 aF | 9 aF |
| Ratio of capacitances $\alpha = C_g/C_{tot}$ | 0.35 | 0.12 |
| Thermal peak width at 600 mK $4k_B T/\alpha$ | 0.6 mV | 1.7 mV |

There are two points worth noting about these results. First, we see that the AFM tip is only about one third as effective as the backgate at coupling to the dot: the period of the Coulomb oscillations is 3 times larger when using the tip instead of the backgate. This is because the tip, with a diameter of 100 nm, is considerably smaller than the dot, and hence only couples well to part of the dot at any one time. Second, we see that the width of the Coulomb oscillation peaks is about 3 times the value expected from thermal noise, given by $4k_B T/\alpha$. This indicates that the peaks are being broadened by coupling to the leads, which is not surprising given the fact that the peak conductance is quite high.

2. Note that the conductance plot in Fig. 6.5 is dominated by the effects of the (larger) right-hand quantum dot. This is because the conductance of the left-hand dot in Figs. 6.3 and 6.4 was changed shortly after these images were taken. Charged particles accidentally deposited near the nanotube during an AFM tip crash opened up the left-hand dot so that it had much weaker conductance oscillations.

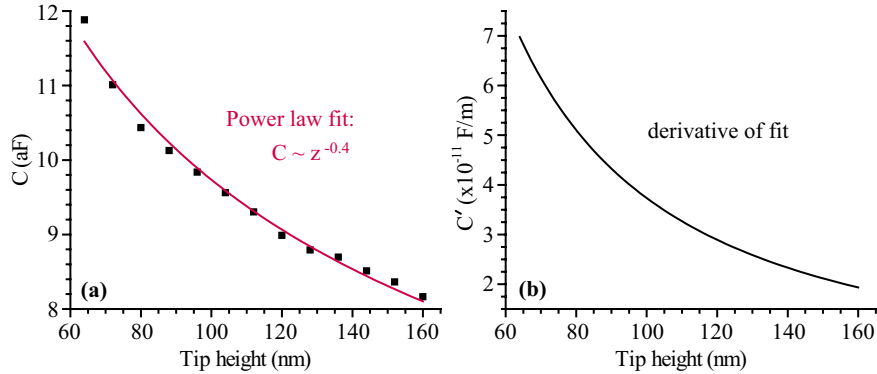


Fig. 6.6: (a) Tip-dot capacitance $C(z)$ as a function of the height of the tip z above the dot, measured from the periodicity of the Coulomb oscillations. The power law fit shows that $C \sim z^{-0.4}$. (b) First derivative of the tip-dot capacitance $C'(z)$, calculated from the fit to the capacitance. This will be useful for the force measurements in Chapter 7.

We next look at the interaction between this quantum dot and the AFM tip. From Fig. 6.2, we are able to determine the capacitance between the tip and the quantum dot, listed in Table 6.1. Another quantity that we can determine using scanned gate microscopy is the dependence of the tip-dot capacitance on the height of the tip above the dot. This is done by measuring the average separation of the conductance oscillations as a function of the tip voltage as the tip is lowered towards the sample. The result is shown in Fig. 6.6(a). Fitting the capacitance C to a power law in the tip height z as discussed in Chapter 2, we find that $C \propto z^{-0.4}$, close to the expected power of -0.5. We also plot in Fig. 6.6(b) the derivative of the capacitance, C' , as calculated from the fit to the capacitance. This will prove useful in Chapter 7 for measurements of the electrostatic force.

Finally, we investigate the effect on the scanned gate measurements of the noise δz_N in the height of the AFM tip above the sample. Since the tip-dot capacitance changes as

the tip moves up and down, as we have just seen, noise in z broadens the Coulomb oscillation peaks. We can express the broadening due to the tip motion as an effective charge noise δq_N on the quantum dot:

$$\delta q_N = C' \delta z_N (V_{tip} - \Phi) \quad (6.2)$$

Here Φ is the contact potential between the tip and the dot, and C' is the derivative of the tip-dot capacitance. We just measured C' in Fig. 6.6, and we know that $\delta z_{N,rms} \sim 0.25$ nm from measurements in Chapter 2. Hence we find an rms charge noise due to vibrations of about $0.02 e$ for a typical tip voltage of $(V_{tip} - \Phi) = 500$ mV. The charge resolution of the scanned gate measurement is therefore $0.02 e$ or less for typical values of V_{tip} . This is much less than the average width of the Coulomb oscillation peaks determined from Table 6.1, $0.2 e$, and also less than the expected thermal width of the peaks, $0.07 e$. The vibrational noise of the AFM therefore does not contribute significantly to the width of the Coulomb oscillation peaks.

We can study the effect of the AFM tip motion on the width of the Coulomb oscillations in greater detail by deliberately oscillating the tip. We drive the cantilever mechanically to oscillate the tip by a known amount, and then measure width of the Coulomb peaks. The width of the Coulomb oscillations as a function of tip voltage, ΔV_{peak} , can be approximated as the sum in quadrature of the natural peak width ΔV_0 and the peak width induced by the tip oscillation, $\delta q_N/C$:

$$\Delta V_{peak} \approx \sqrt{\Delta V_0^2 + \left[\frac{C'}{C} (V_{tip} - \Phi) \delta z \right]^2} \quad (6.3)$$

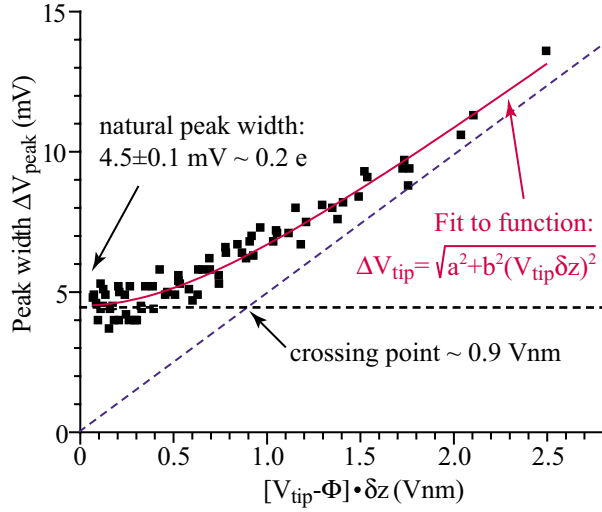


Fig. 6.7: Broadening of Coulomb oscillation peaks due to the motion of the AFM tip in z . The peak width is measured for several peaks near $(V_{tip} - \Phi) \sim 0.5$ V while mechanically oscillating the cantilever. The width changes little for small oscillation amplitudes, staying near the natural width 4.5 mV. At high oscillation amplitudes, the peak width grows linearly with the tip motion. The turning point where the tip motion begins to induce significant broadening of the Coulomb peaks occurs for an rms oscillation of 0.7 nm at typical V_{tip} .

In Fig. 6.7 we plot the peak width versus the product of the tip voltage and the oscillation amplitude (full width) for a number of peaks near $(V_{tip} - \Phi) \sim 500$ mV. This shows precisely the behaviour expected from Eq. 6.3. At small $V\delta z$ (small tip oscillation amplitudes), the peak widths show little increase in response to the tip oscillation, while at large $V\delta z$ (large oscillations) the peak widths increase linearly with $V\delta z$. The turning point between these behaviours occurs near $V\delta z \sim 0.9$ nm, *i.e.* near an rms oscillation amplitude (half-width) of $\delta z \sim 0.7$ nm for the typical V_{tip} used here. This corresponds to an induced charge $\delta q = C'(V_{tip} - \Phi)\delta z$ of $\sim 0.07 e$, about 1/3 of the natural peak width. Thus as long as the oscillation amplitude of the AFM tip is kept less than ~ 0.7 nm, the motion of the tip does not induce significant broadening of the Coulomb oscillation peaks for this quantum dot.

The measurements presented in this section demonstrate that we can quantitatively characterise the properties of the quantum dot using scanned gate microscopy. By exam-

ining the effect of the tip on the quantum dot, we see that we can also determine how much the tip is perturbing the dot and develop criteria for minimal perturbations. These results will be useful when investigating the sample using other scanned probe techniques such as EFM.

6.5 Tip Voltage Dependence of Scanned Gate Images

Having demonstrated the ability to image Coulomb oscillations from individual quantum dots in the nanotube, we next explore the evolution of the scanned gate images with changing tip voltage V_{tip} . We do this by scanning over the same area repeatedly, changing the tip voltage each time by 25 mV, to create a movie of the scanned gate images. A selection of eight frames from this movie is shown in Fig. 6.8. The full set of frames from the movie can be seen in the Appendix. Each image is taken at $T = 600$ mK and atip height of $z = 120$ nm, with a dc source-drain bias of $V_{sd} = 200$ μ V across the nanotube. For clarity of presentation, the current is shown on a log scale. The positions of the nanotube and the gold contacts, determined from topographic images, are superimposed over the image of the current in each frame.

Naively, we would expect that as the tip voltage increases from large negative V_{tip} , the circular Coulomb oscillations seen in Fig. 6.3 would simply shrink in towards the dot as V_{tip} approaches the contact potential of the nanotube, and then grow outwards again as V_{tip} becomes increasingly positive. This is the expectation from Eq. 6.1, since a given equipotential ring around the quantum dot will have a smaller radius as $\Delta V = V_{tip} - \Phi$ is

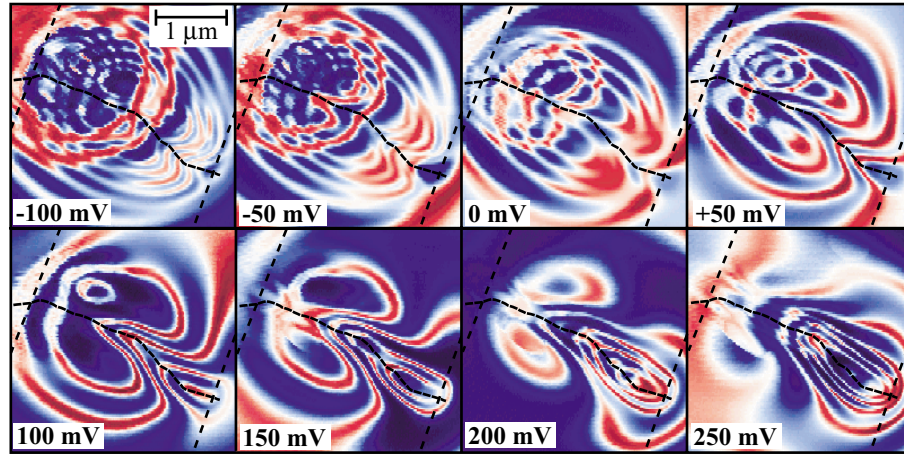


Fig. 6.8: Frames from movie showing evolution of scanned gate images with V_{tip} . The tip voltage is noted in each frame, as is the position of the nanotube and the contacts. The current is shown on a log scale (red is high, blue low). All images are taken at $T=600$ mK and $z=120$ nm, using a source drain bias of 0.2 mV.

decreased. Things are evidently more complicated than this simple picture would suggest, however. At large negative tip bias, all of the rings do indeed shrink as V_{tip} increases (*e.g.* -100 mV frame), and at large positive tip bias they all do grow with increasing V_{tip} (*e.g.* +250 mV frame), as expected from Eq. 6.1. At small positive tip voltages, however, there is a lot more going on. For these values of V_{tip} , some of the Coulomb oscillation rings expand with increasing V_{tip} while others contract. The Coulomb oscillation circles also distort considerably, growing “mouths” and side lobes (*e.g.* +0 to +150 mV frames), and there is even the development of Coulomb oscillations that are not centered over the nanotube (*e.g.* the “eye” in the frame at +100 mV).

By observing which rings grow with increasing V_{tip} and which ones shrink, we can distinguish between Coulomb oscillations that correspond to adding an electron to a dot and

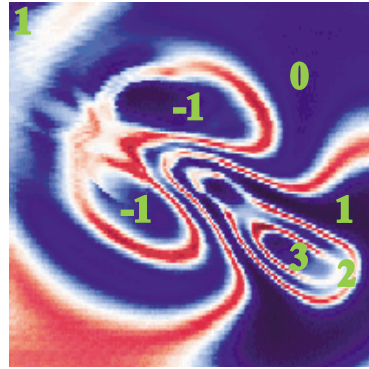


Fig. 6.9: Charge states associated with the right-hand dot at 150 mV tip bias. As the dot is approached from the upper left corner, first the tip removes electrons from the dot, then it adds them on. The current is shown on a log scale. Note that the left-hand dot is barely affected by the tip at this tip bias.

Coulomb oscillation that correspond to removing an electron. We can thus assign charge states to the dots between the Coulomb oscillations, just as in Fig. 6.3. The charge states associated with the scanned gate image measured at $V_{tip} = 150$ mV are shown in Fig. 6.9. At this tip voltage, the AFM tip scarcely affects the left-hand dot, and almost all of the features in the scanned gate image are due to the right-hand dot. Whereas in Fig. 6.3 at large negative V_{tip} the charge on the dot changes monotonically as the tip approaches the dot, here we see quite clearly that the charge on the dot can change non-monotonically as the tip approaches. Approaching from the right hand side of the dot, the electron occupancy of the dot increases monotonically, but approaching from the top of the dot, the occupancy first decreases before it increases.

6.6 Qualitative Interpretation of Scanned Gate Images

We can understand the behaviour observed in the scanned gate movie (Fig. 6.8) by considering the effects of the electrostatic environment of the nanotube on the conductance.

We have seen in Chapter 4 that the presence of dielectrics and conductors can distort fea-

tures in scanned gate images and complicate their interpretation. Similar mechanisms are responsible for the complex features observed here. The system we are measuring consists of not just an isolated AFM tip and carbon nanotube, but also two gold electrodes, a silicon backgate beneath a dielectric oxide ($\epsilon = 3.8$), and various charged particles lying on the oxide surface near the nanotube. All of these contribute to the electrostatic potential of the quantum dots in the nanotube and hence influence the conductance of the nanotube in the scanned gate images.

Consider first the influence of the many different conductors present near the nanotube quantum dot. Each conductor is made of a different material and therefore has a different workfunction. Workfunction differences between electrically-connected conductors give rise to an electrostatic potential between the conductors called the contact potential, as described in Chapter 2. Contact potential differences therefore exist not just between the nanotube and the AFM tip (analogous to the contact potential between the 2DEG and the tip seen in Chapters 3 and 4), but also between the nanotube and the gold contacts, the nanotube and the backgate, and the tip and the backgate. Associated with each of these contact potential differences are electric fields between the two conductors involved that can lead to complicated behaviour in the scanned gate images.

The effect of the contact potential difference between the nanotube quantum dot and the tip, Φ_{dot} , is just to shift the electrostatic potential felt by the dot from V_{tip} to $\Delta V = V_{\text{tip}} - \Phi_{\text{dot}}$ (as discussed in Chapter 2). This is a uniform factor, and therefore does not pro-

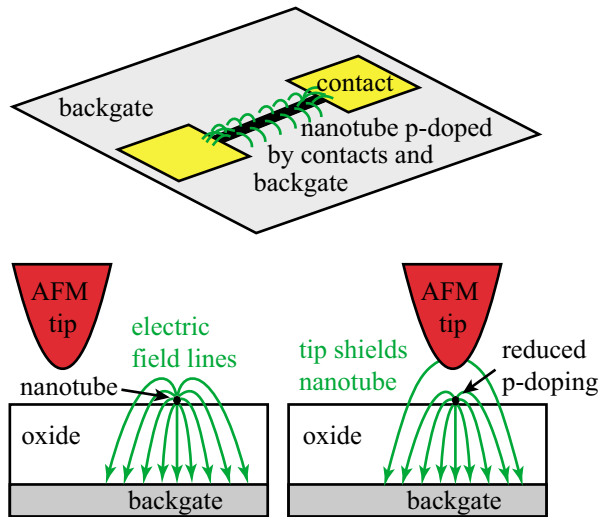


Fig. 6.10: Electric field lines due to the contact potential difference between the nanotube and the backgate and contacts. The contacts and backgate p-dope the nanotube. When the tip is close to the nanotube, it shields these field lines, reducing the p-doping of the nanotube and changing its conductance.

duce structure in the scanned gate image. The contact potentials between the nanotube and the backgate and contacts, on the other hand, produce effects that change as the AFM tip moves over the sample. This is illustrated in Fig. 6.10. As mentioned in Chapter 5, it is known empirically that the contacts and backgate frequently p-dope the nanotube, because the workfunction of the nanotube is lower than either that of the gold contacts or the Si backgate³. In Fig. 6.10 we therefore show electric field lines due to these contact potential differences that come out of the nanotube and terminate on the backgate and contacts. When the AFM tip approaches the nanotube, it screens these electric fields as illustrated. This reduces the amount of p-doping caused by the contact potential differences, increasing the electron occupancy of the quantum dot and hence changing the conductance of the nanotube. Note that this effect is only observed when the tip is close to the nanotube, as shown in Fig. 6.10, because the extended planar backgate screens the electric fields in the

3. The calculated workfunction of carbon nanotubes is ~ 4.5 eV (Saito 1998), while the value measured for gold is 5.1-5.3 eV and that for n-doped silicon is ~ 4.9 eV (Lide 1990).

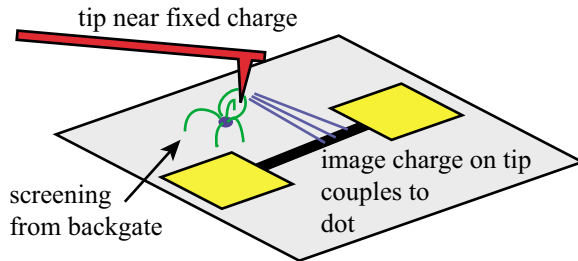


Fig. 6.11: Fixed charges on the oxide surface induce image charges on the AFM tip. The field from the image charges couples to the quantum dot, changing its electrostatic potential and hence its conductance.

sample at a length-scale $l \sim 200$ nm (the screening length) given by the apparent electrostatic depth of the oxide ($700 \text{ nm}/\epsilon \sim 200$ nm).

We next consider the effect on the scanned gate images of charged particles sitting on the oxide near the nanotube. Sources of such fixed charge include resist residue left after fabrication, detritus deposited by the AFM tip during scanning, impurities in the oxide, and dirt collected during sample preparation. The position and/or charge of these surface impurities has been observed to change on the time scale of hours to days, causing abrupt switching behaviour in the scanned gate images. This is especially true when large tip bias is used, which is why all measurements here are confined to $|\Delta V| < 500$ mV. On the time scale of the images in the scanned gate movie (Fig. 6.8), however, these particles are essentially fixed in charge and location. Nevertheless, they still affect the scanned gate images of the nanotube, in two ways.

The first way in which fixed charges can affect a scanned gate image of the nanotube quantum dot is through their effect on the potential difference between the tip and the sample. As discussed in Chapter 2, fixed charges on the surface induce an image charge

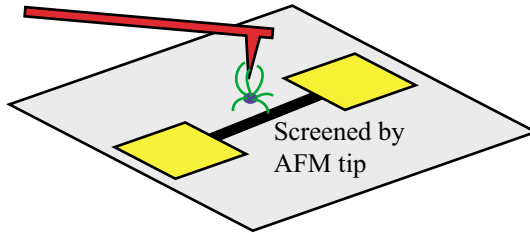


Fig. 12: Fixed charge in a carbon nanotube quantum dot

quantum dot. The conducting AFM tip screens the electric field from the fixed charges, changing the total electrostatic potential of the dot. Only charges close enough to the quantum dot to contribute to its electrostatic potential have this effect.

on the AFM tip. This establishes a dipole field between the tip and the charge which changes the potential difference ΔV between tip and quantum dot, as shown in Fig. 6.11. This is similar to the spatial variations in the effective contact potential of the 2DEG observed in Chapters 3 and 4. The magnitude of the change in ΔV depends on the amount of charge, the distance between the charge and the tip, and the distance between the tip and the quantum dot. Because of the screening from the backgate mentioned earlier, this effect is suppressed at length scales greater than l .

The second way in which fixed charges can influence the scanned gate images is through the screening properties of the AFM tip. This is demonstrated schematically in Fig. 6.12. If a fixed charge is located very close to the nanotube quantum dot, then it contributes to the electrostatic potential of the dot. When the AFM tip is far away, field lines from the fixed charge terminate on the dot as shown. When the tip approaches the charge, the tip screens the quantum dot from the field of the fixed charge, changing the electrostatic potential of the dot and hence its conductance. Thus even if the potential difference between the tip and the dot is set to zero, so that the direct effect of the tip on the dot conductance is

nulled, there will still be an indirect scanned gate signal due to the screening of the electric field from the fixed charge. As before, since the field from the fixed charge is screened by the backgate, only charges close to the quantum dot can have this effect on the scanned gate images.

This discussion of the effects of the electrostatic environment of the quantum dot on the scanned gate measurements is quite simplistic. Nevertheless, we believe it captures qualitatively the essential physics of the problem, although it may be difficult to distinguish between these effects experimentally. Given that all of the effects of fixed charges and contact potential differences mentioned above are going on at the same time, it is not surprising that the scanned gate images do not show just simple circles of Coulomb oscillations: there is no value of V_{tip} at which the tip has no effect on the nanotube conductance for all tip positions. This explains why the scanned gate images in Fig. 6.8 are never everywhere flat and featureless. Instead, the V_{tip} at which the tip does not affect the conductance changes as the tip moves around, depending on the local influence of fixed charges and contact potential screening. This is what gives rise to the complex structure seen in the scanned gate movie. Because these effects are screened by the backgate, much of the structure is observed close to the quantum dots.

6.7 Phenomenological Model of Scanned Gate Measurement

The interpretation presented in the previous section explains qualitatively the features seen in the scanned gate images. To go beyond a qualitative description of the results,

we model the electrostatics of the scanned gate measurement. The full self-consistent electrostatic problem represented by the scanned gate images is very difficult to solve, due to the non-trivial geometries involved. We can use the results of the previous section, however, to construct a simple phenomenological model that captures the most important physical elements. We do this by noting that for each location of the AFM tip, there is a tip voltage $\Phi_{0i}(x,y)$ for which the tip does not affect the occupancy of quantum dot i . At $V_{tip} < \Phi_{0i}(x,y)$ electrons are removed from the dot and at $V_{tip} > \Phi_{0i}(x,y)$ electrons are added to the dot, but for $V_{tip} = \Phi_{0i}(x,y)$ the occupancy is unchanged. The voltage $\Phi_{0i}(x,y)$ therefore defines an effective local contact potential between the dot and the tip. This effective contact potential incorporates all the effects of the electrostatic environment of the dot that were discussed in section 6.6, in addition to the intrinsic contact potential between the tip and the dot.

As discussed in Chapter 1, the conductance of the nanotube depends on the continuous charge induced on the quantum dots by the gate, δq . To model the scanned gate images, we express the continuous charge on the dot i induced by the AFM tip at position (x,y) , $\delta q_i(x,y)$, as:

$$\delta q_i(x, y) = C_i(x, y) \cdot [V_{tip} - \Phi_{0i}(x, y)] \quad (6.4)$$

Here, $C_i(x,y)$ is the capacitance between the tip and the quantum dot and $\Phi_{0i}(x,y)$ is the effective contact potential difference between the tip and the dot. In this simple model, all the spatial dependence of the scanned gate images is contained in two parameters for each

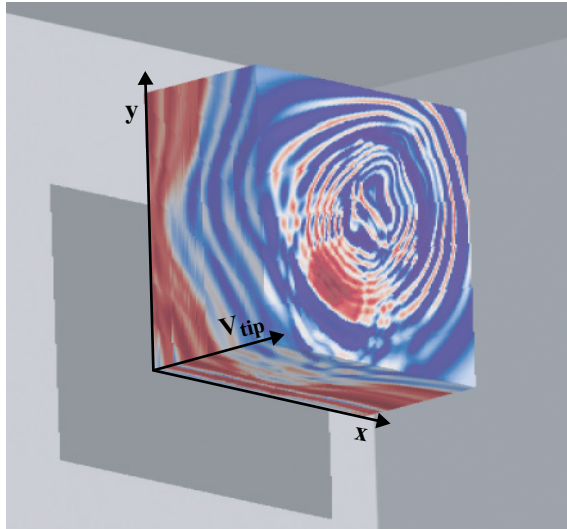


Fig. 6.13: Movie of scanned gate images of the nanotube conductance at $T = 600$ mK and $z = 120$ nm, using $V_{sd} = 0.2$ mV. Images with V_{tip} ranging from 60 mV to 415 mV in 5 mV steps have been stacked on top of each other to create a data cube. The capacitance between the quantum dot and the AFM tip at each point (x, y) is determined by taking a Fourier transform of the cube in the V_{tip} axis.

quantum dot, the capacitance $C_i(x, y)$ and the contact potential $\Phi_{0i}(x, y)$. Once we know these parameters, we can calculate the charge induced on the dots, and hence the conductance of the nanotube.

The capacitance $C_i(x, y)$ is determined from the periodicity in V_{tip} of the Coulomb oscillations of dot i when the tip is at the position (x, y) , using Eq. 1.6. To calculate the periodicity in tip voltage, a movie of scanned gate images with 5 mV steps in tip voltage between frames is used to create a three-dimensional data cube, shown in Fig. 6.13 (the frames are shown in the Appendix). The Fourier transform of this cube in the V_{tip} axis then allows the period of the Coulomb oscillations to be identified and the capacitance calculated. Once $C_i(x, y)$ has been determined, the contact potential $\Phi_{0i}(x, y)$ is found by examining the charge state of the dot in a single frame of the movie, *e.g.* as done in Fig. 6.9. The continuous charge $\delta q_i(x, y)$ is inferred from the patterns of Coulomb oscillation minima and maxima, and Eq. 6.4 is inverted to determine $\Phi_{0i}(x, y)$.

Note that the physical nature of the two parameters in the model, $C(x,y)$ and $\Phi_0(x,y)$, is quite different. The capacitance $C(x,y)$ depends only on the geometry of the AFM tip and the sample, in particular the distance between the tip and quantum dot. We expect it to be a smoothly decreasing function of the tip-dot separation. The effective contact potential $\Phi_0(x,y)$, on the other hand, contains all of the spatial information on the detailed configuration of fixed charges and contact potential differences. We therefore expect it to be a much more complicated function of the tip position. We also expect that it may change from time to time as charges move on the surface, *e.g.* due to forces applied by the tip voltage.

We also note that in principle, the calculation described above is far from straightforward for a multi-dot system, as the capacitances and charges for each dot have to be untangled. The calculation performed here, however, is aided by a fortuitous accident. Before the fine-scale scanned gate movie in Fig. 6.13 was made, the AFM tip accidentally crashed into the sample surface, depositing a large amount of charge near the nanotube (partly right next to the nanotube, mostly about 1-2 μm above the nanotube). This greatly increased the conductance of the left-hand dot seen in Figs. 6.3-6.5. As a consequence, the left-hand dot became much less sensitive to the AFM tip, and the scanned gate images in the movie shown in Fig. 6.13 are dominated by the quantum dot on the right side of the nanotube. The calculations that follow are therefore all performed exclusively for the right-hand quantum dot.

6.8 Quantitative Interpretation of Scanned Gate Images

When we perform the calculation of the model parameters for the quantum dot on the right side of the nanotube, the results we obtain for $C(x,y)$ and $\Phi_0(x,y)$ are shown in Fig. 6.14. In Fig. 6.14(a) we show a contour plot of the continuous charge $\delta q(x,y)$ on the dot, as inferred from the scanned gate image in Fig. 6.9 (where $V_{tip} = 150$ mV)⁴. The tip-dot capacitance $C(x,y)$ extracted from the movie in Fig. 6.13 is displayed as a contour plot in Fig. 6.14(b). In Figs. 6.14(c) and (d) we show results for the effective contact potential $\Phi_0(x,y)$, again as contour plots. The first is from the scanned gate image of Fig. 6.9 (for which we have shown the associated charge $\delta q(x,y)$ in Fig. 6.14(a)), and the second is from one of the frames in the movie of Fig. 6.13 ($V_{tip} = 200$ mV). This allows us to compare the effective contact potential before and after the tip crash and investigate the effect of the deposition of extra charges.

Looking first at $C(x,y)$ (Fig. 6.14(b)), we see that the tip-dot capacitance is a smooth, monotonic function that peaks over the center of the dot. The contour lines are only slightly oval far from the dot, but become progressively more elongated as the dot is approached. As expected, none of the complicated behaviour observed in the scanned gate image shows up in the capacitance—it is symmetric and slowly-varying. Note however that the capacitance does not go to zero as the tip moves far away; rather, it goes to about 3 aF. This indicates that there is a substantial part of the capacitance to the dot that is due

4. When inferring the charge δq for the model Eq. 6.4, care must be taken to ensure that δq be set to 0 far away from the nanotube, where the AFM has little effect on the quantum dot.

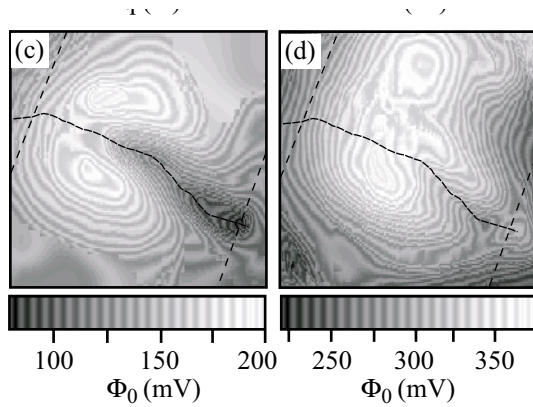


Fig. 6.14: Model of the scanned gate images. All images shown as contour plots. **(a)** Continuous charge $\delta q(x,y)$ on the right-hand dot as determined from Fig.6.9, in units of e . **(b)** Tip-dot capacitance $C(x,y)$ calculated from the Coulomb oscillation periodicity. The capacitance is smooth and monotonic. **(c)** Effective contact potential of the dot $\Phi_0(x,y)$ calculated from (a) using Eqn. 6.4. All of the fine spatial structure in (a) is due to $\Phi_0(x,y)$. The effects of screening the fields from the backgate and contacts are clearly visible. **(d)** Effective contact potential calculated after the AFM tip crashed into the sample. There are noticeable changes due to the deposition of charged particles during the tip crash.

to the cantilever rather than the tip itself. This is not a surprise, as the same effect was observed earlier in the experiments with 2D electron gases.

We consider next the effective contact potential $\Phi_0(x,y)$ calculated from the scanned gate image in Fig. 6.9 (Fig. 6.14(c)). As expected from the discussion in previous sections, this function varies strongly with tip position and is the source of all the complexity in the scanned gate images. There are three features to note in this image. First, far away from the nanotube, the effective contact potential difference Φ_0 between the tip and the nanotube is fairly flat, at about 150 mV. This far-field contact potential represents in some sense the intrinsic contact potential difference between the tip and the dot, ignoring all the effects of the electrostatic environment: we are far enough away from the dot that the backgate should screen out almost all of these effects. We note that the far-field Φ_0

found here is the same as the V_{tip} used to take the scanned gate image (Fig. 6.9) from which $\Phi_0(x,y)$ is calculated. This explains why the charge plot δq looks essentially the same as Φ_0 : the tip is only affecting the conductance through screening and image charges, not through the applied tip bias.

The second important feature we see in Fig. 6.14(c) is that when the tip is within a few hundred nm of the nanotube, there is a sharp dip in Φ_0 of about 30-40 mV, resulting in a contact potential over the quantum dot of 100-120 mV. This dip occurs along the whole length of the quantum dot and has a half-width at half-maximum of ~ 200 nm, equal to the screening length of the backgate. These observations strongly suggest that the dip in Φ_0 arises from screening by the AFM tip of the contact potential difference between the nanotube quantum dot and the backgate/contacts. As discussed in section 6.6, this screening lowers the p-doping of the nanotube, which effectively decreases Φ_0 . We can calculate from Figs. 6.14(b) and (c) the amount by which the screening from the tip reduces the p-doping of the nanotube, finding that it amounts to ~ 1 -1.5 electrons added to the dot.

The third feature we see in Fig. 6.14 (c) is that there are two irregularly-shaped peaks in Φ_0 in the center-left part of the image. One of these peaks is above the nanotube and the other is below it, both about 500 nm away from the nanotube. We attribute these peaks in the effective contact potential to the effects of fixed fixed charges lying on the oxide and/or the contact potential difference between the tip and the backgate, as discussed in section 6.6. We are not able to distinguish which of these effects contribute to this part

of the observed local contact potential. We can, however, specify what the net effect is: since Φ_0 is increased, the fixed charges and/or backgate contact potential are effectively p-doping the quantum dot via the AFM tip. Calculating the change in the charge on the dot using Fig. 6.14(c), we find that the tip induces up to $\sim 1.5 e$ on the dot at the two peaks.

This interpretation of the factors contributing to Φ_0 is reinforced by examining the effective local contact potential in Fig. 6.14(d), calculated from a scanned gate image taken after a tip crash deposited charge on the sample. Comparing Fig. 6.14(d) to Fig. 6.14(c), we see some of the same broad features, such as a dip in Φ_0 of about 20-30 mV when the tip is over the quantum dot. There are, however, some significant differences between the figures. For example, in Fig. 6.14(d) Φ_0 has everywhere increased by an average value of ~ 160 mV. Because this increase is close to uniform, we attribute it to charges on the tip that were picked up during the tip crash. The contact potential along the quantum dot has increased even more, to around 300-340 mV. Finally, an especially noticeable change occurs near the top of the scan range, where Φ_0 increases by an additional ~ 40 -50 mV. We interpret this in terms of additional fixed charge deposited by the tip. This interpretation is corroborated by the observation of new dirt-like features in the topography (not shown) at the same locations as the new feature in Φ_0 .

By analysing the scanned gate measurements in terms of the simple model presented in Eq. 6.4, then, we find that we can attribute all of the complex structure in the scanned gate images (Figs. 6.8, 6.13) to spatial variations in the effective local contact po-

tential $\Phi_0(x,y)$. We can account for the principal features in $\Phi_0(x,y)$ within this model in terms of image charges induced on the tip by fixed charges on the sample surface and screening of contact potential differences by the AFM tip. By depositing additional charges from the tip, we find that we can change the local contact potential $\Phi_0(x,y)$, demonstrating its dependence on fixed charges. We thus see that our phenomenological model successfully expresses the principal effects of the electrostatic environment of the quantum dot on the scanned gate measurements of the nanotube.

6.8 Summary

In this chapter we have for the first time demonstrated scanned gate microscopy of a quantum dot in the single-electron regime, imaging Coulomb oscillations in quantum dots in a metallic carbon nanotube. By using a simple model of how the AFM tip interacts with the electrostatic environment of the quantum dot, we have shown that the scanned gate images are sensitive to perturbations from fixed charges and conductors lying near the quantum dot. Single-electron scanned gate measurements can thus be a useful tool for characterising quantum dots and their electrostatic environment. In the next chapter, we will use what we have learned about the dot and the tip-dot system from scanned gate measurements to investigate force measurements in the single-electron regime.

CHAPTER 7: *Single-Electron Force Microscopy in Carbon Nanotubes*

7.1 Introduction

In the previous chapter, we showed that we can use the AFM to characterise a quantum dot in a nanotube and extract information about its electrostatic environment, by using the tip as a perturbative tool to change the electrostatic potential of the quantum dot. Now, we make use of the exquisite force sensitivity of the AFM to sense the motion of single electrons going on and off the nanotube. We find that the electrostatic force from single-electron motion causes not just a deflection of the cantilever, but also a shift in the resonance frequency of the cantilever, and even a degradation of the Q -factor of the resonance.

In section 7.2 we present EFM measurements of the same nanotube measured with SGM in the previous chapter, which we interpret quantitatively in section 7.3. Section 7.4 presents EFM measurements of several nanotubes that are contacted on only one side. In section 7.5 we turn to measurements of the frequency shift, which we interpret in section 7.6. We conclude with an investigation of the degradation of the cantilever Q , with measurements and interpretations presented in sections 7.7 and 7.8.

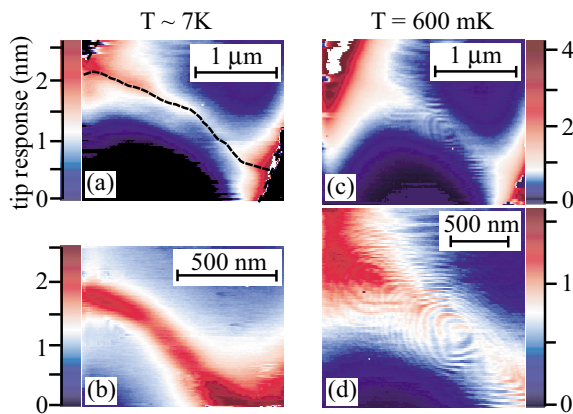


Fig. 7.1: ac-EFM images of the nanotube studied in Chapter 6, driving both electrodes self-resonantly (with 2.5 mV rms in (a) and (b), 1.2 mV in (c) and (d)). (a) At $T \sim 7$ K, the nanotube appears as a bright line between the electrodes. The position of the nanotube and electrodes is indicated in the image. $V_{tip} = -300$ mV and $z = 60$ nm. (b) Close-up of nanotube showing that the EFM signal at 7 K is almost featureless. The width of the EFM signal from the nanotube is ~ 130 nm. $V_{tip} = -400$ mV and $z = 40$ nm. (c) At $T = 600$ mK, concentric rings around the nanotube appear in the tip response. $V_{tip} = -400$ mV and $z = 100$ nm. (d) Close up image of the rings around the nanotube. $V_{tip} = -400$ mV and $z = 60$ nm.

7.2 Electrostatic Force Measurements

We begin by measuring the force on the AFM tip from the nanotube using the ac-EFM technique described in Ch. 2 (see Fig. 2.7). We apply a dc voltage V_{tip} to the tip while driving the contacts on both sides of the nanotube with an ac voltage of 2.5 mV rms, and we measure the resulting amplitude of the cantilever oscillation. Because the effective local contact potential varies considerably near the nanotube, as shown in the previous chapter (section 6.8), the resonant frequency of the cantilever changes with tip position. To ensure that the cantilever oscillation remains on resonance as the tip scans over the sample, a self-resonant circuit is used to drive the nanotube and the amplitude of the cantilever response is measured with an ac voltmeter, as discussed in Chapter 2 (see Fig. 2.8).

An EFM image of the nanotube at a temperature of $T \sim 7$ K is shown in Fig. 7.1(a). This is the same nanotube that was measured using SGM in the previous chapter. The position of the nanotube and the contacts (determined from topographic scans) is overlaid on the EFM image. The nanotube is clearly visible in this image as a bright line between the

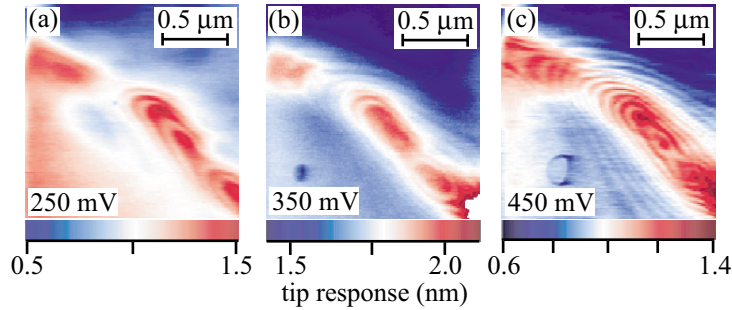


Fig. 7.2: Variation of EFM images with tip voltage. All images taken at $T=600$ mK and $z=60-80$ nm, driving both electrodes self-resonantly. (a),(b) 2.5 mV rms driving voltage. (c) 1.2 mV rms driving voltage.

electrodes. A higher-resolution image taken 40 nm above the sample shows that the EFM signal from the nanotube is essentially featureless, with a full width at half maximum of ~ 130 nm (Fig. 7.1(b)).

Similar pictures have been seen previously in EFM images of nanotubes (Bachtold 2000). At this elevated temperature, the thermal width of Coulomb oscillations ($4k_B T = 2.5$ meV) is similar to the charging energy of the quantum dot in the nanotube (2 meV, see Table 6.1). The driving bias of 2.5 meV is also similar to the charging energy. Single-electron effects are therefore smeared out, and the nanotube appears essentially featureless¹. The apparent width of the nanotube, 130 nm, is about what we expect when measuring with a tip of ~ 100 nm diameter sitting ~ 40 nm above the nanotube.

When we cool down the nanotube, the EFM image develops a lot of fine structure, which can be seen in Figs. 7.1(c) and (d). Where the nanotube appears as simply a bright line in the amplitude response of the cantilever at $T \sim 7$ K in Figs. 7.1(a) and (b), at $T = 600$

1. In the previous chapter, scanned gate images at $T \sim 6$ K showed weak Coulomb oscillations (Fig. 6.3) in contrast to the featureless AFM images at $T \sim 7$ K here. We believe the difference is because the source-drain bias in the scanned gate image is small ($V_{sd} = 0.1$ mV). The driving signal in the EFM image is large ($V_{ac} = 2.5$ mV), and thus smears out further the already weak Coulomb oscillations.

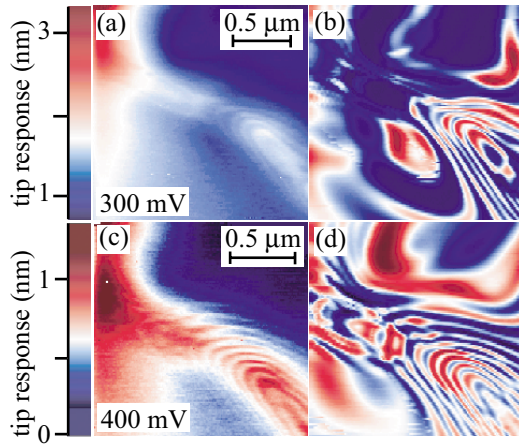


Fig. 7.3: Correspondence between scanned gate images and EFM images. All images taken at $T=600$ mK and $z=60$ nm. **(a)** EFM image of the center of the nanotube at $V_{tip}=300$ mV, driving both sides of nanotube self-resonantly with 2.5 mV rms. **(b)** Scanned gate image at the same V_{tip} as in (a), shown on a log scale for clarity. The Coulomb oscillation peaks occur at the same locations as the peaks in the EFM response. **(c)** EFM image of the same part of the nanotube at $V_{tip} = 400$ mV, driving with 1.2 mV rms. **(d)** Scanned gate image at the same V_{tip} as in (c). Again, the Coulomb oscillations occur at precisely the same locations as the peaks in the EFM response.

mK the EFM images contains two sets of multiple, concentric, quasi-circular peaks. Both sets of concentric rings are centered on the nanotube, one over the left 1/3 of the nanotube, the other over the right 2/3 of the nanotube. The magnitude of the amplitude response on the rings decreases monotonically as the tip moves further from the nanotube, until the rings fade away entirely ~ 300 nm away from the nanotube. The pattern of rings changes as the tip voltage is changed, as demonstrated by the series of images in Fig. 7.2.

These patterns of peaks in the response to the electrostatic force on the tip look remarkably like the patterns of peaks in the conductance measured in Chapter 6. In fact, when we measure a scanned gate image at the same location and under the same conditions as an EFM image, we find that the peaks in the force are aligned precisely with the Coulomb oscillation peaks in the conductance. This is demonstrated in Fig. 7.3 for two scans over the same part of the nanotube at different tip voltages. We therefore attribute these peaks to single-electron charging effects in the quantum dots studied with SGM in the previous chapter.

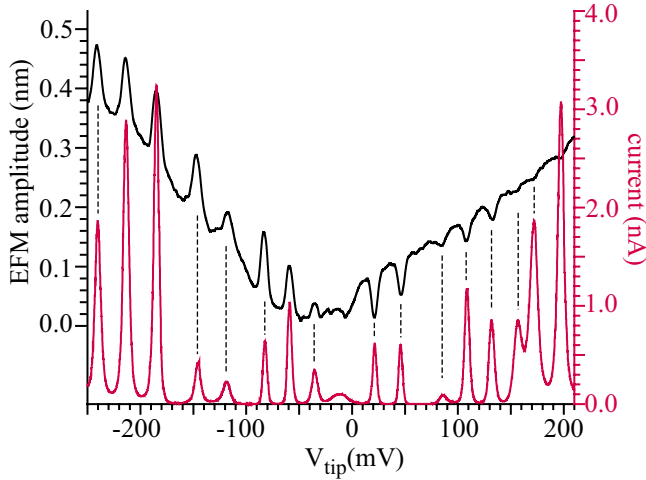


Fig. 7.4: EFM response of the AFM cantilever as a function of V_{tip} . The nanotube is driven on both sides with 0.7 mV rms at 34503 Hz, and the amplitude response is measured with a lock-in amplifier. The conductance of the nanotube as a function of V_{tip} is shown in red. The EFM response vanishes near -50 mV, growing linearly on either side. There are periodic modulations in the response that line up with the Coulomb oscillations in the conductance as indicated. Below -50 mV, these modulations represent an increase in the net force on the tip, while above -50 mV they represent a decrease in the net force. The modulations decrease in amplitude linearly as V_{tip} increases. $T=600$ mK and $z=120$ nm.

A more complete picture of the electrostatic force on the AFM tip can be obtained by measuring the force on the tip as a function of the tip voltage, shown in Fig. 7.4. Here, we fix the position of the AFM tip over the quantum dot on the right-hand side of the nanotube. We drive both sides of the nanotube directly with 0.7 mV rms at a fixed frequency near the resonant frequency of the cantilever, instead of using the self-resonant feedback loop². We then measure the amplitude response of the cantilever with a lock-in amplifier as the tip voltage is changed. The conductance of the nanotube is also measured, under identical conditions, and is plotted beneath the tip deflection.

We can identify from this figure several characteristics of the EFM response. First, the amplitude of the tip oscillation is zero near -50 mV, and grows roughly linearly with the

2. Driving at a fixed frequency provides two advantages: first, low-noise measurements can be made with a lock-in amplifier; and second, the oscillation amplitude can be kept small. A small oscillation is important both to ensure that the amplitude response remains in the linear regime, and also to ensure that the tip motion does not perturb the Coulomb oscillations too much (see Fig. 6.7). The self-resonant feedback loop requires a minimum oscillation amplitude of ~ 0.5 nm to function, and operates best at an oscillation amplitude of >1 nm, which is large enough to change the width of the Coulomb oscillations.

tip voltage on either side of -50 mV. On top of this linear background, there is a periodic modulation in the amplitude which lines up precisely with the Coulomb oscillation peaks in the conductance. This correspondence is shown by the dotted lines in Fig. 7.4. At tip voltages lower than -50 mV, the modulations are all increases in the amplitude above the linear background, representing an increase in the net force on the tip. For tip voltages above -50 mV, on the other hand, they are all decreases below the linear background, representing a decrease in the net force on the tip. The size of these modulations decreases roughly linearly as V_{tip} becomes more positive, becoming difficult to see above 200 mV.

7.3 Interpretation of EFM Measurements

We can understand the observations in the previous section in terms of a simple model of the forces on the AFM tip, illustrated in Fig. 7.5. The tip is driven into resonance by two sources of electric field: the electrodes and the nanotube quantum dot. Because of the Coulomb oscillations in the conductance of the quantum dot, however, its ability to drive the tip depends sensitively on the tip voltage. Just as in the scanned gate measurements, the dot opens and closes as the AFM tip approaches or the tip voltage changes, alternately allowing current to flow and then blockading it. When the dot is blockaded and no electrons can jump on or off, the dot exerts little ac force on the tip, and the cantilever is deflected mainly by the force from the electrodes. When the dot is open, however, an electron can hop on and off the dot at the driving frequency ω_0 . This changes the electrostatic potential of the dot at the driving frequency, exerting an additional force on the tip.

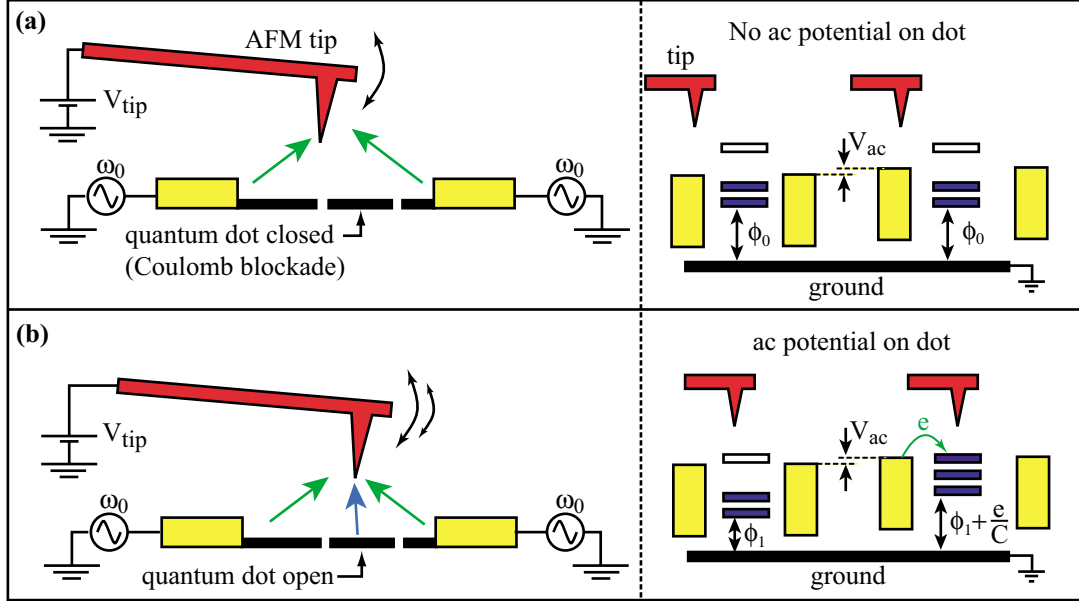


Fig. 7.5: Coulomb oscillations in the electrostatic force on the AFM tip. **(a)** When the dot is blockaded, no electrons can hop on or off, and there is little ac potential on the dot. The EFM signal comes mainly from the electrodes. **(b)** When the dot is open (*i.e.* on the conductance peaks), a single electron can hop on and off each cycle of the driving frequency. This causes an ac potential on the dot, which contributes to the EFM signal. Coulomb oscillations are therefore observed in the force on the tip.

The periodic modulations in the tip response thus represent the force on the tip from single electrons moving on and off the dot. This picture explains the exact correspondence between the scanned gate images and the EFM images.

Expressing this model mathematically, the total force on the tip F_{tot} consists of components from the electrodes, F_{el} , and the quantum dot, F_{dot} . If the sample is being driven from both electrodes with a voltage at the resonant frequency of the cantilever,

$V = V_{ac} \cos(\omega_0 t)$, then the force on the tip is:

$$F_{tot} = F_{el} + F_{dot}$$

$$F_{el} = C'_{el}(V_{tip} - \Phi_{el}) \cdot V_{ac} \quad (7.1)$$

$$F_{dot} = C'_{dot}(V_{tip} - \Phi_{dot}) \cdot V_{ac}^{dot} \quad (7.2)$$

Here, C_{el} is the capacitance between the electrodes and the AFM tip, Φ_{el} is the contact potential between the tip and the electrodes, C_{dot} is the capacitance between the tip and the dot (which until now has been called just C), and Φ_{dot} is the contact potential between the tip and the dot.

The term V_{ac}^{dot} represents the ac electrostatic potential of the quantum dot. This is not the same as the ac potential of the electrodes, since the potential of the dot changes abruptly near a Coulomb oscillation. We calculate V_{ac}^{dot} from the total electrostatic potential of the quantum dot, ϕ (see Chapter 1, Eq. 1.3), by noting that applying the ac potential V_{ac} to both electrodes is to a good approximation equivalent to applying the same potential V_{ac} to the backgate³. Assuming that V_{ac} is less than the width of the Coulomb oscillations, we obtain:

$$V_{ac}^{dot} = \left(\frac{\partial \phi}{\partial q} \right) C_g V_{ac} \quad (7.3)$$

$$F_{dot} = C'_{dot}(V_{tip} - \Phi_{dot}) \cdot \left(\frac{\partial \phi}{\partial q} \right) C_g V_{ac} \quad (7.4)$$

where C_g is the capacitance between the backgate and the dot and q is the continuous charge on the dot, defined in Chapter 1.

We recall from Chapter 1 that the electrostatic potential ϕ of the dot decreases slowly in the Coulomb blockade regime as q builds up on the dot due to the gate voltage,

3. In this approximation, we neglect the capacitive coupling between the tip and the quantum dot.

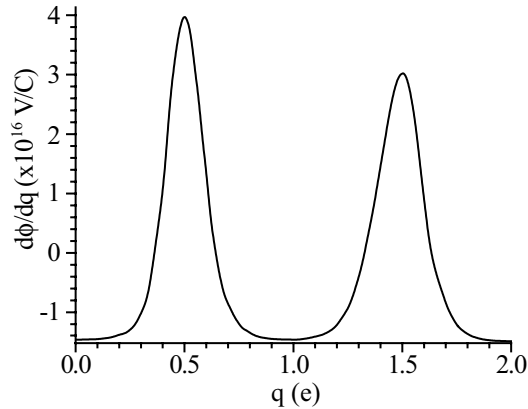


Fig. 7.6: Change in the electrostatic potential ϕ of the quantum dot as a function of the continuous charge q induced on the dot by the AFM tip. This is calculated here from two typical adjacent peaks in the conductance as a function of tip voltage.

but then jumps abruptly at each Coulomb oscillation by an amount equal to the charging energy e/C (see Fig. 1.4). The change in the electrostatic potential $\frac{\partial\phi}{\partial q}$ is thus highly peaked at the Coulomb oscillations. In fact, it has the same shape as the peaks in the conductance. It can therefore be calculated by simply scaling the conductance peaks so that the integral over one Coulomb oscillation is equal to the charging energy, and then offsetting the result from 0 to account for the decrease in ϕ between Coulomb oscillations. A plot of $\frac{\partial\phi}{\partial q}$ calculated in this way from two typical conductance peaks is shown in Fig. 7.6. Note that it is because the change in the electrostatic potential of the dot $\frac{\partial\phi}{\partial q}$ is so highly peaked at the Coulomb oscillations that the dot causes peaks in the force on the AFM tip at the Coulomb oscillations.

Using Eqs. 7.1-7.4, we can now account for all of the features in the EFM measurement of Fig. 7.4. The linear background is the force from the electrodes. This force goes to zero at the contact potential of the electrodes, ~ -50 mV, creating a “V” shape centered on the electrode contact potential. The peaks and valleys on top of the linear background

are the force from single-electron charging events in the dot. This goes to zero at the contact potential of the dot, ~ 300 mV, which is not the same as the contact potential of the electrodes (as discussed in Chapter 6). It is because the two contact potentials are not the same that the force from the dot causes a peak in the tip response for some tip voltages, and a dip for others. When the tip voltage is below the contact potentials of both the tip and the dot, then the force from the dot and the force from the electrodes have the same sign, giving rise to a peak in the response. When the tip voltage is between the two contact potentials, however, the forces have opposite signs, giving rise to a dip in the response.

We can quantitatively analyse the EFM signal in Fig. 7.4 using Eqs. 7.1-7.4. In order to do this, however, we must first correct for the fact that the driving frequency is not on resonance at all tip voltages: the driving frequency is fixed, while the resonance frequency varies with tip voltage, as described in Chapter 2. Recall that the transfer function of the cantilever response (from Eq. 2.2) is:

$$H(\omega, \omega_0) = \frac{Q}{k} \cdot \frac{1}{\sqrt{Q^2(1 - (\omega/\omega_0)^2)^2 + (\omega/\omega_0)^2}} \quad (7.5)$$

We calculate this transfer function from the measured V_{tip} dependence of the resonant frequency ω_0 (not shown). The measurements of Fig. 7.4 are then scaled by the transfer function, so that the response becomes what would be expected if cantilever were on resonance at all V_{tip} . The result is plotted in Fig. 7.7 (a) along with the transfer function as an inset. Note that the slopes of the two arms of the “V”-shaped background are now equalised. The

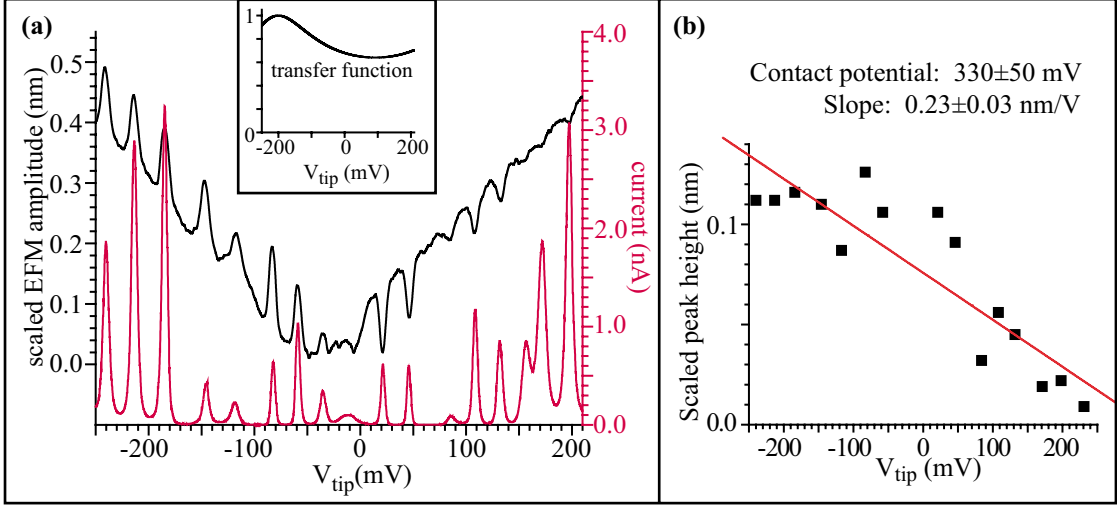


Fig. 7.7: (a) EFM response measured in Fig. 7.4, scaled by the transfer function of the cantilever resonance (shown in inset). The transfer function (Eq. 2.2) gives the frequency-dependent amplitude response of the cantilever. Here the EFM signal is scaled so that it is as if the cantilever were on resonance at all V_{tip} . (b) Magnitude of the Coulomb oscillations in the force. The Coulomb oscillations go to zero at the contact potential of the dot.

scaled heights of the peaks and dips in the tip response are extracted and plotted separately in Fig. 7.7 (b).

We first look at the part of the force from the electrodes alone, the “V”-shaped background. From the position of the zero of the tip response (the apex of the “V”) we determine the contact potential of the electrodes, finding $\Phi_{el} \sim -50 \pm 10$ mV. From the slope of the background, we determine the derivative of the tip-electrode capacitance. On resonance, the amplitude response to the force from the electrodes is $z = \left(\frac{Q}{k}\right) F_{el}$. Using Eq. 7.1, the slope of the linear background with respect to V_{tip} is therefore just:

$$\frac{dz}{dV_{tip}} = \left(\frac{Q}{k}\right) (C'_{el} \cdot V_{ac}) \quad (7.6)$$

Knowing $V_{ac} = 0.7$ mV, $Q = 31\,000$, $k = 3 \pm 0.5$ N/m, and using the slope measured from Fig. 7.4 of $dz/dV_{tip} = 1.8 \pm 0.1$ nm/V, we can calculate C'_{el} , finding $C'_{el} = 2.5 \pm 0.4 \times 10^{-10}$ F/m.

Next we consider the force from the quantum dot. From the linear fit to the force peaks shown in Fig. 7.7(b), we obtain the contact potential of the dot, finding $\Phi_{dot} = 330 \pm 50$ mV. This is the same as the value of the effective local contact potential $\Phi_0(x,y)$ deduced from the phenomenological model of SGM in Chapter 6, where we found that $\Phi_0 \sim 300$ -340 mV over the quantum dot⁴. The derivative of the tip-dot capacitance C'_{dot} is determined from the slope of the linear fit to the force peaks shown in Fig. 7.7 (b), similarly to the way that C'_{el} is calculated. Now, however, the slope of the amplitude response $\frac{dz}{dV_{tip}}$ is governed by Eq. 7.4, and we have:

$$\frac{dz}{dV_{tip}} = \left(\frac{Q}{k}\right) (C'_{dot} \cdot V_{ac}) \cdot \left(\frac{\partial\Phi}{\partial q}\right) C_g \quad (7.7)$$

We know from Fig. 7.6 that the height of the peaks in $\frac{\partial\Phi}{\partial q}$ is $\sim 5 \pm 0.5 \times 10^{16}$ V/C for typical Coulomb oscillations in this quantum dot, while from Table 6.1 we know find that the back-gate capacitance is $C_g = 30$ aF. Given the measured slope of the amplitude response, 0.23 ± 0.03 nm/V, we calculate that $C'_{dot} = 2.1 \pm 0.5 \times 10^{-11}$ F/m for the tip height of 120 nm used in this measurement⁵. This is similar to the result obtained from scanned gate meas-

4. The EFM measurements in this chapter were all taken after the tip crash mentioned in Chapter 6, so that we compare them to the scanned gate results after made after the tip crash.

5. Note that due to the dependence of F_{dot} on $\frac{\partial\Phi}{\partial q}$, we expect there to be variations in F_{dot} from peak to peak arising from variations in the conductance peak shapes. This contributes to the scatter of peak heights in Fig. 7.7(b).

urements in Chapter 6 (Fig. 6.6(b)), where we found $C'_{dot} = 2.9 \pm 0.2 \times 10^{-11}$ F/m at a tip height of 120 nm. This agreement between the scanned gate results and the EFM results gives us confidence in the accuracy of our model.

Note that the picture we have presented here says that the quasi-periodic peaks in the EFM images in Figs. 7.1-7.4 are all due to the force exerted by single-electron charging events in the quantum dot. Each of these peaks that we observe so clearly corresponds to the force exerted by a single electron moving onto or off of the dot. This is really quite remarkable: the AFM is feeling the motion of individual electrons! The magnitude of this single-electron force can be determined from the amplitude of the peaks in the EFM signal (Fig. 7.4). We find that at a tip-sample voltage $V_{tip} - \Phi_{dot} \sim 300$ mV, the force is only about 10 fN. Small as this is, it is still 1.5 orders of magnitude larger than the force sensitivity of the AFM, $0.3 \text{ fN/Hz}^{1/2}$ (see Table 2.1). We thus have more than enough sensitivity for detecting the force exerted by single electrons moving on and off the quantum dot.

7.4 Investigating Other Nanotubes

Until this point, all of the measurements (both SGM and EFM) have been on the same nanotube, the one shown in Fig. 6.1. All of the other nanotubes are broken or have contacts that are not electrically connected. To make EFM measurements, however, we do not need to have conduction through the whole nanotube; it is sufficient to have electrical contact to only one side of the nanotube, as mentioned in Chapter 5. This allows us to use EFM to investigate nanotubes with only one accessible contact. Recall that we have shown

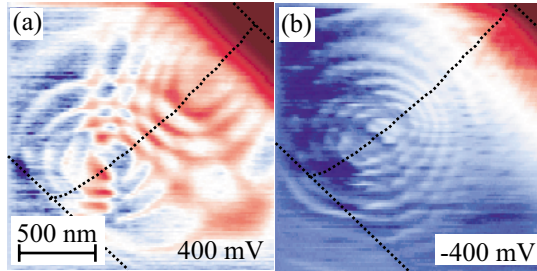


Fig. 7.8: EFM images of a semiconducting nanotube contacted on only one side (upper right contact). The EFM signal is shown on a log scale for clarity. The location of the nanotube and contacts is shown overlaid on the EFM image. Two quantum dots of roughly equal size are visible. The images are taken at $T = 600$ mK and $z = 100$ nm, driving with $V_{ac} = 2.5$ mV rms.

in the previous section that the Coulomb oscillations in the force on the AFM tip correspond precisely to the Coulomb oscillations in the conductance measured by scanned gate. We can therefore use EFM to image quantum dots in nanotubes that are broken or have only one contact and learn the same type of information that we learned with SGM: the number of dots, their locations, their capacitances to the AFM tip, their contact potentials, etc. In this section we present a brief survey of EFM images from four of the other nanotubes on the sample.

Shown in Fig. 7.8 are two EFM images of a $1.5 \mu\text{m}$ long nanotube. The location of the contacts and the nanotube determined from topographic images are overlaid on the EFM image. The lower contact on this nanotube is grounded because of a broken lead wire. Transport measurements made before the contact was broken indicate that this nanotube is semiconducting. The EFM images in Fig. 7.8 show clearly that there are two quantum dots in this nanotube. Neither dot is associated with an obvious defect in the nanotube like a bend. The Coulomb oscillations around both dots are slightly oval in shape, indicating that the dots are quite large. From their shapes and their positions on the nanotube, they appear to be roughly equal in size, and hence about $0.75 \mu\text{m}$ long.

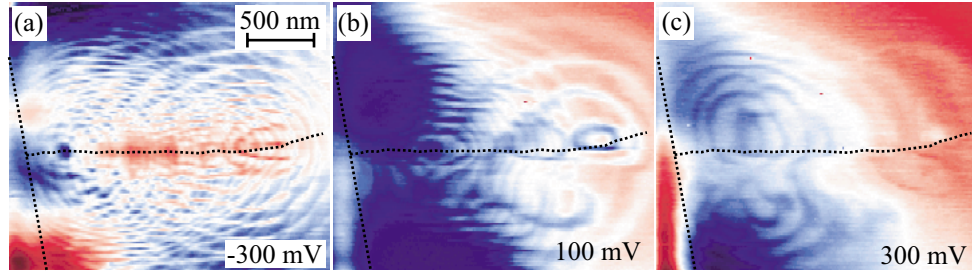


Fig. 7.9: EFM images of a nanotube contacted on only left side. The positions of the contact and the nanotube are overlaid on the image. Several dots (4 or 5) can be seen in this nanotube with careful inspection. (a),(b),(c) Evolution of EFM images with V_{tip} . Behaviour such as rings off the axis of the nanotube is seen, suggesting that the electrostatic environment of the nanotube is not simple. All images taken at $T=600$ mK and $z=100$ nm, with $V_{ac}=2.5$ mV rms ((a) and (c)) or 1.2 mV rms (b).

Another nanotube is imaged with EFM in Fig. 7.9. This one is $3.5 \mu\text{m}$ long and is connected electrically only on the left-hand side. We show only the left half of the nanotube in these images because there is no EFM signal from the right half of the nanotube (presumably due to a large tunnel barrier or break in the middle of the nanotube). The locations of the contact and the nanotube determined from a topographic image are overlaid on the EFM images. Once again, we see that there are multiple quantum dots in the nanotube—in this case, close inspection reveals 4 or possibly 5. Some of these dots have Coulomb oscillations that are quite circular, indicating that they are fairly small (*e.g.* the left-most dot in Fig. 7.9(a)), while others have distinctly elliptical Coulomb oscillations, indicating that they are larger (*e.g.* the right-most dot in Fig. 7.9(a)). Again, none of these dots seems to be associated with obvious structural defects like bends in the nanotube. If we look at the evolution of the Coulomb oscillations with V_{tip} , shown for two different values of V_{tip} in Figs. 7.9(b) and (c), we find that the images are reminiscent of the complex be-

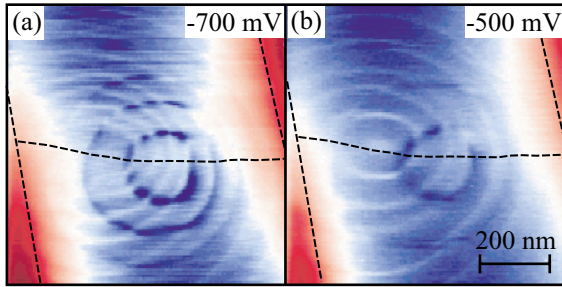


Fig. 7.10: EFM images of a broken metallic nanotube at two different tip voltages. This 800 nm long nanotube has two quantum dots. The Coulomb oscillations around the dot on the left are more elliptical in shape and more closely spaced than the Coulomb oscillations around the dot on the right, indicating that the dot on the left is larger. Images taken at $T=600$ mK and $z=100$ nm, driving with $V_{ac}=1.2$ mV rms.

haviour observed in scanned gate measurements in the previous chapter. This suggests that screening by the AFM tip of fields from contact potential differences and surface charges plays an important role, just as it did in Chapter 6.

EFM images of two more nanotubes are shown in Figs. 7.10 and 7.11. Both nanotubes are contacted on each side, but they are broken and do not conduct. Yet again, we see multiple quantum dots. The nanotube in Fig. 7.10, which is known to be metallic, has two quantum dots even though it is only 800 nm long. The Coulomb oscillations around the dot on the left are slightly elliptical while those around the dot on the right are more closely circular, indicating that the dot on the left is larger. In the nanotube shown in Fig. 7.11, also only 800 nm long, we see even more quantum dots: about 4-5. The Coulomb oscillations around these dots have a very large periodicity, indicating that the dots are very small; in fact, in many cases we only see one or two rings around each dot⁶. Note that in Figs. 7.11(a) and (b) some Coulomb oscillations are observed in the upper left corner of the

6. In both of these nanotubes, some Coulomb oscillations produce a positive force on the tip and some produce a negative force (*e.g.* Figs. 7.10(a) and (c)). This could be due to the dots having quite different contact potentials. Another possibility is that it results from a degradation of the Q of the cantilever at the Coulomb oscillation for certain dots. This effect will be discussed in detail in section 7.6.

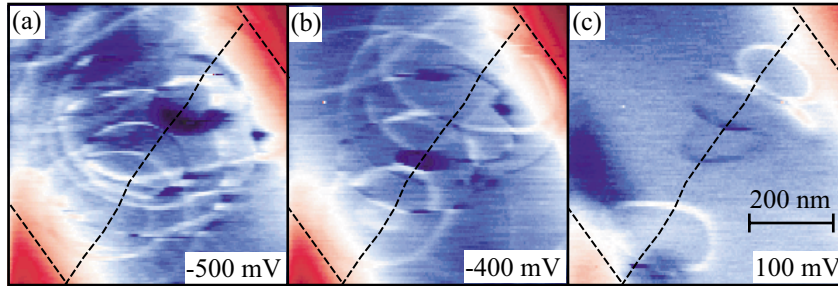


Fig. 7.11: EFM images of another 800 nm long broken nanotube at three different tip voltages. This nanotube has ~ 4 -5 dots with very large Coulomb oscillation periods, indicating that the dots are very small. Some dots have only one Coulomb oscillation visible around them. The Coulomb oscillations seen in the upper left corner come from a nearby nanotube connected to the upper contact. Images taken at $T=600$ mK and $z=80$ nm, driving with $V_{ac}=1.2$ mV rms.

image, coming from a point outside of the scan range. These are due to a second nanotube nearby that is contacted by the electrode on the right.

In this section, we have restricted ourselves to simple EFM images of the quantum dots, to get a feel for the variety of behaviour that can occur. In principle, though, we could go beyond this and characterise the individual quantum dots in these nanotubes with EFM in much the same way we did with SGM in Chapter 6. For example, by placing the AFM tip over the dot and measuring the Coulomb oscillations in the EFM response as a function of V_{tip} as was done in Fig. 7.4, the tip-dot capacitance C_{dot} and contact potential Φ_{dot} can be determined. Repeating such measurements at different tip heights then yields the capacitance derivative C'_{dot} , as in Fig. 6.6. The capacitance between the dot and the backgate C_g can be found similarly, by varying the backgate voltage rather than the tip voltage⁷.

Knowing these parameters, the height of the single-electron force peaks can be used to cal-

7. This may be difficult if there are many dots in the nanotube. In this case, C_g may be determined indirectly by comparing the amplitude of the Coulomb oscillation in the force (Eq. 7.4) to the amplitude of the Coulomb oscillations in the frequency (to be discussed later, Eq. 7.9).

culate the function $\frac{\partial\phi}{\partial q}$ from Eqs. 7.4-7.6, yielding the charging energy of the dot. Although we do not perform such a characterisation of a quantum dot with EFM here, the procedure is in principle straightforward.

This completes our brief survey of single-electron EFM of quantum dots in nanotubes. One of the important conclusions from the collection of images shown here is that all of the nanotubes we investigate form multiple quantum dots. Tunnel barriers within the nanotube, and not just at the contacts, thus seem to occur generically. None of the tunnel barriers defining the quantum dots that we observe is associated with a bend in the nanotube, even though a few of the nanotubes do have bends in them. The dots thus appear to result from microscopic defects in the nanotubes or local potential fluctuations. The average frequency of these defects, determined simply from the number of quantum dots observed in the EFM images, appears to be about 1 every 500 nm⁸.

7.5 Frequency Shift Measurements

The previous sections have investigated the force on the AFM tip from single-electron charging in nanotubes. We have seen that Coulomb oscillations in the occupancy of a quantum dot in the nanotube cause peaks in the force on the tip due to the sharp change in the electrostatic potential of the dot. Single-electron charging of a quantum dot should affect not just the force on the tip, however, but also the derivative of the force. As a result,

8. This is actually an overestimate of the actual frequency of defects, since in the broken nanotubes some of the “defects” that define the quantum dots are actually the breaks in the nanotube.

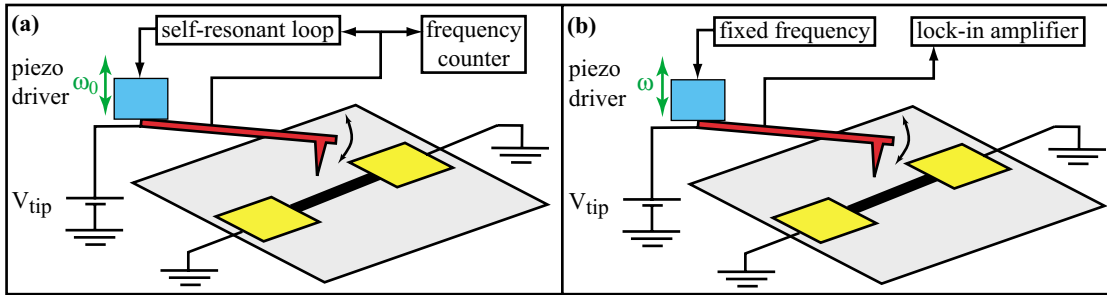


Fig. 7.12: Measuring Coulomb oscillations in the cantilever resonance frequency. **(a)** Direct measurement. The cantilever is driven into resonance mechanically using the self-resonant feedback loop, and the frequency of the resonance is measured with a counter. **(b)** Indirect measurement. The cantilever is driven mechanically at a fixed frequency near resonance. The change in the amplitude of the cantilever response due to changes in the resonant frequency are measured with a lock-in amplifier. The frequency is inferred from the transfer function of the cantilever resonance (Eq. 7.5).

we might also expect to see shifts in the resonance frequency ω_0 of the cantilever whenever there are Coulomb oscillations in the conductance.

We detect these frequency shifts in two equivalent ways, illustrated schematically in Fig. 7.12. The first method is to count directly the frequency of the cantilever oscillation. In this measurement, the sample is grounded while the cantilever is driven into resonance mechanically by a piezoelectric driver (Fig. 7.12 (a)). When the AFM tip voltage causes Coulomb oscillations in the occupancy of the quantum dot, the changing force derivative shifts the resonant frequency, which is measured directly by the frequency counter. To ensure that the oscillation remains on resonance at all times, a self-resonant positive feedback system is used as in the EFM measurements. The second method technique is similar, except that the cantilever is driven at a fixed frequency instead of self-resonantly. The amplitude of the tip response is then measured by a lock-in amplifier instead of counting the frequency of oscillations. In the linear response regime, the amplitude depends on the res-

onant frequency only via the transfer function of the cantilever (Eq. 7.5). Shifts in the frequency due to the Coulomb oscillations are thus observed as peaks or dips in the response amplitude⁹. Note that for these measurements, just as for EFM, it is not necessary to measure the Coulomb oscillations in the conductance, nor is it even necessary to have conduction through the nanotube: we just need to be able to change the occupancy of the quantum dot using the tip voltage. Therefore we can once again study nanotubes which are broken or only contacted on one side¹⁰.

A measurement of the frequency shift in the cantilever oscillation, taken when the tip is over the same quantum dot we studied in sections 7.2 and 7.3, is shown in Fig. 7.13. The conductance of the nanotube is also measured simultaneously, to verify the positions of the Coulomb oscillation peaks. Here, we use the amplitude response to a fixed driving frequency to deduce the frequency shift (method (b) in Fig. 7.12). The driving frequency is on resonance at $V_{tip} = -200$ mV. The V_{tip} dependence of the resonant frequency is known from previous measurements (not shown), and the resulting transfer function is plotted as a blue line. We see that the amplitude response of the tip oscillation follows the expected curve everywhere except at the Coulomb oscillations. For V_{tip} below -200 mV (*i.e.* when the cantilever is driven above resonance), the amplitude on the Coulomb peaks decreases from the expected response; for tip voltages above -200 mV (*i.e.* when the cantilever is

9. We can also use the phase of the cantilever response to measure the frequency shifts, but for practical reasons this turns out to be the least convenient method.

10. Note that the nanotube participates in this measurement only passively, unlike the case for EFM. In principle, we therefore do not need to have any electrical contact to the nanotube to make this measurement, as long as the charge has somewhere to go (such as another dot on the nanotube). Measurements of nanotubes that are not electrically contacted have not yet been attempted.

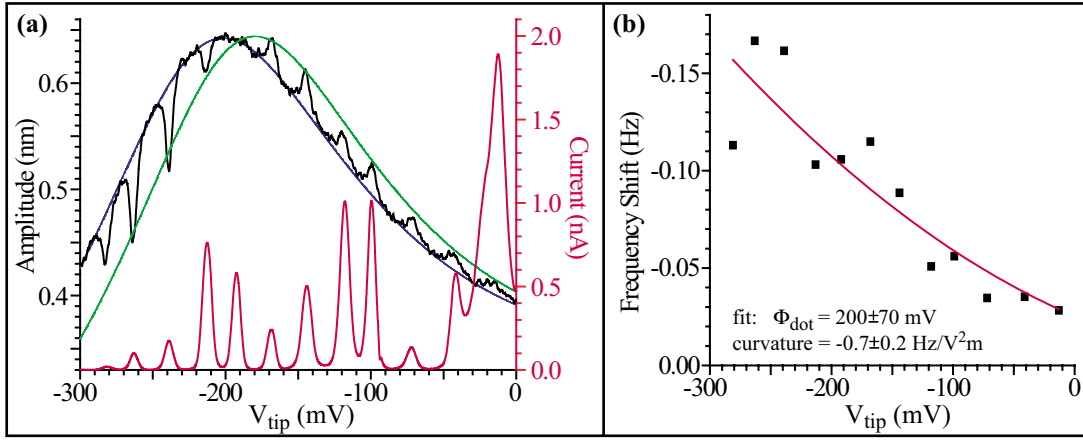


Fig. 7.13: Frequency shift measured from the amplitude response of cantilever to a fixed driving frequency, for quantum dot studied in sections 7.2 and 7.3. **(a)** The amplitude response as a function of V_{tip} is shown in black, the simultaneously-measured conductance is shown in red. There are peaks and dips in the amplitude response at the location of the conductance peaks, due to a reduction of the cantilever resonance frequency at the Coulomb oscillations. This frequency shift at the Coulomb oscillations moves the normal transfer function of the cantilever (shown in blue) to higher V_{tip} (shown in green). **(b)** The shift in frequency at the Coulomb oscillations varies quadratically with tip voltage.

driven below resonance), the amplitude increases from the expected response. The peaks and dips in the amplitude response coincide precisely with the Coulomb oscillations in the conductance.

It is important to note that although Fig. 7.13 looks very similar to Fig. 7.4, showing peaks and dips in the amplitude response of the cantilever at the positions of the Coulomb oscillations in the conductance, the physical meaning of these peaks and dips is quite different. In the EFM measurement of Fig. 7.4, the peaks and dips result from the dot exerting a force on the AFM tip. In Fig. 7.13, we are not directly applying any electrostatic potential to the nanotube: it is grounded. The peaks and dips result from a change in the dynamical properties of the cantilever, *i.e.* its resonance frequency ω_0 .

7.6 Interpretation of Frequency Shift Measurements

We can understand this behaviour in terms of the effect of the motion of the tip on the electrostatic potential of the quantum dot. As the tip oscillates, the voltage on the tip causes the electrostatic potential of the dot to oscillate, too. Away from the Coulomb oscillations, the dot occupancy is fixed, and hence the potential of the dot is insensitive to the tip oscillation, as described in section 7.3. The tip response therefore follows the expected transfer function for the cantilever. At the Coulomb oscillations, however, the potential of the dot is very sensitive to changes in the electrostatic potential felt from the tip (see Fig. 7.6). As the tip approaches the dot during each cycle of oscillation, an electron hops onto the dot and the attractive force between the tip and the dot is increased. This effectively softens the cantilever, reducing the spring constant k and hence ω_0 . In terms of the amplitude response measured in Fig. 7.13, this means that the transfer function shifts to a more positive V_{tip} at the Coulomb oscillations, shown as a green line in the figure.

Expressing this mathematically, we recall that the force on the cantilever has two components, one from the electrodes and one from the quantum dot:

$$F = \frac{1}{2}C'_{el}(V_{tip} - \Phi_{el})^2 + \frac{1}{2}C'_{dot}(V_{tip} - \Phi_{dot})^2 \quad (7.8)$$

The force derivative thus also has two components. The potential of the electrodes does not change as the tip moves, but the potential of the dot does. The force derivative is thus:

$$F' = \left\{ \frac{1}{2}C''_{el}(V_{tip} - \Phi_{el})^2 + \frac{1}{2}C''_{dot}(V_{tip} - \Phi_{dot})^2 \right\} + C'_{dot}(V_{tip} - \Phi_{dot})\frac{\partial\Phi}{\partial z} \quad (7.9)$$

where ϕ is the electrostatic potential of the dot. The terms in the brackets are just the standard force derivative terms that produce a continuous frequency shift quadratic in tip voltage. These are the terms responsible for the V_{tip} dependence of ω_0 that leads to the regular transfer function of the cantilever response (blue line) in Fig. 7.13. The last term, which we will call $\Delta F'$, is the one that is responsible for the additional frequency shift on the Coulomb oscillations. Expanding the dot potential in terms of the continuous charge q induced on the dot by the tip, we obtain:

$$\Delta F' = (C'_{dot} \cdot (V_{tip} - \Phi_{dot}))^2 \frac{\partial \phi}{\partial q} \quad (7.10)$$

As discussed in section 7.3 and shown in Fig. 7.6, $\frac{\partial \phi}{\partial q}$ is highly peaked, having the same shape as the peaks in the conductance. The additional force gradient $\Delta F'$ due to changing the occupancy of the dot thus contributes only on the Coulomb peaks, and Coulomb oscillations in the resonant frequency of the cantilever are observed at the same locations as oscillations in the force on the tip and oscillations in the conductance of the dot.

This model of the frequency shifts due to the Coulomb oscillations can be tested quantitatively by comparison to the data in Fig. 7.13. To calculate the quadratic curvature in V_{tip} of the frequency shifts that is expected from Eq. 7.10, we use the values $C'_{dot} = 2.9 \pm 0.2 \times 10^{-11}$ F/m (determined in Chapter 6) and $\frac{\partial \phi}{\partial q} = 5 \pm 0.5 \times 10^{16}$ V/C (obtained from section 7.3). The expected curvature in the force gradient is then 80 ± 10 $\mu\text{N}/\text{V}^2\text{m}$, producing a frequency shift of -0.5 ± 0.1 Hz/V².

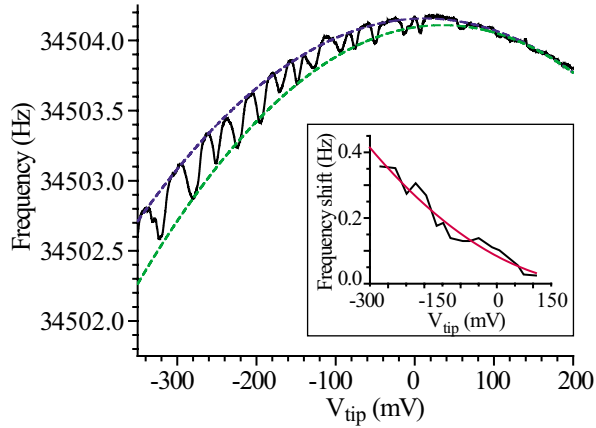


Fig. 7.14: Frequency shift measured by frequency counting above one of the dots in the nanotube imaged in Fig. 7.9. Again, quasi-periodic dips in the frequency are observed. The normal frequency shift due to the dc electrostatic potential difference between the tip and the sample is shown in blue; the enhanced frequency shift at the Coulomb oscillations is shown in green. The inset shows a quadratic fit to the peaks in the frequency shift.

The measured shifts in the resonance frequency are plotted in Fig. 7.13(b), along with a quadratic fit according to Eq. 7.10. We find that the fit produces a frequency shift of $-0.7 \pm 0.2 \text{ Hz/V}^2$, in good agreement with the theoretical value. The contact potential of the dot obtained from the fit is $\Phi_{\text{dot}} = 200 \pm 70 \text{ mV}$, close to the value obtained in section 7.3 ($\Phi_{\text{dot}} = 330 \pm 50 \text{ mV}$). We thus have confidence that Eq. 7.10 correctly describes the frequency shift due to single-electron charging. To show the effect of the change in the force gradient due to the single-electron motion, in Fig. 7.13(a) we plot the amplitude response expected at the Coulomb oscillations as a green line.

We can perform similar measurements on dots in nanotubes which are only contacted on one side. In Fig. 7.14, we measure the frequency shifts from Coulomb oscillations in one of the dots in the nanotube that was measured by EFM in Fig. 7.9, using a frequency counter as described in Fig. 7.12(a). The resonant frequency is plotted as a function of V_{tip} along with a quadratic fit to the Coulomb peaks according to Eq. 7.10. The fit

yields a contact potential $\Phi_{\text{dot}} = 280 \pm 30$ mV, and a frequency shift of -1.0 ± 0.1 Hz/V², about twice the value seen in the other dot (Fig. 7.13).

Our model for the frequency shift successfully describes the shifts in the resonance frequency produced by the Coulomb oscillations. We see that by studying the effects of single-electron motion on the dynamics of the cantilever oscillation, we can measure details of the electrostatics of quantum dots on the nanotubes without even having good electrical contact. In the same way as described for EFM in section 7.3, in principle we can use measurements of these frequency shifts at the Coulomb oscillations to characterise a quantum dot, determining the tip-dot capacitance and capacitance derivative, the contact potential of the dot, the capacitance to the gate, the width of the Coulomb oscillation peaks, and the charging energy. Interestingly, we note that the frequency shift from the dot depends on the dot parameters in a different way than does the force from the dot. Measuring both the frequency shift and the force can therefore be used to check the consistency of the results.

7.7 Q Degradation Measurements

So far, we have seen that the Coulomb oscillations affect the electrostatic force on the AFM tip and the resonant frequency of the AFM cantilever. These are not the only effects of the Coulomb oscillations, however. In particular, we find that often the Q factor of the cantilever resonance is also affected, being reduced on the Coulomb oscillations from its nominal value, sometimes substantially. This effect has been briefly noted in section 7.4, where we presented a survey of EFM images of several nanotubes. We now investigate

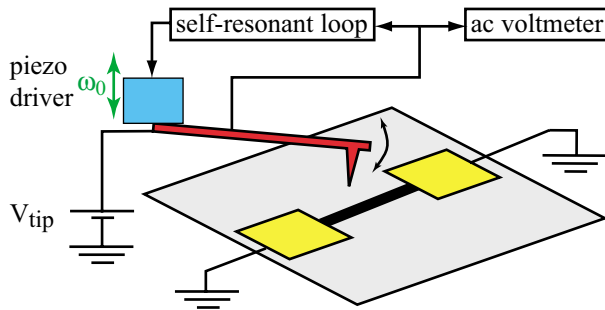


Fig. 7.15: Measuring the Q degradation with scanned dissipation microscopy (SDM). The cantilever is driven into resonance mechanically, using the self-resonant feedback loop so that the oscillation stays on resonance at all times. The amplitude of the oscillation, measured with an ac voltmeter, is then proportional to the Q of the resonance (assuming linear response).

the Q degradation in more detail, presenting measurements on several nanotubes. Because the Q of the resonance measures the energy dissipated by the cantilever motion, we call this measurement technique *scanned dissipation microscopy* (SDM)¹¹.

Conceptually the most straightforward way to image the Q degradation is to measure the Q of the cantilever resonance at each position of the AFM tip by directly measuring the width of the resonance as a function of frequency. Some measurements of the Q have been made in this way, but it is a very cumbersome method. In practice, we most often use a simple shortcut, illustrated in Fig. 7.15. The cantilever is driven mechanically by a self-resonant feedback loop, and the amplitude of the response is measured with an ac voltmeter. Since the oscillation is always on resonance, the response amplitude in the linear regime is just $z = (F_{drive}/k)Q$. The driving force F_{drive} is fixed and k changes by only very small amounts (as seen in the previous section), hence variations in the amplitude of the oscillation are due principally to variations in the Q of the oscillation. Note that this method for measuring the Q degradation assumes that the cantilever oscillation is always in the lin-

¹¹.A similar technique has been used previously to measure dissipation in magnetic systems (Grutter 1997) and doped semiconductors (Stowe 1999).

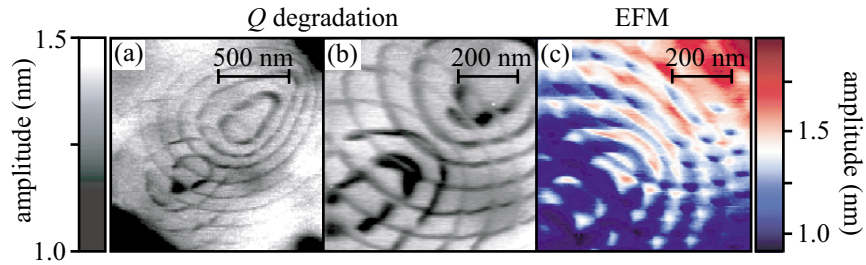


Fig. 7.16: Scanned dissipation images of semiconducting nanotube imaged by EFM in Fig. 7.8. $T=600$ mK, $z=100$ nm. (a),(b) SDM images shows concentric rings of strong Q degradation (dark areas) around the two dots known to be in this nanotube. The maximum Q degradation is $\sim 35\%$ of the normal Q . $V_{tip}=-300$ mV in (a), -400 mV in (b). (c) EFM image of the same area as (b) taken under the same conditions. The rings of Q degradation occur at precisely the same locations as the peaks in the force, indicating that they arise from single-electron charging effects.

ear response regime. Deviations from linear response will appear as changes in the Q . Empirically, we find that when the cantilever amplitude is ~ 1 nm, it is close to the onset of non-linear behaviour at typical tip voltages. Artifacts from non-linearities are thus sometimes observed¹².

A scanned dissipation measurement of the $1.5 \mu\text{m}$ long semiconducting nanotube that is imaged by EFM in Fig. 7.8 is shown in Fig. 7.16. In these images we plot the amplitude response of the cantilever to the mechanical driving force, so that locations where the amplitude is diminished by Q degradation show up as dark areas. In Figs. 7.16(a) we observe two sets of concentric rings centered at different locations along the nanotube where the Q is strongly degraded. These rings of Q degradation occur at exactly the same spots as the force peaks in the EFM signal, as can be seen by comparing the Q degradation image in Fig. 7.16(b) to the EFM image in Fig. 7.16(c). The Q is thus being decreased at

12. As an example, the Q appears to be degraded over the contacts in all the Q degradation measurements. This is because the contacts are tall and hence the tip is much closer to the surface, increasing the nonlinearity of the oscillation.

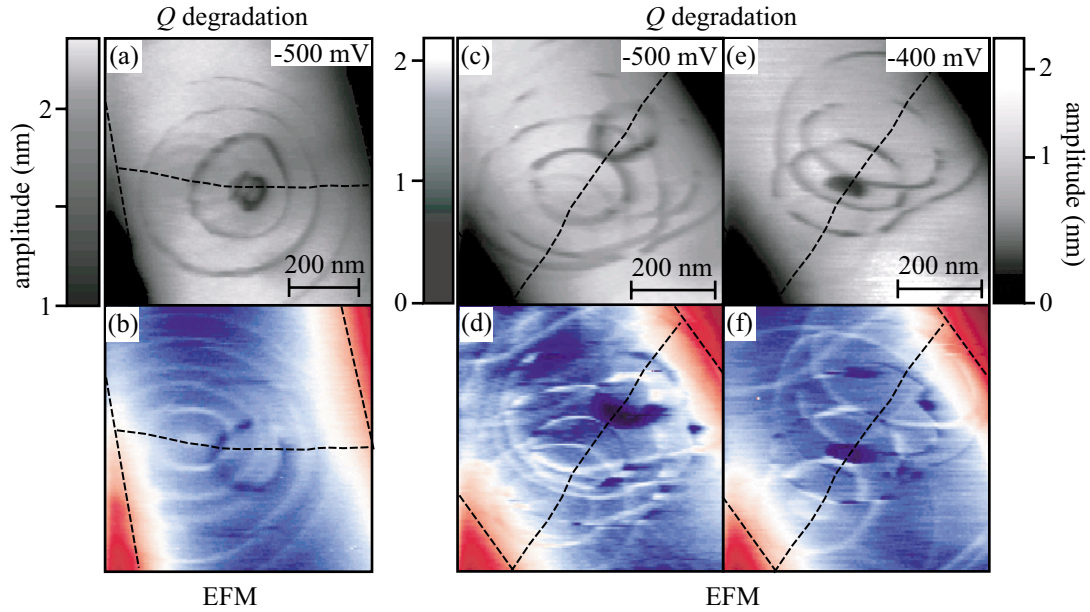


Fig. 7.17: Variation in Q degradation on different dots. $T=600$ mK. (a) SDM image of the nanotube measured by EFM in Fig. 7.10. The EFM image is repeated in (b) for ease of comparison. There are two dots seen in the EFM image, but only the dot on the right has a sizable ($\sim 50\%$) Q degradation at the Coulomb oscillations. The SDM signal from the dot on the left is barely detectable. The rings in the SDM and EFM images do not align precisely because the images were taken at different tip heights. (c)-(f) SDM and EFM images of the nanotube measured in Fig. 7.11. The dots in the lower left show a small Q degradation, while the dots in the upper right show a large ($\sim 30\text{-}40\%$) degradation. V_{iip} indicated on images.

the Coulomb oscillations by some dissipation process. Measuring the magnitude of the amplitude decrease on the Coulomb oscillations, we find that at the maxima of the Coulomb oscillations the Q decreases by as much as 35% from its normal value Q_0 , *i.e.* to as little as $0.65Q_0$.

In these images we can see that the Q degradation is about the same for both quantum dots on the nanotube. Measurements on other nanotubes, however, show that the Q degradation can vary significantly from one dot to the next. In Fig. 7.17 we show images of the Q degradation around the nanotubes that were imaged by EFM in Figs. 7.10 and 7.11. For ease of comparison, the EFM images are shown here once again. In Fig. 7.17(a), we

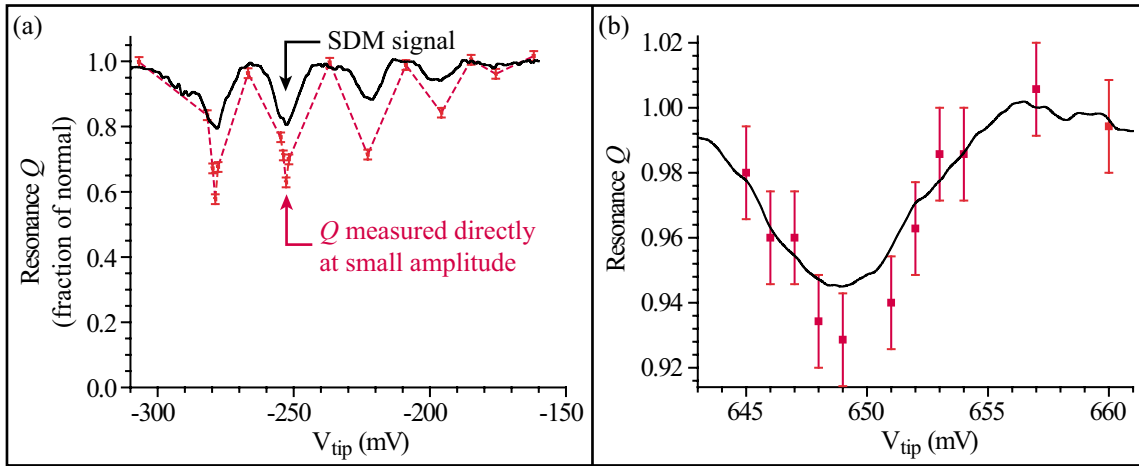


Fig. 7.18: Comparison of Q inferred from SDM to Q measured directly. **(a)** The resonance Q as a function of V_{tip} inferred from an SDM measurement over a single quantum dot is plotted as a fraction of its normal value (black line). At various V_{tip} , Q is measured directly from the width of the resonance in frequency (red squares, dotted red line). The changes in Q inferred from SDM correspond to actual decreases in the measured Q . The SDM measurement underestimates the true Q reduction because of the large tip oscillation used. **(b)** Resonance Q near a single Coulomb oscillation at another dot. The Q inferred from SDM follows the measured Q (red squares) along the profile of the peak. SDM gives a better measure of the true Q reduction here because the tip oscillation amplitude is smaller.

see that the Q degradation for Coulomb oscillations around the right-hand dot is very strong, as much as 50% of Q_0 , but around the left-hand dot it is only just barely visible. Similarly, in the images of the other nanotube (Figs. 7.17(c) to (f)), the dots that have Coulomb oscillations in the lower left corner of the EFM images do not show much Q degradation. The dots in the upper right corner, on the other hand, do show a significant decrease of Q at the Coulomb oscillations: in Fig. 7.17(c) Q falls as low as $0.7Q_0$, while in Fig. 7.17(e) it falls as low as $0.6Q_0$.

In the scanned dissipation measurements presented above, we have assumed that the reductions in the amplitude response are due only to reductions in Q . We now check this assumption by comparing the putative Q obtained from an SDM measurement to the Q obtained from a direct measurement of the width of the resonance. We first fix the position

of the tip over a quantum dot with a strong SDM signal and measure the amplitude response of the cantilever as a function of V_{tip} . We then measure the resonance curve of the cantilever at various values of V_{tip} and extract the Q factor directly from the height:width ratio of the resonance as a function of frequency. The result is plotted in Fig. 7.18 for two different quantum dots. The SDM amplitude signal is shown as black, while the directly measured Q is shown as red squares. Both are plotted as a fraction of the Q away from a Coulomb oscillation.

It is clear from Fig. 7.18 that the decrease observed in the amplitude of the cantilever oscillation is indeed due to a decrease in the Q of the resonance. In Fig. 7.18(a), several Coulomb oscillations with different amounts of reduction in the SDM signal are shown. At each peak in the SDM signal, the Q of the resonance is reduced from its normal value: small SDM peaks correspond to small reductions in Q , while large SDM peaks correspond to large reductions in Q . The main difference between the measurements is that SDM actually understates the true reduction in Q , by as much as 50%. This is due to the large oscillation amplitude used in the measurement, ~ 1.5 nm, which is into the regime where the tip motion widens the Coulomb oscillation peaks (see Fig. 6.7) as well as the regime where the cantilever motion is non-linear.

The correspondence between the SDM signal and the Q degradation is confirmed by a more detailed measurement of Q along the profile of a single SDM peak at a different dot (Fig. 7.18(b)). Here we see that the Q inferred from the SDM measurement very closely

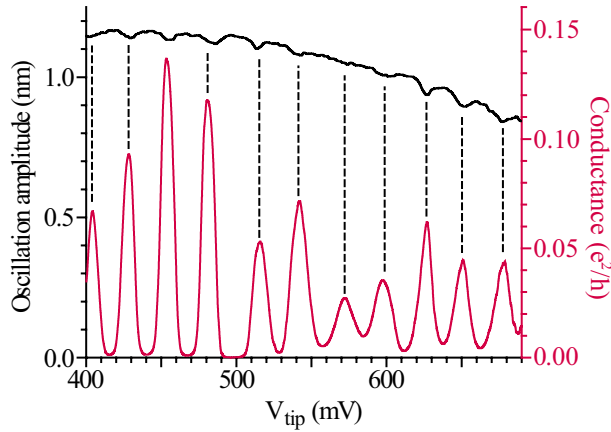


Fig. 7.19: SDM measurement of the quantum dot studied in sections 7.2-7.3. The SDM signal is shown in black, the conductance is shown in red. The peaks in the Q degradation occur at the same location as the peaks in the conductance. The Q degradation in this dot is much smaller than the dots measured earlier, only $\sim 2\text{-}3\%$. There is no obvious correlation between the height of the conductance peaks and the amount of Q degradation in this dot.

follows the actual Q of the cantilever resonance, all along the peak. Once again, the main difference is that the Q degradation measured by SDM is reduced due to the large cantilever oscillation amplitude¹³. Note that the agreement between the SDM measurement and the actual Q is much closer in Fig. 7.18(b) than in Fig. 7.18(a), due to the use of a smaller oscillation amplitude in the SDM measurement.

The final aspect of the Q degradation we investigate is its dependence on the sample conductance. To do this, we return to the nanotube studied in sections 7.2 and 7.3. In Fig. 7.19 we plot the scanned dissipation signal measured as a function of V_{tip} when the tip is over the quantum dot on the right side of the nanotube (the same dot studied in sections 7.2 and 7.3). The conductance of the nanotube is measured simultaneously. There are several notable features in this figure. First, we confirm that the peaks in the Q degradation do indeed line up with the peaks in the conductance, as expected. Additionally, we see that

13. Shifts in the phase of the cantilever response on resonance can also cause the oscillation amplitude to decrease.

When this is checked it is found not to occur, except for nonlinear cantilever oscillations. In that case, the phase of the amplitude response on resonance changes, and the phase contributes a small amount of the SDM signal.

the magnitude of the Q degradation at this dot is much smaller than at the dots measured earlier. Here, the typical Q degradation is $\sim 2\text{-}3\%$, compared to as much as 50% seen previously. Finally, although there is some variation from one Coulomb oscillation to the next in both the height of the conductance peaks and the magnitude of the Q degradation, we do not find any obvious correlation between the two in this dot.

7.8 Interpretation of Q Degradation Measurements

In order to understand the physical origin of the Q degradation, we recall that the Q -factor of the resonance describes the energy dissipated by the cantilever motion. More precisely, the Q is defined as the ratio of the energy stored in the cantilever oscillation to the energy dissipated in one cycle of oscillation. Any decrease in Q must thus be due to some process causing additional dissipation of energy from the cantilever. Note that the additional energy dissipation that we are measuring here is really very small. For a typical cantilever oscillation amplitude δz of 1 nm, the energy stored in the cantilever is $(1/2)k\delta z^2 \sim 1.5$ aJ. With a normal Q of ~ 30000 and frequency of ~ 30 kHz, the power dissipated naturally in the cantilever is 1.5 aW. When we measure a 2% degradation of the Q , as in Fig. 7.19, we are therefore measuring an additional power dissipation of only 3×10^{-20} W.

To understand the source of this additional energy dissipation, we note that the Q degradation observed in the SDM measurements occurs only at the Coulomb oscillations, where the charge state of the quantum dot changes by 1. The additional energy dissipation causing the Q degradation is therefore clearly related to single-electron motion in the quan-

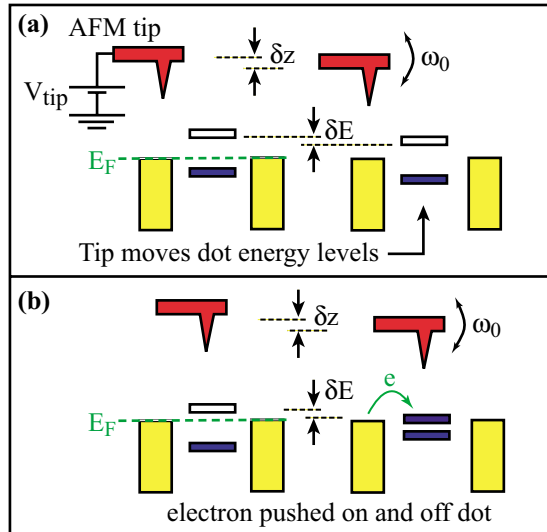


Fig. 7.20: Degradation of cantilever Q due to energy dissipated by single-electron motion. **(a)** The motion of the tip causes an oscillation δE of the electrochemical potential of the quantum dot with respect to the Fermi level of the contacts. In the Coulomb blockade regime, there is no motion of charge on/off the dot. **(b)** When the dot potential is near E_F , δE causes a single electron to jump on and off the dot once per cycle of tip motion. The resulting current flow that is pushed by the tip dissipates energy from the cantilever, reducing the Q .

tum dot. It is natural to attribute this energy dissipation to the energy dissipated by the electrons as they move on and off the dot under the influence of the AFM tip motion.

The basic picture is illustrated in Fig. 7.20. The voltage on the tip changes the electrostatic potential and hence the electrochemical potential of the dot, so that the tip oscillation causes an oscillation of the dot potential. When the dot potential is in the Coulomb blockade regime, the oscillation of the dot potential does not change the charge on the dot and there is no current flow between the electrodes and the dot. Thus there is no energy dissipation in the dot, and the cantilever Q has its normal value. When the dot potential is near the Fermi level E_F of the electrodes, however, the oscillation of the dot potential causes an electron to hop on and off the dot once each cycle. This current flows across the resistive barrier between the electrodes and the dot dissipates energy. Since the current is being pushed by the AFM tip, the energy dissipated comes from the energy of the cantilever oscillation, degrading the Q .

We can calculate the energy dissipation expected in this picture from simple physical considerations. For small tip oscillations $\delta z(t) = \delta z \cos(\omega t)$, the change in the electrochemical potential of the dot E due to the effect of the tip is given by:

$$E(t) = E + \delta E(t) \sim \frac{C}{C_{tot}} e\Delta V + \left(\frac{C'}{C_{tot}} e\Delta V \right) \delta z(t) \quad (7.11)$$

Here C is the tip-dot capacitance, C_{tot} is the total capacitance of the dot, and $\Delta V = V_{tip} - \Phi$ is the net dc voltage between tip and dot. The first term in this equation represents the dc electrochemical potential change due to the tip voltage, and the second term the ac change due to the oscillation of the tip. This ac change in the electrochemical potential of the dot causes a current I to flow on and off the dot, dissipating an rms power $P = (1/2)I^2/G$, where G is the conductance.

To determine the current flow caused by the tip motion, consider for simplicity the case of an electron moving back and forth from an electrode to a single energy level on the quantum dot. Then, we know that the additional charge on the dot, eN , is given by $eN = ef(E - E_F)$, where $f(E)$ is the Fermi distribution function: $f(E) = \left(1 + \exp\left(\frac{E}{k_B T}\right) \right)^{-1}$.

The current flow in this model is therefore:

$$I = \frac{edN}{dt} = -ef'(E - E_F) \cdot \frac{dE}{dt}$$

$$\therefore I \sim -ef'(E - E_F) \cdot \omega \delta E \quad (7.12)$$

Here $f'(E - E_F)$ is the derivative of the Fermi distribution function, which is highly peaked at E_F . The conductance G can also be expressed in terms of the Fermi distribution function:

$G = -G_{max}(4k_B T)f'(E - E_F)$, where G_{max} is the height of the conductance peak (Grabert 1992). The power P dissipated by the current I is thus:

$$P = \frac{1}{2}(I^2/G) \sim \frac{1}{2} \frac{(e\omega)^2}{G_{max}} \cdot \left(\frac{\delta E}{k_B T}\right)^2 \cdot [-k_B T f'(E - E_F)] \quad (7.13)$$

Note that this result is derived in the limit of small excursions of the tip, $\delta E \ll k_B T$, and tip oscillation frequencies ω much lower than the tunnelling rate¹⁴.

This expression captures the essential physics of the energy dissipation. The first term expresses the power dissipation we would expect for a charge e moving moving back and forth at a frequency ω with a conductance G_{max} . This represents the maximum power that can be dissipated from single-electron motion. The second term expresses in some sense the amount of charge that moves for a given tip amplitude. Finally, the last term accounts for the fact that charge only moves when the dot is not blockaded, so that all the power is concentrated at the Coulomb oscillation. It is this last term that ensures that the lineshape of the Q dissipation will be highly peaked at the Coulomb oscillations.

From Eq. 7.13 we can calculate the peak power dissipation expected at the Coulomb oscillations due to single-electron motion:

$$P_{max} \sim \frac{1}{8} \cdot \frac{(e\omega)^2}{G_{max}} \cdot \left(\frac{C'}{C_{tot}} \frac{e\Delta V}{k_B T}\right)^2 \delta z^2 \quad (7.14)$$

14. Note that there are some subtleties involved with the definition of the conductance used in Eq. 7.13. We have written it in terms of the measured conductance peak G_{max} . A more precise calculation would express the power in terms of an effective conductance for hopping off the dot to either of the contacts. This may differ by from the measured conductance by some prefactor. For the purposes of an order of magnitude calculation as presented here, we simply approximate the effective conductance by G_{max} .

Since we measure the resonance Q rather than the power, we want to calculate the change in Q caused by this power dissipation. The Q is expressed in terms of the total power P_{tot} as $Q = \left(\frac{1}{4\pi}\right) \frac{\omega k \delta z^2}{P_{tot}}$. If the cantilever has a natural Q of Q_0 due to a power dissipation P_0 , then $P_{tot} = P_0 + P_{max}$, and the Q measured at the dissipation peak is given by:

$$\frac{1}{Q} = \frac{1}{Q_0} + \Delta\left(\frac{1}{Q}\right) \quad (7.15)$$

$$\Delta\left(\frac{1}{Q}\right) = \left(\frac{\pi}{2}\right) \frac{e^2 \omega}{k G_{max}} \cdot \left(\frac{C'}{C_{tot}} \frac{e \Delta V}{k_B T}\right)^2 \quad (7.16)$$

Eqs. 7.15 and 7.16 thus describes the Q degradation signal we expect to observe due to single-electron motion in the quantum dot.

To see if this result is reasonable, we investigate what peak conductance would be needed to produce a Q degradation on the order of 50%, the largest observed in the images shown in the previous section. Using typical values for the parameters in Eq. 7.16 ($k = 3$ N/m, $\omega = 2 \times 10^5$ s⁻¹, $k_B T = 0.05$ meV, $e \Delta V \sim 0.5$ V, $C' \sim 3 \times 10^{-11}$ F/m, $C \sim 8 \times 10^{-17}$ F), we find as an order-of-magnitude estimate that $Q \sim (1/2)Q_0$ for $G_{max} \sim 2 \times 10^{-9}$ S (*i.e.* a dot resistance of ~ 500 M Ω). This is a low conductance, but it is certainly within the range of values that has been observed for such quantum dots.

From this estimate we can now understand why the Q degradation signal is so small in Fig. 7.19: it's because the conductance of the dot being measured is so high. Since we know the conductance of this dot, we can attempt to get quantitative agreement between the measured Q degradation and the Q degradation expected from Eq. 7.16. The peak conduct-

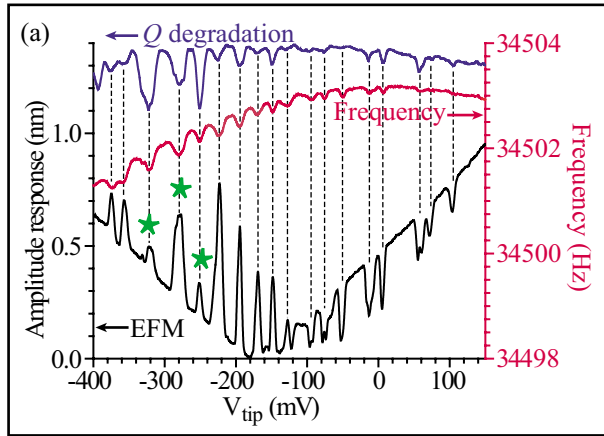


Fig. 7.21: Measurements of the EFM signal (black), frequency shift (red), and Q degradation (blue) as a function of V_{tip} for the same dot. All three effects occur simultaneously. Large peaks in the Q degradation affect the amplitude response at the Coulomb oscillations. In the EFM measurement, this depresses the height of the single-electron force peak (green stars).

ance of this dot is $G_{max} \sim 0.1 e^2/h \sim 3 \times 10^{-6} \text{ S}$. Using the same parameter values as previously, we predict a Q degradation of $\sim 0.05\%$. This is about 50 times smaller than what we actually observe in Fig. 7.19. The origin of this discrepancy is not clear. It would be instructive to measure the Q degradation as a function of the conductance in very resistive devices, to develop a better quantitative understanding of this effect.

As a concluding remark, we note that the degradation of the Q at the Coulomb oscillations can have a noticeable effect on the other types of measurements we have studied in this chapter that rely on measuring the amplitude of the cantilever response. Changes in the Q change the amplitude response of the cantilever to the driving forces, masking the “true” signal that we are trying to measure. For example, the height of the single-electron EFM signal from a quantum dot will be reduced by any degradation of the Q . For dots with small Q degradation, such as the dot studied in sections 7.2 and 7.3, we can safely ignore the effect that changes in the Q have on the EFM response. When the Q degradation is large, however, this is definitely not the case. This is illustrated in Fig. 7.21, where we

show the EFM signal and the SDM signal as a function of V_{tip} on the same graph. We have marked with a green star several Coulomb oscillations on this dot that have a large Q degradation. We can clearly see that the peaks in the EFM signal at these particular Coulomb oscillations are suppressed compared to their neighbours, in some cases substantially so. Care must therefore be taken when analysing EFM measurements to ensure that the effects being observed are truly due to the electrostatic force, and not just changes in the Q of the resonance.

7.9 Summary

In this chapter we have used an AFM to sense single-electron motion on quantum dots in a carbon nanotube in several different ways. We first measure the force from a single electron jumping on and off a quantum dot by using electrostatic force microscopy. We observe clear peaks in the force whenever there are peaks in the conductance, allowing us to image Coulomb oscillations in the force exerted by the quantum dot. We obtain quantitative agreement between the measured force and the force expected from single-electron motion. In addition to creating peaks in the force on the AFM tip, we find that single-electron charging creates peaks in the frequency shift of the cantilever resonance. This provides us with a second method for sensing the motion of single electrons on and off the quantum dot. The frequency shift we measure agrees quantitatively with the shift expected due to single-electron charging of the dot. Finally, we find that single-electron motion also changes the Q -factor of the cantilever resonance, so that we can image Coulomb oscilla-

tions through their effect on the energy dissipation in the cantilever. We obtain qualitative agreement between the observed Q degradation and the energy dissipation expected from single-electron motion on the quantum dot.

What we have measured in this chapter are the effects from a single electron moving on and off a quantum dot. Needless to say, these effects are very small: the typical force from single-electron motion is only about 10^{-14} N, the typical shift in the resonance frequency about 1 part in 10^6 , and the typical power dissipation about 10^{-19} W. The fact that we can see these effects is a testament to the exquisite sensitivity of the AFM, proving once again its power as a tool for studying the microscopic properties of low-dimensional systems.

8.1 Summary

In this thesis, we have explored the local electronic properties of low-dimensional systems using scanned probe microscopy. Specifically, we have used a low-temperature atomic force microscope sensitive to electrostatic forces to study two particular systems: two-dimensional electron gases in the quantum Hall regime, and carbon nanotubes.

In the quantum Hall regime, we investigated the properties of non-equilibrium edge state populations in a quantum Hall conductor. We first used electrostatic force microscopy to measure the local Hall voltage distribution associated with disequilibrated edge states. As expected, we observed a sharp Hall voltage gradient across the incompressible strip at the sample edge, which could be eliminated by deliberately equilibrating the edge state populations. We also measured the local rate at which equilibration occurred.

We next used scanned gate microscopy to study in more detail the inter edge state scattering responsible for the equilibration of the edge state potentials. We found that scattering between the edge states was dominated by a small number of strong, discrete scattering centers that were well separated along the edge of the sample. Investigating the nature of the individual scattering centers by looking at the tip voltage dependence of the

scattering, we discovered two types of scattering centers: weak links in the incompressible strip between the edge states, and microscopic impurities near the edge.

Turning to one-dimensional electrons, we investigated the local properties of carbon nanotubes in the single-electron regime. Scanned gate measurements provided images of Coulomb oscillations in the conductance due to quantum dots that formed in the nanotube. We used these measurements to characterise a quantum dot and its interaction with the AFM tip. We found that the electrostatic environment of the quantum dot played a very important role in determining the structure of the scanned gate images. We modeled the scanned gate measurements phenomenologically to take into account the effects of fixed charges on the sample surface as well as screening of contact potential differences by the AFM tip.

Finally, we performed single-electron force measurements on carbon nanotubes. We measured peaks in the force exerted on the AFM tip at the locations of the Coulomb oscillations in the conductance. We also measured peaks in the resonance frequency of the AFM cantilever at the Coulomb oscillations in the conductance. In both cases, quantitative agreement was found with the force and force derivative expected from the abrupt change in the electrostatic potential of the quantum dot due to single-electron motion. Both of these measurements were found to provide another way of characterising the properties of the quantum dots on the nanotubes, with the advantage that good electrical contact needed to be made only to one side of the nanotube. Lastly, we observed a reduction of the Q -factor of the cantilever resonance at the Coulomb oscillations. We attributed

this to the energy dissipated by the single-electron motion on the dot, obtaining qualitative agreement with the measurements.

8.2 Future Directions

The success of the scanned probe studies of low-dimensional systems presented in this thesis suggests many avenues for future research. Some of these are questions raised by this work that remain to be answered, while others involve different phenomena about which much could be learned using scanned probe techniques.

Looking first at 2DEG systems, one interesting question raised by the work on edge state equilibration in Chapter 3 and 4 is the correlation between the local rate of equilibration of the edge state potentials and the location of the individual scattering centers. We were able to measure the local equilibration rate with EFM and locate the scattering centers with SGM, but we were not able to correlate the two, possibly because the scattering rate was too high. It would be interesting to repeat the experiment on a sample with much higher mobility (*i.e.* much lower scattering rate), so that we could study scattering sites that are isolated by much longer distances and observe how the local equilibration of the edge state potentials evolves around a single site. It would also be interesting to look at scattering between spin-polarised edge states, to see if the different momentum conservation considerations give rise to different types of scattering centers.

Looking next at carbon nanotubes, more study of the Q degradation at the Coulomb oscillations would be helpful. The energy dissipated by the single-electron motion

on and off a quantum dot does not appear to be sufficient to account for all the energy dissipation observed in the measurement, at least for the nanotube we analysed quantitatively here. Further studies of nanotubes with low conductance would be helpful in developing a better understanding of this phenomenon. It would be especially nice to measure the Q degradation from a semiconducting nanotube while changing the conductance with the backgate. Armed with a quantitative understanding of the scanned dissipation measurement, we could then use it to study dissipation not just in carbon nanotubes, but also in a variety of other resistive systems. In particular, scanned dissipation measurements of DNA might prove very interesting.

Several other aspects of carbon nanotubes would provide fruitful avenues of research. For instance, in nanotubes with several quantum dots, sometimes dots can be made to merge using the backgate or AFM tip voltages. Such behaviour was observed in a few measurements (not reported in this thesis), but it was not explored in any depth. It would be interesting to study this in more detail, especially in semiconducting nanotubes where the conductance can be changed significantly. Another interesting experiment would be to look for Fabry-Perot-type interference effects using scanned gate measurements, as were recently observed in 2DEG systems (Topinka 2001). Yet another avenue of research would be to investigate the properties of nanotubes when they are suspended above the surface of the substrate, so that interactions with the substrate are much reduced.

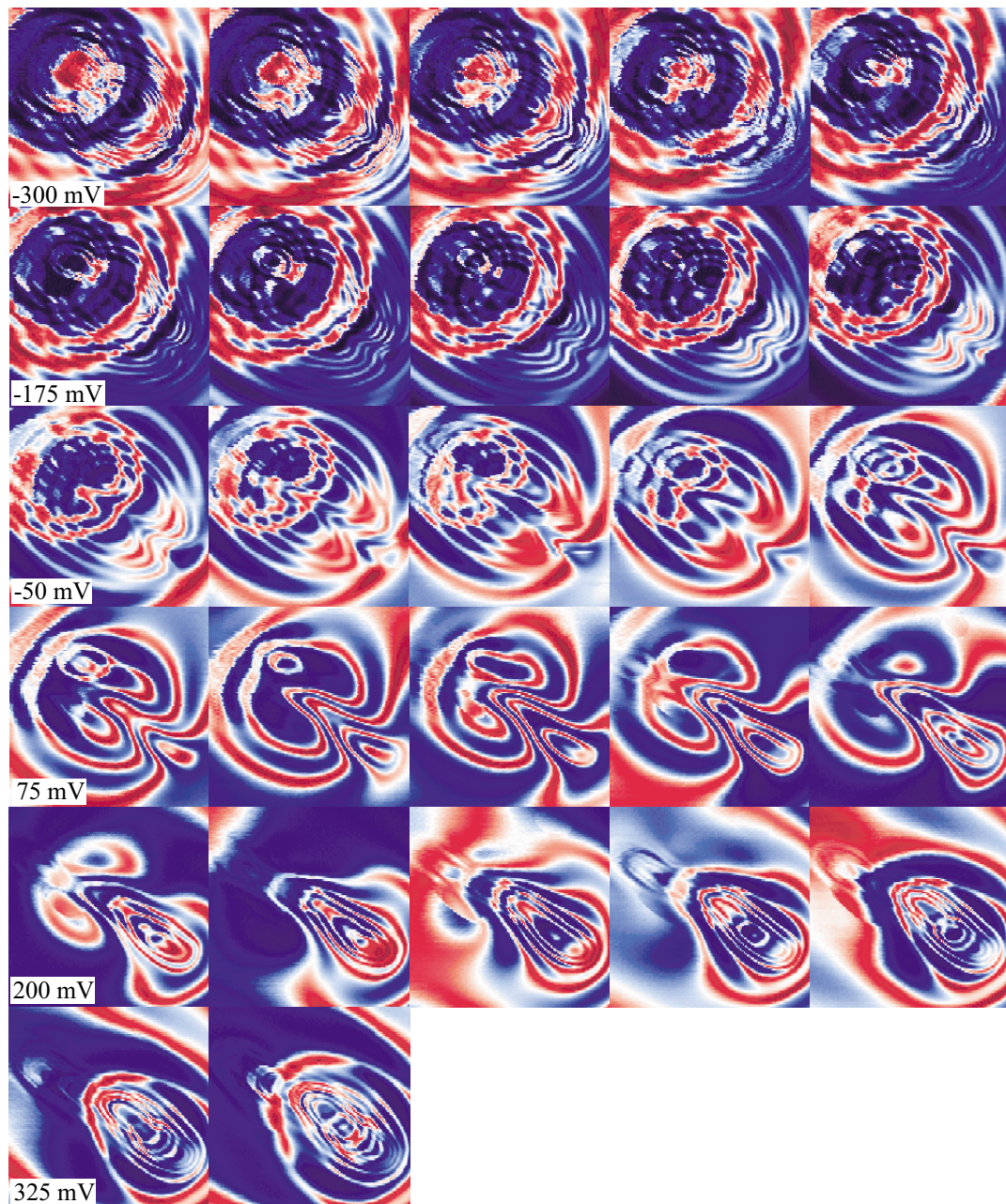
8.3 Concluding Remarks

The work in this thesis demonstrates that scanned probe microscopy provides a powerful tool for exploring the local electronic properties of low-dimensional systems. Given the versatility of scanned probe techniques, and the novel techniques and applications that continue to be developed, it is clear that scanned probe measurements will continue to be a source of important discoveries in the years ahead.

Appendix

A.1 Scanned Gate Movie: Fig. 6.8

Frames spaced by 25 mV:

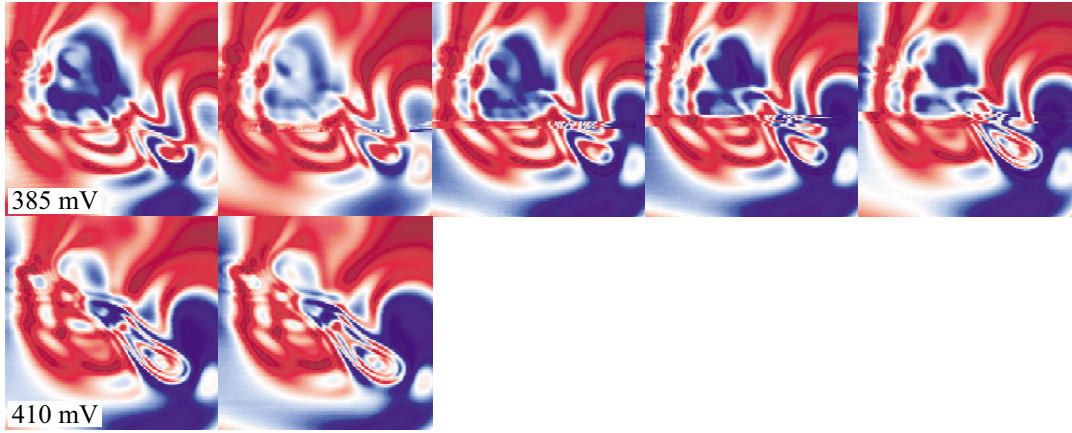


A.2 Scanned Gate Movie: Fig. 6.10

Frames spaced by 5 mV:







References

- Acremann Y., T. Heinzel, K. Ensslin *et al.*, Phys. Rev. B **59**, 2116 (1999).
- Albrecht T. R., P. Grutter, D. Horne *et al.*, Journal of Applied Physics **69**, 668 (1991).
- Alphenaar B. W., P. L. McEuen, R. G. Wheeler *et al.*, Phys. Rev. Lett. **64**, 677 (1990).
- Alphenaar B. W., P. L. McEuen, and R. G. Wheeler, Physica B **175**, 235 (1991).
- Aschcroft N. W. and N. D. Mermin, *Solid State Physics*. Fort Worth: Saunders College Publishing (1976).
- Bachtold A., M. S. Fuhrer, S. Plyasunov *et al.*, Phys. Rev. Lett. **84**, 6082 (2000).
- Badalian S. M., Y. B. Levinson, and D. L. Maslov, JETP Lett. **53**, 619 (1991).
- Bastard G., J. A. Brum, and R. Ferreira, Solid State Physics **44**, 229 (1991).
- Beenakker C. W. J., Phys. Rev. Lett. **64**, 216 (1990).
- Beenakker C. W. J. and H. van Houten, Solid State Physics **44**, 1 (1991).
- Belaidi S., P. Girard, and G. Leveque, Journal of Applied Physics **81**, 1023 (1997).
- Besocke K., in *Proc. STM '86: First International Conference on Scanning Tunneling Microscopy*, Santiago de Compostela, Spain, **181**, 145 (1986).
- Binnig G., C. F. Quate, and C. Gerber, Phys. Rev. Lett. **56**, 930 (1986).
- Bockrath M., D. H. Cobden, P. L. McEuen *et al.*, Science **275**, 1922 (1997).
- Bockrath M., W. J. Liang, D. Bozovic *et al.*, Science **291**, 283 (2001).
- Bozovic D., M. Bockrath, J. H. Hafner *et al.*, Appl. Phys. Lett. **78**, 3693 (2001).
- Büttiker M., Phys. Rev. Lett. **57**, 1761 (1986).
- Büttiker M., Phys. Rev. B **38**, 9375 (1988).

- Chang A. M., Solid State Comm. **74**, 871 (1990).
- Chen L. H., M. A. Topinka, B. J. LeRoy *et al.*, Appl. Phys. Lett. **79**, 1202 (2001).
- Chklovskii D. B., B. I. Shlovskii, and L. I. Glazman, Phys. Rev. B **46**, 4026 (1992).
- Cobden D. H., C. H. W. Barnes, and C. J. B. Ford, Phys. Rev. Lett. **82**, 4695 (1999).
- Collins P. G., K. Bradley, M. Ishigami, and A. Zettl, Science **287**, 1801 (2000).
- Crook R., C. G. Smith, M. Y. Simmons, and D. A. Ritchie, J. Phys. C **12**, L167 (2000).
- Das Sarma S., and A. Pinczuk, eds., *Perspectives on the Quantum Hall Effects*. New York: Wiley Interscience (1997).
- Datta S., *Electronic Transport in Mesoscopic Systems*. Cambridge: Cambridge University Press (1995).
- Dekker C., Physics Today **52**, 22 (1999).
- Dresselhaus M. S., G. Dresselhaus, and P. C. Eklund, *Science of Fullerenes and Carbon Nanotubes*. San Diego: Academic Press (1996).
- Drude P., Annalen der Physik **1**, 566 (1900a).
- Drude P., Annalen der Physik **3**, 369 (1900b).
- Ebbesen T. W. ed., *Carbon Nanotubes: Preparation and Properties*. Boca Raton: CRC Press (1997).
- Eriksson M. A., R. G. Beck, M. Topinka *et al.*, Appl. Phys. Lett. **69**, 671 (1996).
- Finkelstein G., P. I. Glicofridis, R. C. Ashoori *et al.*, Science **289**, 90 (2000).
- Gelfand B. Y. and Halperin B. I., Phys. Rev. B **49**, 1862 (1994).
- Goldhaber-Gordon D., H. Shtrikman, D. Mahalu *et al.*, Nature **391**, 156 (1998).
- Grabert H. and M. H. Devoret, eds., *Single Charge Tunneling*. New York: Plenum Press (1992).

- Grutter P., Y. Liu, P. LeBlanc, and U. Durig, *Appl. Phys. Lett.* **71**, 279 (1997).
- Hafner J. H., M. J. Bronikowski, B. R. Azamian *et al.*, *Chem. Phys. Lett.* **296**, 195 (1998).
- Hafner J. H. C. L. Cheung, T. H. Oosterkamp *et al.*, *J. Phys. Chem. B* **105**, 743 (2001).
- Halperin B. I., *Phys. Rev. B* **25**, 2185 (1982).
- Hall E. H., *American Journal of Science* **119**, 200 (1880).
- Hamada N., S. Sawada, and A. Oshiyama, *Phys. Rev. Lett.* **68**, 1579 (1992).
- van Haren R. J. F., F. A. P. Blom, W. de Lange, and J. H. Wolter, *Phys. Rev. B* **47**, 15700 (1993).
- van Haren R. J. F., F. A. P. Blom, and J. H. Wolter, *Phys. Rev. Lett.* **74**, 1198 (1995).
- Haug R. J., *Semicond. Sci. Tech.* **8**, 131 (1993a).
- Haug R. J., A. D. Wieck, K. von Klitzing *et al.*, *Physica B* **184**, 192 (1993b).
- Iijima S., *Nature* **354**, 56 (1991).
- Imry Y., *Introduction to Mesoscopic Physics* (Oxford University Press, New York, 1997).
- Israelachvili J. N., *Intermolecular and Surface Forces* (Academic Press London, London, 1992).
- Jackson J. D., *Classical Electrodynamics* (Wiley, New York, 1975).
- Jain J. K. and S. A. Kivelson, *Phys. Rev. Lett.* **60**, 1542 (1988).
- Kane B. E., D. C. Tsui, and G. Weimann, *Phys. Rev. Lett.* **59**, 1353 (1987).
- Kastner M., *Physics Today*, **46**, 24 (1993).
- Kim P. and C. M. Lieber, *Science* **286**, 2148 (1999).
- Kittel C., *Introduction to Solid State Physics*. New York: John Wiley & Sons, Inc. (1986).
- von Klitzing K., G. Dorda, and M. Pepper, *Phys. Rev. Lett.* **45**, 494 (1980).

- Komiyama S. H. Hirai, M. Ohsawa *et al.*, Phys. Rev. B **45**, 11085 (1992).
- Komiyama S., H. Hirai, S. Sasa *et al.*, Phys. Rev. B **40**, 12566 (1989).
- Kong J., H. T. Soh, A. M. Cassell *et al.*, Nature **395**, 878 (1998).
- Kong J., N. R. Franklin, C. Zhou, *et al.*, Science **287**, 622 (2000).
- Kouwenhoven L. P., T. H. Oosterkamp, M. W. S. Danoesastro *et al.*, Science **278**, 1788 (1997).
- Kravchenko S. V., D. Simonian, M. P. Sarachik *et al.*, Phys. Rev. Lett. **77**, 938 (1996).
- Landauer R., IBM Journal of Research and Development **1**, 223 (1957).
- Larkin I. A. and J. D. Davies, Phys. Rev. B **52**, 5535 (1995).
- LeMay S. G., J. W. Janssen, M. van den Hout *et al.*, Nature **412**, 617 (2001).
- Lide D., ed., *CRC Handbook of Chemistry and Physics*. Boca Raton: CRC Press (1990).
- Lilly M. P., K. B. Cooper, J. P. Eisenstein *et al.*, Phys. Rev. Lett. **82**, 394 (1999).
- Main P. C., A. K. Geim, H. A. Carmona *et al.*, Phys. Rev. B **50**, 4450 (1994).
- Maranowski K. D., J. P. Ibbetson, K. L. Campman *et al.*, Appl. Phys. Lett. **66**, 3459 (1995).
- Martel R., T. Schmidt, H. R. Shea *et al.*, Appl. Phys. Lett. **73**, 2447 (1998).
- Martin T. and S. Feng, Phys. Rev. Lett. **64**, 1971 (1990).
- Martin Y., D. W. Abraham, and H. K. Wickramasinghe, Appl. Phys. Lett. **52**, 1103 (1988).
- McCormick K. L., M. T. Woodside, M. Huang *et al.*, Physica B **249-251**, 79 (1998a).
- McCormick K. L., Ph. D. thesis, University of California, Berkeley (1998b).
- McCormick K. L., M. T. Woodside, M. Huang *et al.*, Phys. Rev. B **59**, 4654 (1999).
- McEuen P. L., A. Sfez, C. A. Richter *et al.*, Phys. Rev. Lett. **64**, 2062 (1990).

- McEuen P. L., M. Bockrath, D. H. Cobden *et al.*, Phys. Rev. Lett. **83**, 5098 (1999).
- McEuen P. L., Physics World **13** (June), 31 (2000).
- G. Müller, D. Weiss, A. V. Khaetskii *et al.*, Phys. Rev. B **45**, 3932 (1992).
- Nonnenmacher M., M. P. O'Boyle, and H. K. Wickramasinghe, Appl. Phys. Lett. **58**, 2921 (1991).
- Odom T. W., J. Huang, P. Kim, and C.M. Lieber, Nature **391**, 62 (1998).
- Ohtsuki T. and Y. Ono, J. Phys. Soc. Japan **58**, 3863 (1989).
- Palacios J. J. and C. Tejedor, Phys. Rev. B **44**, 8157 (1991).
- Park J. and P. L. McEuen, Appl. Phys. Lett. **79**, 1363 (2001).
- Postma H. W. C., T. Teepen, Z. Yao *et al.*, Science **293**, 5527 (2001).
- Prange R. E. and S. M. Girvin, *The Quantum Hall Effect*. New York: Springer-Verlag (1990).
- Saito R., M. Fujita, G. Dresselhaus, and M.S. Dresselhaus, Appl. Phys. Lett. **60**, 2204 (1992).
- Saito R., G. Dresselhaus, and M. S. Dresselhaus, *Physical Properties of Carbon Nanotubes*. New York: Plenum Press (1998).
- Sarid D., *Scanning Force Microscopy*. Oxford: Oxford University Press (1994).
- Schönenberger C. and S. F. Alvarado, Phys. Rev. Lett. **65**, 3262 (1990).
- Seeger K., *Semiconductor Physics: An Introduction*. Berlin: Springer-Verlag (1991).
- Shashkin A. A., A. J. Kent, J. R. Owers-Bradley *et al.*, Phys. Rev. Lett. **79**, 5114 (1997).
- Soh H. T., C. F. Quate, A. F. Morpurgo *et al.*, Appl. Phys. Lett. **75**, 627 (1999).
- Sohn L., L. P. Kouwenhoven, and G. Schön, eds., *Mesoscopic Electron Transport*. Dordrecht: Kluwer Academic Publishers (1997).

- Sondhi S. L., S. M. Girvin, J. P. Carini, and D. Shahar, *Rev. Mod. Phys.* **69**, 315 (1997).
- Staring A. A. M., H. van Houten, and C. W. J. Beenakker, *Phys. Rev. B* **45**, 9222 (1992).
- Stern J. E., B. D. Terris, H. J. Mamin, and D. Rugar, *Appl. Phys. Lett.* **53**, 2717 (1988).
- Stipe B. C., H. J. Mamin, T. D. Stowe *et al.*, *Phys. Rev. Lett.* **86**, 2874 (2001).
- Stowe T. D., T. W. Kenny, D. J. Thomson, and D. Rugar, *Appl. Phys. Lett.* **75**, 2785 (1999).
- Takaoka S., K. Oto, H. Kurimoto *et al.*, *Phys. Rev. Lett.* **72**, 3080 (1994).
- Tans S. J., M. H. Devoret, H. Dai *et al.*, *Nature* **386**, 474 (1997).
- Tans S. J. and C. Dekker, *Nature* **404**, 834 (2000).
- Tessmer S. H., P. I. Glicofridis, R. C. Ashoori *et al.*, *Nature* **392**, 51 (1998)
- Thess A., R. Lee, P. Nikolaev *et al.*, *Science* **273**, 483 (1996).
- Tomblor T. W., C. Zhou, L. Alexeyev *et al.*, *Nature* **405**, 769 (2000a).
- Tomblor T. W., C. Zhou, J. Kong, and H. Dai, *Appl. Phys. Lett.* **76**, 2412 (2000b).
- Topinka M. A., B. J. LeRoy, S. E. J. Shaw *et al.*, *Science* **289**, 2323 (2000).
- Topinka M. A., B. J. LeRoy, R. Westervelt *et al.*, *Nature* **410**, 183 (2001).
- Tortorese M., R. C. Barrett, and C. F. Quate, *Appl. Phys. Lett.* **62**, 834 (1993).
- van Wees B. J., E. M. M. Willems, C. W. J. Beenakker *et al.*, *Phys. Rev. Lett.* **60** 1848 (1988).
- van Wees B. J., E. M. M. Willems, C. P. J. M. Harmans *et al.*, *Phys. Rev. Lett.* **62**, 1181 (1989a).
- van Wees B. J., E. M. M. Willems, L. P. Kouwenhoven *et al.*, *Phys. Rev. B* **39**, 8066 (1989b).
- Wei Y.Y., J. Weis, K. von Klitzing *et al.*, *Phys. Rev. Lett.* **81**, 1674 (1998).

- Weitz P., E. Alhswede, J. Weis *et al.*, *Physica E* **6**, 247 (2000).
- Wiesendanger R., *Scanning Probe Microscopy and Spectroscopy*. Cambridge: Cambridge University Press (1994).
- Wharam D. A., T. J. Thornton, R. Newbury *et al.*, *J. Phys. C* **21**, L209 (1988).
- White C. T. and T. N. Todorov, *Nature* **393**, 240 (1998).
- Wildöer J. W. G., L. C. Venema, A. G. Rinzler *et al.*, *Nature* **391**, 59 (1998).
- Williams R. E., *Gallium Arsenide Processing Techniques*. Dedham, MA: Artech House (1984).
- Woodside M. T., C. Vale, K. L. McCormick *et al.*, *Physica E* **6**, 238 (2000).
- Woodside M. T., C. Vale, P. L. McEuen *et al.*, *Phys. Rev. B* **64**, 1310 (2001).
- Yacoby A., H. F. Hess, T. A. Fulton *et al.*, *Solid State Comm.* **111**, 1 (1999)
- Yahel E., D. Orgad, A. Palevski *et al.*, *Phys. Rev. Lett.* **76**, 2149 (1996).
- Yoo M. J., T. A. Fulton, H. F. Hess *et al.*, *Science* **276**, 579 (1997).
- Zhitenev N. B., R. J. Haug, K. von Klitzing *et al.*, *Phys. Rev. B* **49**, 7809 (1994).
- Zhitenev N. B., T. A. Fulton, A. Yacoby *et al.*, *Nature* **404**, 473 (2000).